Biblioteca Digital
F C E N - U B A

BIBLIOTECA CENTRAL LUIS F LELOIR
BIBLIOTECA CENTRAL LELOIR
FACULTAD DE CIENCIAS EXACTAS Y NATURALES UBA

Tesis Doctoral

Conmutación resistiva en óxidos de metales de transición y sistemas fuertemente correlacionados

Tesler, Federico Ariel

2018-03-27

Este documento forma parte de la colección de tesis doctorales y de maestría de la Biblioteca Central Dr. Luis Federico Leloir, disponible en digital.bl.fcen.uba.ar. Su utilización debe ser acompañada por la cita bibliográfica con reconocimiento de la fuente.

This document is part of the doctoral theses collection of the Central Library Dr. Luis Federico Leloir, available in digital.bl.fcen.uba.ar. It should be used accompanied by the corresponding citation acknowledging the source.

Cita tipo APA:
Tesler, Federico Ariel. (2018-03-27). Conmutación resistiva en óxidos de metales de transición y sistemas fuertemente correlacionados. Facultad de Ciencias Exactas y Naturales. Universidad de Buenos Aires.

Cita tipo Chicago:
Tesler, Federico Ariel. "Conmutación resistiva en óxidos de metales de transición y sistemas fuertemente correlacionados". Facultad de Ciencias Exactas y Naturales. Universidad de Buenos Aires. 2018-03-27.

EXACTAS UBA
Facultad de Ciencias Exactas y Naturales

UBA
Universidad de Buenos Aires

Dirección: Biblioteca Central Dr. Luis F. Leloir, Facultad de Ciencias Exactas y Naturales, Universidad de Buenos Aires. Intendente Güiraldes 2160 - C1428EGA - Tel. (++54 +11) 4789-9293

Contacto: digital@bl.fcen.uba.ar

UNIVERSIDAD DE BUENOS AIRES

Facultad de Ciencias Exactas y Naturales

Departamento de Física

Conmutación Resistiva en óxidos de metales de transición y sistemas fuertemente correlacionados

Tesis presentada para optar al título de
Doctor de la Universidad de Buenos Aires en el área Ciencias Físicas

por **Federico Ariel Tesler**

Director de Tesis: Dr. Marcelo Rozenberg
Director Asistente de Tesis: Dr. Alberto Camjayi
Consejero de Estudios: Dr. Carlos Acha

Lugar de Trabajo: Departamento de Fsica, FCEN, UBA

Fecha de defensa: 27 de marzo de 2018

Resumen

Luego de décadas de desarrollo sostenido, existe consenso en que las posibilidades de miniaturización en la industria electrónica de semiconductores está alcanzando su tope. Por lo tanto, en los últimos años ha comenzado una verdadera carrera de I+D en la búsqueda de nuevos materiales y mecanismos para seleccionar la base tecnológica de una nueva generación de dispositivos electrónicos. Entre las nuevas tecnologías estudiadas se encuentran los dipositivos basados en el fenómeno de Conmutación Resistiva (CR). Este fenómeno consiste en el cambio abrupto de la resistencia eléctrica de un material generado mediante la aplicación de un pulso eléctrico de corta duración (nano segundos a milisegundos). Este cambio de resistencia puede ser volátil (transitorio) o no-volátil (permanente o semi-permanente) y es en todos los casos reversible.

En esta tesis de doctorado se estudia el fenómeno de Conmutación Resistiva y sus potenciales aplicaciones. En el primer Capítulo se presenta una introducción al tema en donde se describen los distintos mecanismos que originan este fenómeno y sus principales aplicaciones. En los siguientes capítulos se presenta el trabajo realizado durante la tesis. Primero se presenta el trabajo realizado sobre dispositivos con CR no-volátil (principalmente en manganitas de la familia LCMO y óxidos binarios), en donde la conmutación es generada mediante la migración de especies iónicas entre distintas regiones del material. El eje central de esta parte del trabajo gira en torno a la formación de ondas de choque durante el proceso de migración, originadas a causa de la fuerte no-linealidad de la dinámica del sistema. Esta parte del trabajo involucra desarrollo analítico, computacional y experimental. En los siguientes capítulos se presenta el trabajo realizado sobre dispositivos basados en transiciones de fase en Sistemas Fuertemente Correlacionados, vinculados típicamente con CR de tipo volátil. El Capítulo 4 está dedicado a los materiales de la familia de calcogenoides AM_4Q_8 (A = Ga, Ge; M = V, Nb, Ta, Mo; Q = S, Se, Te) y el Capítulo 5 está dedicado al sistema VO_2. En cada caso se presenta el análisis teórico y computacional desarrollado durante la tesis para cada tipo de material. Finalmente se presenta el estudio realizado sobre las aplicaciones de estos materiales en redes neuronales artificiales.

Palabras clave: Conmutación Resistiva, memristores, Sistemas Fuertemente Correlacionados, Computación Neuromórfica

Resistive Switching in transition metal oxides and strongly correlated systems

Abstract

After decades of permanent development there is now consensus in that the miniaturization capabilities in the electronic industry is close to its limit. Thus, the development of new materials and mechanisms for the next generation of electronic devices has become a crucial topic. Among the new technologies under study we can find the devices based on the Resistive Switching (RS) phenomenon. The RS phenomenon consist in an abrupt change of the electrical resistance of a material under the application of short electrical pulses (from nano to miliseconds). This change of resistance can be volatile (transitory) or non-volatile (permanent or semi-permanent) and is in every case reversible. In this PhD thesis we study the RS phenomenon and its potential applications. In the first chapter we present an introduction to the subject where we describe the different mechanisms behind the RS and their main applications. The next chapters describe the work performed during the PhD. First we focus on devices with non-volatile RS (mainly manganites of the LCMO family and binary oxides), where the RS is generated by the migration of ionic species between different regions of the material. The main focus of this study is centered on the formation of shock-waves during the migration process, which are originated due to strong non-linearities in the system. This part of the thesis involves analytical, computational and an experimental work. Next we introduce the study performed on RS devices based in metal-insulator phase transitions in strongly correlated systems, which is mainly related with volatile RS. This work comprises the study of two different materials: one part is focused in chalcogenides of the AM_4Q_8 family (A = Ga, Ge; M = V, Nb, Ta, Mo; Q = S, Se, Te) and another part is focused on the VO_2 system. In each case we present the theoretical and computational work performed during the thesis for each type of material. Finally, we present a study on the application of these systems in artificial neural networks.

Keywords: Resistive Switching, memristors, Correlated Systems, Neuromorphic Computing

Agradecimientos

Agradezco a mi director Marcelo Rozenberg por todo el apoyo y la guía durante estos años de doctorado. A Alberto Camjayi y Pablo Levy, que colaboraron en la dirección de mi tesis. A los integrantes del grupo MeMOSat y del Laboratorio de Propiedades Eléctricas y Magnéticas de la Comisión Nacional de Energía Atómica (Pablo, Mechi, Cynthia, Mariano, Fernando, Diego, Nestor), donde desarrollé parte de mi trabajo. A Shao Tang y Vladimir Dobrosavljević de la Florida State University con quienes tuve el gusto de colaborar. A la Universidad de Buenos Aires. A mis compañeros de oficina, con los que compartimos incontables almuerzos y charlas. A mis hermanos y sobrinos. A mis padres por el apoyo constante durante mis años de estudio. A amigos, profesores, colegas y a todos los que han contribuido con mi formación durante estos años.

Contents

1 Introduction **1**

1.1 RS in transition metal oxides 2
1.2 RS in strongly correlated systems 4
1.3 Bio-inspired computing 8

2 Shock waves in transition metal oxides memristors **12**

2.1 Generalized Burgers' equation. 12
2.2 Model system 16
2.3 Shock wave formation: the "propagation phase" 17
2.4 Resistance switching: the "leakage phase" 19
2.5 Resistivity scaling 20
2.6 Dynamics of shock waves 22
2.7 VEOV model 22
2.8 Simulations details 23
2.9 Fitting for the VEOV model 25
2.10 Experimental details 26
2.11 Scaling 28
2.12 Quantitative comparison: experiments & simulations 30

3 Shock waves in binary oxides memristors **34**

3.1 Generalized Burgers' equation and SW dynamics in binary oxides 34
3.2 Model system and results 35

4 Volatile RS in strongly correlated systems. Towards the implementation of artificial neurons **41**

4.1 Introduction 41
4.2 The model 44
4.3 Filament formation and growth 49
4.4 Filament reabsorption: retentivity in the recovery phase 57
4.5 Resistance relaxation with an applied voltage bias 62
4.6 Complete pulse-voltage protocol 63
4.7 Dynamical analysis and filament formation 68

4.8 Retentivity for clusters with $d > w_B$ 69
4.9 Longer range interactions 71

5 VO_2 thermal spiking neuron **73**
5.1 Introduction 73
5.2 The model 73
5.3 Oscillations and filament formation 76
5.4 Dynamical analysis and the FitzHugh-Nagumo model 78
5.5 A LIF (Leaky-Integrate-and-Fire) implementation 84

6 Conclusions **91**

Appendices **94**

A Method of characteristics **95**

B Filaments size distribution in Experiments **97**

Bibliography **99**

Chapter 1

Introduction

After decades of permanent development, there is now a general consensus in that the miniaturization capabilities in the semiconducting industry will reach a limit within the next decade. The dimensions of the electrical components are now in the order of the tens of nanometers which is believed close to the limit for silicon based technology. Thus, there is urgent need to identify novel materials and physical mechanisms for future electronic device applications. Among the new developments under study, the phenomenon of Resistive Switching (RS) and its associated device the "memristor" has been intensively investigated during the recent years. This phenomenon consists in an abrupt change in the electrical resistance of a material under the application of an external strong electric stimulus. What makes this effect of interest is that the change of resistance can be non-volatile, i.e. permanent or semi-permanent, and reversible. This kind of technology has received a lot of attention due to its attractive features such as working speed in the nanosecond scale, low power consumption and high miniaturization potential, which makes it very attractive for future industrial applications. This phenomenon has been observed in a large number of different systems: it has been reported in materials such as simple binary oxides as CuO, NiO, MnO, Fe_2O_3 and in ternary perovskites as $SrTiO_3$, $SrZnO_3$. Even further, it has also been observed in "strongly-correlated-materials" such as high Tc superconductors cuprates (LSCO, YBCO) and also in manganite systems based in $LaMnO_3$ which have been widely studied the past decades due to its colossal magnetoresistance.

In addition, the RS-devices are currently being studied for the development of artificial neural networks and bioinspired computing: systems that process information based in the operation of biological neurons and synapses. The main objective of this thesis is to study the Resistive Switching phenomenon and its applications to Neural Networks. The RS is studied in two different types of systems: Transition Metal Oxides (TMO) and Strongly Correlated Materials. In Chapter 2 we present a study of ionic migration during RS in complex oxides (manganites) and we show that the switching process can be related with the

formation of shockwaves due to strong non-linear effects. This chapter involves experimental, theoretical and computational work. In Chapter 3 we extend the shockwave analysis for binary oxides, and we show that this dynamics can describe a wider range of materials. In the 4th and 5th chapter we focus in Strongly Correlated Materials and its application to Neurmorphic systems. In Chapter 4 we study the relaxation process after RS in chalcogenides of the family AM_4Q_8, which is associated with the recovery ("refractory") period of a biological neuron. In Chapter 5 we focus on RS in vanadium dioxide (VO_2) and we establish a relation between this system and an oscillatory neuron model known as "FitzHugh-Nagumo" model. In the rest of this introduction we provide a presentation of the different systems study during this thesis and on neuromorphic systems.

1.1 RS in transition metal oxides

Resistive Switching based in Transition Metal Oxides (TMO's) has been intensively investigated during the last decade. Standard RS devices (or "memristors") are capacitor like structures composed of insulating or semiconducting oxides sandwiched between two metal electrodes. The oxides under study range from binary oxides such as CuO, NiO, MnO, Fe_2O_3, ternary perovskites as $SrTiO_3$, $SrZnO_3$ to manganites as $LaMnO_3$ [1, 2]. Through extensive experimental work during the past years, a consensus has emerged about the mechanisms behind RS in these systems. Depending on the switching behaviour, RS is generally classified in two types: unipolar and bipolar RS. In the unipolar case the RS depends on the amplitude of the applied voltage but is independent of the polarity. This kind of RS is usually associated with the formation and rupture of metallic filaments within an insulating medium. Here thermal redox and/or anodization are typically considered as the mechanisms behind the formation and rupture of the filaments [1, 3]. In contrast, in bipolar-RS the switching between high-to-low and low-to-high resistance states demands the inversion of the applied polarity. In this case the mechanism involves the migration of ionic species, including oxygen vacancies (V_O), affecting the local transport properties of the system [4, 5]. In Fig.1.1.a-b) we show typical characteristic I-V curves for unipolar and bipolar RS.

A second classification of RS devices is based on the conducting path involved in the switching: they are usually classified as either "filamentary" or "interfacial". In insulating mediums (such as TiO_2) the RS typically involves the formation and rupture of filamentary conducting paths within the insulating matrix [1, 3]. This is known as filamentary RS. In these systems the RS process is usually initiated by a breakdown (forming) operation, which results in the formation of a conductive nanofilament responsible for the low resistance [3]. Reported

filament sizes are in the order of the few nm [4, 6]. This is in many ways similar to typical dielectric breakdown, but it has the advantage that the rupture can be reversed and repeated, while it is usually irreversible in typical dielectrics. Direct measurements of conducting filaments have been reported, typically by electron microscopy, and identification of local species and phases has been possible. In TiO_2 devices a Ti_4O_7 Magneli phase with metallic conductivity has been identified at the filament location [4, 7]. This indicates that suboxides, or oxygen-poor phases/alloys, can be responsible for the locally high conductivity. Devices associated with filamentary RS have shown both unipolar and bipolar type of RS [1].

In contrast to filamentary RS, in semiconducting mediums such as $LaCaMnO_3$, the resistive switching usually takes place over the entire interface between the metal electrode and the oxide, with no evidence of filament formation [8]. In this case the RS is typically related with bipolar resistive switching due to oxygen migration. A diagram of the filamentary and interfacial RS is shown in Fig.1.1.c-d). A key feature in interfacial RS is the role of highly resistive interfaces, such as Schottky barriers (SB) [1, 9, 10]. Standard interfacial RS devices involve a metal-semiconductor junction and are likely to form a SB. If the barrier is high enough it leads to the appearance of a depletion layer in the interfacial region and a high contact resistance. The formation and size of the barrier depends on the band structure of the two compounds involved in the junction [11]. This makes interfacial RS strongly dependent on the particular metal used for the electrode. As an example, the p-type semiconductor $Pr_{0.7}Ca_0.3MnO_3$ exhibits RS with rectification behaviour for Ti electrodes, while ohmic behaviour with no RS is observed for Au or $SrRuO_3$ electrodes [1]. In this case as the work function of the metal decreases ($\sim$ 4.3 eV for Ti, $\sim$ 5.1 for Au and $\sim$ 5.3 eV for SrRuO) the contact resistance increases and rectification behaviour emerges as predicted by classical Schottky-Mott theory [11]. In these systems the presence of oxygen-vacancies in the interfacial region is believed to affect the width of the depletion layer in addition to the evident disorder effects that they may also produce. In p-type oxides semiconductors the presence of oxygen vacancies is considered equivalent to a reduction of acceptors, which may cause the depletion layer to become wider. Thus, it is thought that the migration of oxygen vacancies from or toward the interfacial region can modulate the width of the depletion layer, inducing the RS by a change in the contact resistance [1, 9]. Another effect that the oxygen vacancies may bring is to disrupt the p-d hybridized conductions bands due to the missing oxygens. In such a case, the resistivity of the regions with oxygen vacancies should be expected to increase. A detail transport theory of this phenomenon is very challenging. Nevertheless, as we shall see we may incorporate a simplified version of it in our numerical modeling of the RS in these type of

materials.

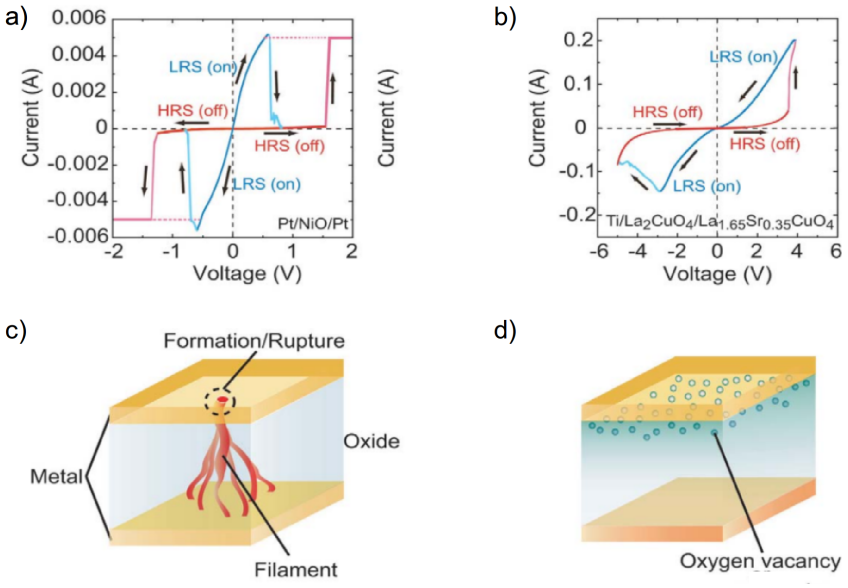

Figure 1.1: a-b) I-V curves for unipolar RS (a) in a Pt/NiO/Pt device and bipolar RS (b) in a $Ti/La_2CuO_4/La_{1.65}Sr_{0.35}CuO_4$ device. In unipolar RS the change between the High Resistance State (HRS) and the Low Resistance State (LRS) depends on the amplitude of the applied voltage. In bipolar RS the switching depends both on the amplitude and the direction (adapted from Ref.[1]). c-d) Diagrams of filamentary and interfacial RS.

In Chapter 2 we will present a study on bipolar RS in complex oxides, associated with ionic migration in highly resistive interfaces. There we analyze the migration dynamics of oxygen-vacancies, and we argue that the strong non-linearity of the process leads to the formation of shock waves that explain the sudden resistance change observed in experiments. We validate our theoretical analysis with simulations and experiments performed on a manganese based memristor device. Then, in Chapter 3 we extend this analysis for RS in binary oxides devices and we show that the formation of shock waves is also feasible in these systems, which suggest that this is a very general feature of bipolar RS in TMO's.

1.2 RS in strongly correlated systems

Most of the more important properties of materials discovered during the last few decades are related to the existence of electron-electron interactions which are large with respect to the kinetic energies and could not be captured by traditional band theory. These properties include phenomena such as superconductivity and the occurrence of metal-insulator transitions in certain materials (such as Mott-

insulators), which are a central part of the current thesis. Unlike conventional band insulators and semiconductors, Mott-insulators possess, according to conventional band theory, an odd number of electrons for which they are expected to be metals as their Fermi levels lie in the middle of a band. However, these materials turn out to be insulators. The discrepancy comes from the existence of a relatively large on-site Coulomb repulsion, which is not properly considered in traditional band theory. The theoretical description of this type of materials has been achieved with modern approaches such as the Dynamical Mean Field Theory (DMFT) that have been able to correctly describe the phase diagram of these systems [12, 13]. In Fig.1.2.a) we show a schematic phase diagram of a compound going through a Mott insulator-to-metal transition (extracted from Ref.[14]). In this figure a single band system at half filling (i.e. with one electron per site) is considered. If the Coulomb repulsion (Hubbard) energy U exceeds the bandwidth W, the half-filled band splits into two sub-bands, the lower (LHB) and upper (UHB) Hubbard bands . Thus, the U term leads to the appearance of a Mott-Hubbard gap E_G between the LHB and the UHB, approximately equal to $E_G \approx U - W$ [12]. In this phase diagram a first order (Mott) transition line separates a metallic phase at low U/W from a paramagnetic Mott insulator (PMI) phase at high U/W [12, 13, 15], as depicted in Fig.1.2.a). This Mott metal-insulator transition line terminates at a second order critical endpoint at high temperature[12, 13, 15]. This endpoint indicates the absence of crystallographic symmetry breaking across the Mott line, since it is possible to connect continuously the PMI and metallic phases through a high temperature path above the endpoint. While the Mott line and the high temperature part of the phase diagram are universal, the low temperature part is material-dependent. This phase diagram highlights two main insulator-to-metal transitions (IMT), represented by red arrows in Fig.1.2.a) [16]. One is the Bandwidth controlled IMT. This IMT corresponds to the crossing of the Mott transition line (see Fig.1.2.a)) induced by tuning the correlation strength U/W [16], which can be achieved by applying an external pressure [12]. The other IMT is the Temperature controlled IMT. This IMT, is driven by temperature and also consists on the crossing of the Mott line in a small region of U/W around ≈ 1.15, between the red dotted line in the figure. This IMT occurs between a low temperature metal and a high temperature insulator [17], in contrast with the more usual transitions from a low-T insulator to a high-T metal. A third IMT can be induced via chemical doping [16]. Finally, for materials exhibiting a low temperature insulating phase, a temperature induced transition from insulator to metal can also be achieved. This type of IMT is usually associated with materials exhibiting long range (e.g. magnetic or orbital) orders [14]. Among known Mott insulators exhibiting a phase diagram as in Fig.1.2.a) (sometimes called canonical Mott insulators) we can find the

oxide $(V_{1-x}Cr_x)_2O_3$, which exhibits a Mott IMT line ending around 450K and separating a Mott insulating phase from a metallic phase, and the V_2O_3 system. Recently a series of chalcogenides systems, the AM_4Q_8 compounds (A = Ga, Ge; M = V, Nb, Ta, Mo; Q = S, Se, Te), have emerged as a potential new example of canonical Mott insulator. These compounds own a narrow gap of $0.1-0.3$ eV, which can be tuned by chemical substitution [18]. At ambient pressure, all AM_4Q_8 compounds display two important characteristics of canonical Mott insulators: they are paramagnetic insulators above 55K [19–21] and do not exhibit any temperature-controlled IMT up to 800 K. Moreover, these compounds exhibit a bandwidth-controlled IMT under pressure [20, 22].

Beyond the case of Mott insulators, we can find other partially-filled insulators displaying temperature controlled IMT, which are also relevant for memory and neuromorphic applications. This include IMT in Ca_2RuO_4 (T_{IMT} = 357 K) [23], NbO_2 (T_{IMT}= 1070 K) [24] , $ANiO_3$ perovskites [25] and VO_2 (T_{IMT} = 340 K) [26]. In Fig.1.2.b) we show the temperature-pressure phase diagram for VO_2. This half-filled insulator contains an IMT line separating a low-T insulating phase from a high-T metallic phase of different crystallographic symmetry (associated with last type of IMT mentioned before) [27, 28]. This system exhibits a transition from a metal with a rutile structure towards an insulator with monoclinic structure for low temperatures.

Compounds undergoing temperature induced IMT are also prone of exhibiting RS (i.e. electrically induced IMT). Indeed, the application of an electric field at $T < T_{IMT}$ can lead to Joule self-heating and therefore to RS if the sample temperature exceeds T_{IMT}. Such a thermal mechanism is at play in correlated metals in the close vicinity of the Mott line, where a volatile resistive switching under electric field between a low T metallic phase and a high T paramagnetic Mott insulator is observed [29–31]. Also, this thermal mechanism may explain the switchings observed in compounds such as VO_2 [32, 33]. It is still not totally clear if the volatile resistive switching in these systems is thermal or electric, or a combination of the two. The volatile transition may be maintained by the continuous application of the electric pulse. As we shall also see, they are characterized by the existence of a threshold value for the electric stress that is required to produce the change. However, we should also mention that non-volatile resistive switching (i.e., the low resistance state remains even after the end of electric pulses) has also been observed in these correlated insulators [34].

As we mentioned before, besides the thermal switching, another mechanism for RS in these systems is the so called dielectric-breakdown. This mechanism is believed to be behind the volatile resistive switching reported in the quasi-one-dimensional Mott insulators Sr_2CuO_3 and $SrCuO_2$ [35] or in the insulating charge-ordered state of $La_{2-x}Sr_xNiO_4$ [36]. These compounds exhibit an IMT

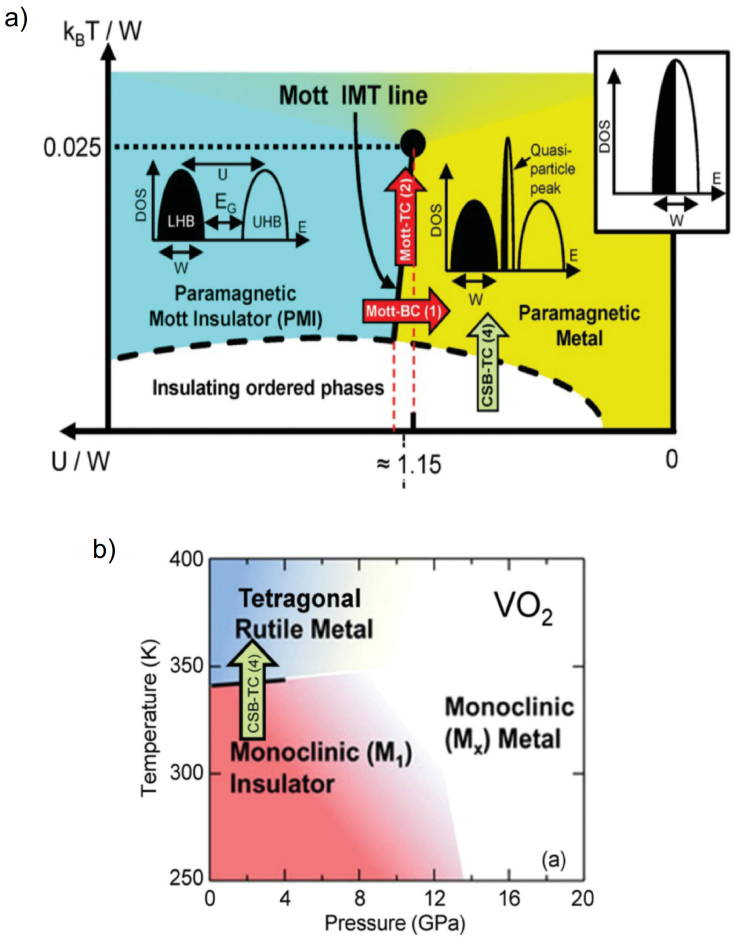

Figure 1.2: a) Schematic phase diagram of systems undergoing a Mott insulator to metal transition. Here W is the bandwidth, T the temperature, and U the Coulomb repulsion energy. Typical density of states (DOS) are shown. The inset (top right) shows the case U=0. b) Schematic temperature-pressure phase diagram of VO_2 (diagrams adapted from Ref.[14]).

for fields above a threshold of the order of $10^2 - 10^4$ V/cm. Similar phenomena were also reported for the family of chalcogenide Mott insulators AM_4Q_8 [37, 38]. Many theoretical works were recently devoted to dielectric breakdown and were mainly focused on the Zener breakdown for Mott insulators [39, 40]. However these studies have predicted the Zener breakdown to occur for strength of the electric field of the order of $10^6 - 10^7$ V/cm [39]. This is at least two orders of magnitude larger than the values observed experimentally [35, 36, 38]. Thus, volatile resistive switching in Mott insulators cannot be explained by a Zener breakdown alone. Alternatively, recent studies on the AM_4Q_8 Mott insulators indicate that the dielectric breakdown originates from an electric field induced electronic avalanche phenomenon [41, 42].

The case of avalanche breakdown in AM_4Q_8 compounds will be further developed in Chapter 4. In that chapter a recently presented model is reviewed [42]

and an extension will be proposed. In a first part of our study a dynamical analysis of the model is performed and the origin of the threshold behaviour is studied. Then we introduce an extension of the model that incorporates local interactions which can explain different switching regimes observed in experiments.

Finally, in Chapter 5 we will introduce a simple phenomenological model for the thermally induced RS in VO_2 described before, and its application for artificial spiking neurons will be analyzed.

1.3 Bio-inspired computing

Traditional computational structures are based in what is known as the von Neumann architecture. In this computational architecture the memory unit (data-storage) is separated from the processing unit ("CPU") and they interchange data via a communication system (a "bus") (see Fig.1.3). Since its development in the 40's, the von Neumann architecture has become the standard structure for modern computers. The astonishing development observed in the past decades in both their memory and processing capacity has been based in the exponential advances of the silicon-based technology. However, current computational systems are facing some main challenges that demand for novel approaches. In the first place, limitations related with the silicon-based technology are emerging, as the feature size of CMOS components is reaching the few nm. Second, there is a fundamental limitation related with the communication path between the memory and the processor: the rate of data transfer between units establishes a limit for operational speed. This is a classical problem of the von Neumann architecture and it is known as the "von Neumann Bottleneck" [43]. Some standard modifications and improvements to this architecture are currently used to mitigate this last problem. One is the inclusion of a "cache", which is a smaller and faster memory that stores recently or frequently used data to feed the processor. Another is the use of "parallel computing", i.e. the use of multiple processors (from a few to thousands) working simultaneously [44].

A third important limitation of traditional computer devices is that they have shown a poor performance in some basic tasks such as speech and image recognition, in which biological systems excel.

Thus, the idea of incorporating computing mechanisms inspired in biological systems has become of great interest. This idea has been present for several decades and has more recently received a lot of attention due to the massive development of "Machine Learning" (ML) techniques. Among one of the most widely used ML techniques is the one known as "Deep Learning", which makes use of tools based in multilayer Artificial Neural Networks (ANNs), which are inspired in biological nervous systems [45–48].

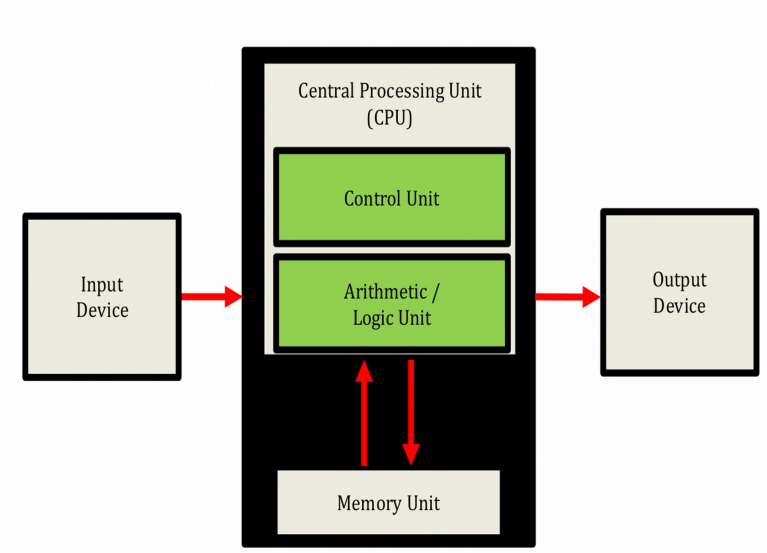

Figure 1.3: Conventional von Neumann computer architecture. The so called "von Neumann bottleneck" consists in the communication path between the memory and the processor unit. This is a traditional limitation for computing performance in this architecture.

A biological nervous system consists in billions of cells called neurons which are densely connected to each other. These connections are known as "synapses" and allow neurons to transmit electrical signals among them. The state of a neuron is usually described in terms of the voltage drop across its cellular membrane. In short, neurons are permanently integrating the incoming electrical signals and when the membrane potential reaches a certain threshold they emit a short electric pulse (spike). These spikes are in turn transmitted through the synapses to other neurons which integrate the signal and again emit a spike. This constitutes the basic dynamics of neuronal activity. Probably, the best known neuronal model is the one of Hodgkin and Huxley [49]. This model describes the membrane potential by means of a circuital diagram made by a set of parallel branches (see Fig.1.4.a)). One branch represents the membrane capacitance, a second branch represents a leakage current and the rest of the branches represent different types of voltage activated channels, these last ones modeled as non-linear voltage-dependent conductances.

Together with the neuron, the other crucial component of the biological nervous system is the synapse. Each synapse is characterized by a "weight" which establishes the strength of the connection between two neurons. These weights are essentially stable, but can change over time depending on previous neuronal activity. This last feature is called "synaptic plasticity" and is believed to be the main mechanism behind biological learning and memory.

Similarly, an Artificial Neural Network consists in a collection of connected units where each unit is analogous to a biological neuron and each connection

to a biological synapse and where neurons can transmit signals to each other. Typically, neurons receive an input in form of real numbers, apply a non-linear function and send the result to other neurons. In a typical implementation an ANN is initially trained ("learn") to perform a task by using a series of examples. The training process implies the reconfiguration of synaptic weights following a predefined algorithm (e.g. "back-propagation")[45]. The learned task can consist in, for example, the classification of incoming data.

Indeed, the use of ANN's has shown to be very effective to perform tasks such as image and speech recognition and are currently a standard tool in big-data analysis [45, 46]. However, most of this progress has been reached by running the new algorithms with conventional codes on conventional (i.e. von Neumann) computers. While the performance of these algorithms is remarkable at many tasks, unfortunately, their power is still limited by the computational power of current machines.Therefore, an exciting perspective is to implement the neural networks directly on hardware, by realizing novel electronic devices that may directly implement the neural network functionality. In this context, RS devices have emerged as relevant candidates to develop the building blocks of direct hardware ANN: i.e. artificial synapses and neurons. The implementation of RS devices as "analogue synapses" has been actively investigated during the past few years [50, 51]. Its programmable resistance plays the role of the "plastic" synaptic weight that is adjusted during the learning process. Unfortunately, the progress in the research and implementation of "analogue neurons" has not been comparable. Hence, its development becomes very important. In the context of resistive change system we may mention two important contributions towards devices with a neuron inspired functionality: One is the "neuristor", which realizes a functionality similar to the Hodgkin-Huxley model for electric pulse propagation in biological axons [52]. The other one is the "artificial neuron", which is based in AM_4Q_8 compounds (described in the previous sections) and which implements the functionality of a leaky-integrate-and-fire (LIF) biological spiking neuron [53]. This last implementation is widely used in computational neuroscience and is based in a very simple model of a neuron in terms of a capacitor with a leakage current (see Fig.1.4.b)). Remarkably, both implementations are based on Mott insulators.

In Chapter 4 we will describe the LIF implementation of Ref.[53] and we will present a study on the "refractory period" in this system: i.e. the recovery period of the neuron after a spike has been fired. Finally, in Chapter 5 we present a new implementation of an artificial neuron based on VO_2 devices. This implementation makes use of the resistance oscillations observed in VO_2 and a direct analogy is made with the well known FitzHugh-Nagumo model of oscillatory neurons.

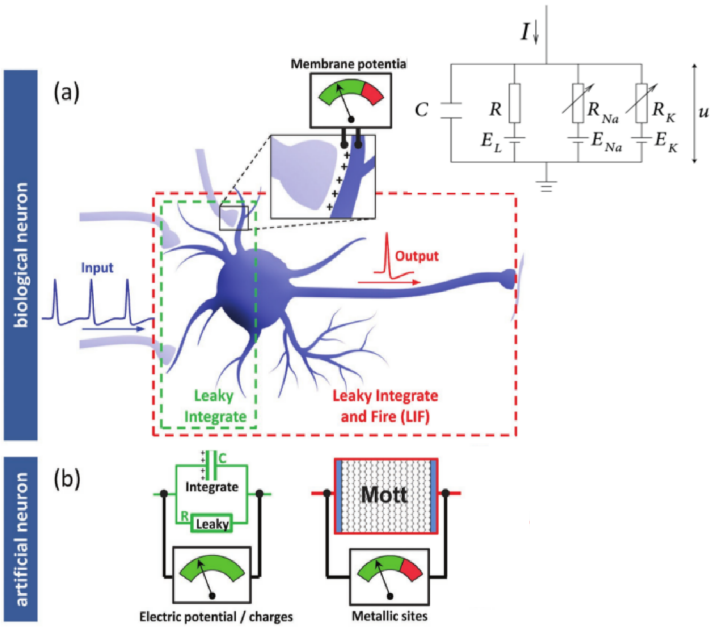

Figure 1.4: a) Schematic representation of a biological neuron receiving input spikes from other neurons and triggering an ouput action potential when the membrane potential reaches the threshold value (adapted from Ref.[53]. Top right: circuit diagram of the Hodgkin-Huxley model. The neuron is described in terms of a capacitance C, a leakage current (through resistance R), a set of voltage activated channels (R_{Na}, R_K) and the trans-membrane potential u. The $E_i's$ are constant voltages known as reverse-potentials. b) The LIF artificial neurons reproduce the evolution of the membrane potential thanks to a Resistance Capacitance (RC) circuit accumulating electrical charges. The Mott artificial neuron reproduces the LIF behavior thanks to the accumulation of correlated metallic sites.

Chapter 2

Shock waves in transition metal oxides memristors

In the present chapter we shall address one of the key aspects of the RS phenomenon in transition metal oxides (TMOs), namely, the issue of the commutation speed of the resistance change. Our first striking result is a connection between the RS phenomenon and *shock wave* formation, a classic topic of non-linear dynamics [54]. In fact, we shall argue that the profile of oxygen vacancies that migrate during the resistive change forms a shock wave that propagates through the highly resistive Schottky barrier and leaks onto the bulk of the device, which we schematically illustrate in Fig.2.1. We further validate the scenario by means of numerical simulations on a successful model of RS and by novel experiments done on a manganese based memristor device. Both model calculations and experiments reveal a striking scaling behaviour as predicted by the shock wave scenario.

2.1 Generalized Burgers' equation.

When ions migrate through a *conducting* medium under the influence of strong applied voltage, they are likely to undergo a nonlinear diffusion process, as we explain in the following. The total ionic current $\mathbf{j}(t,\mathbf{x}) = \mathbf{j}_{diffusion} + \mathbf{j}_{drift}$ can be expressed as the sum of a diffusion current $\mathbf{j}_{diffusion} = -D\nabla u$ and a drift current $\mathbf{j}_{drift}$, which is induced by the local electric field $\mathbf{E}$ and the local concentration u. Together with the continuity equation $\partial_t u + \nabla \cdot \mathbf{j}(\mathbf{x},t) = 0$, this immediately gives us a generalized diffusion equation of the Nernst-Planck type. This would represent a familiar drift-diffusion equation, were the local electric field $\mathbf{E}$ to be held constant, i.e. independent of the local ion concentration u. In contrast, in (poorly) conducting media and under voltage pulses, the local electric field may strongly depend on the local ion concentration; this effect is the key source of

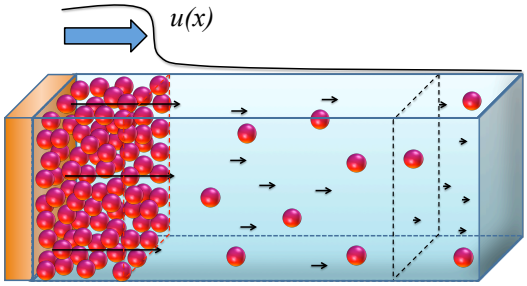

Figure 2.1: Schematic representation of the shock wave evolution. The orange region indicates the metallic electrode and the blue indicates the TMO dielectric. Small spheres denote the ionic defects (oxygen vacancies) whose density profile form a shock wave. It evolves through a highly resistive (Schottky) interface and eventually leaks over the more conductive bulk, producing the resistive change. Black arrows depict the strength of the local electric fields.

nonlinearity causing the formation of shock waves and very sudden resistance switching [9, 55].

Since electrons move much faster than the ions, we can view the ions as static when considering the electronic current $\mathbf{I}$, which obeys a steady-state condition $\nabla \cdot \mathbf{I} = 0$. The local electric field is then simply determined, through Ohm's law, by the local resistivity $\mathbf{E} = \rho(u)\mathbf{I}$, which may be a strong function of the local ion concentration u. In particular, in bad metals such as the transition metal oxides, the migrating ions (e.g. oxygen vacancies) act as scattering centers for the conduction electrons. In such situations, we expect $\rho(u)$ to be a *monotonically increasing* function of the local ion vacancy density $u(\mathbf{x}, t)$. Therefore, the redistribution of the local ion density results in the change of local resistivities and, consequently, of the local electric fields, which further promotes the non-linear effect in the drift.

Under the experimentally-relevant case where the transverse currents may be neglected, the problem simplifies to a one-dimensional non-linear diffusion equation,

$$\partial_t u + f\,(u)\,\partial_x u = D\partial_{xx} u, \tag{2.1}$$

where $f\,(u) \equiv \partial_u j_{drift}\,(u, I)$, and $I(t)$ is the magnitude of the electronic current. Equation (3.1) can be considered a generalization of the famous *Burgers'* equation, which corresponds to the special case $f\,(u) \propto u$. Its most significant feature is the presence of a density-dependent drift term, *which physically means that the "crest of the wave" experiences a stronger external force than the "trough"*. This generally leads to the formation of a sharply defined *shock-wave* front in the $u(x, t)$ profile, which assumes a universal form at long times, completely inde-

pendent of the - quickly "forgotten" - initial conditions. Although the process is driven by the drift term, the stability of the shock wave form is provided by the existence of the diffusion term which prevents the shock wave from self-breaking [54, 56] [1] . Remarkably, the formation of shock waves proves to be robust in a much more general family of models with the nonlinear drift term specified by the function $f(u)$, any *monotonically increasing* function of u. The qualitative behaviour can be established by using the well-known method of characteristics [54, 57], that we illustrate with an example in Fig. 2.2 (see Appendix A for a more detailed explanation).

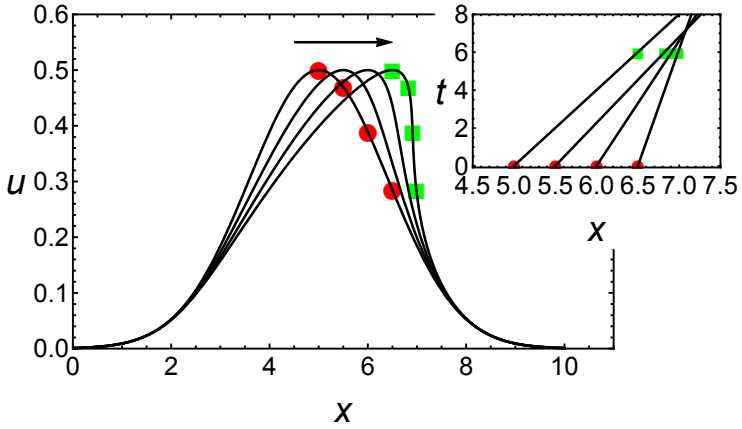

Figure 2.2: Time evolution of a generic density profile according to the generalized Burgers' equation (3.1). Curves correspond to profiles at $t = 0$, 2, 4 and 6. The (arbitrary) initial profile is taken Gaussian and we adopt $f(u) \propto u^2$. The color dots track constant-u points and show the formation of the universal steep shock wave profile. Inset: $x - t$ coordinates of the constant-u tracking points (characteristics). The velocity of each point only depends on its u value. The crossing of the characteristics signals the formation of the multivalued steep shock-wave front.

The drift current is generally given by the expression $j_{drift} = ug(E)$. The form of the function $g(E)$ is material-dependent, and here we envision two limiting situations. In homogeneous conductors, we should have simple "Ohmic" behavior as $g(E) \sim E$ while in granular materials, we expect exponential dependence due to activated transport, corresponding to: $g(E) \sim \sinh(E/E_0)$, where E_0 is a parameter describing the activation process.

[1] While the drift current contains the nonlinear term that leads to a steep wave front, according to Fick's law, the diffusion current flows in such a way as to reduce the steepness of the density profile. Therefore, the diffusion current stabilizes the propagation of the shock wave and it protects the solution from entering the self-breaking region (multi-valued solution). In the scenario of the standard Burgers' equation, where $f(u) \sim u$ in Eq(1), the equation can be explicitly solved via Cole-Hopf transformation (see references [54, 56]. In that case we can check the effects of the diffusion current against nonlinear drift exactly.

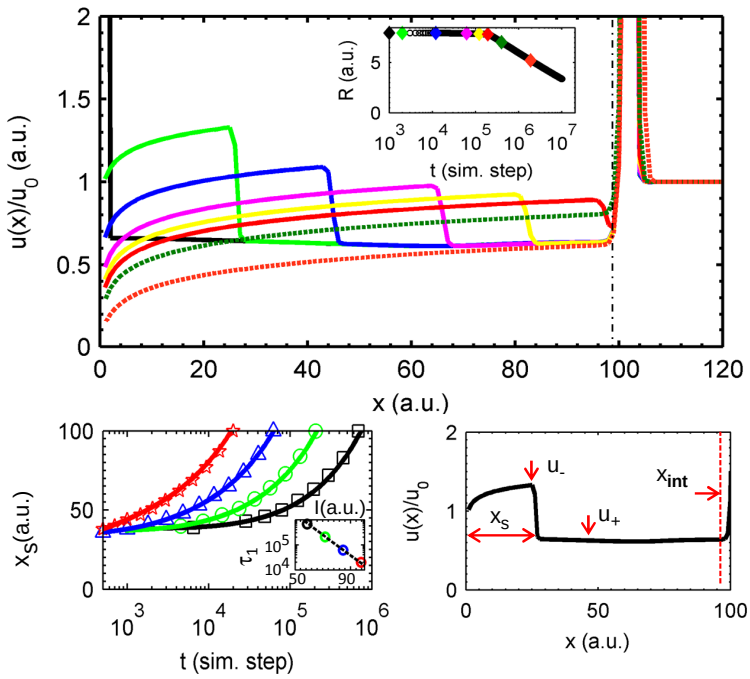

Figure 2.3: Top panel: Snap shots of the time evolution of the density profile $u(x,t)$ within the active interfacial region in a simulation of the VEOV model (see section 2.7 and 2.8 for details). The current used is $I[a.u]$=71.5, with A_{SB}=1000 and A_B=1. The time steps of the successive profiles can be read-off from the corresponding color dots in the inset. The initial state $u(x,0)$ (black line) exhibits a vacancy pile-up next to the electrode at x=1. The SB-B interface is denoted with a vertical dash-dot line at x_{int}=100. The large accumulation of vacancies on the right of x_{int} (bulk side) results from the initial "forming" cycles performed on an originally uniform profile of density u_0. The result of the forming cycles is an approximately fixed background on top of which the density profile further evolves (see details in [58]). Inset: Resistance of the device as a function of time. Color dots indicate the value of $R(t)$ at the corresponding snapshots of the main panel. Bottom-left panel: evolution of the shock wave front position $x_s(t)$ for different currents ($I[a.u]$=58.5, 71.5, 84.5 and 97.5). Dots are from numerical simulations and the solid lines are analytic fits from integration of Eq. (2.4). Inset: characteristic impact-time τ_1 as a function of applied currents from the numerical simulation (circles) and analytic fit (dotted-line) in semi-log scale. Bottom-right panel: Shock wave parameters.

Remarkably, these general ideas find an explicit realization in the context of RS in transition metal oxide memristors, such as manganites [10, 59]. In fact, their transport properties are very sensitively dependent on the oxygen stoichiometry, i.e. on the concentration of oxygen vacancies $[V_O]$. Thus, it is now widely accepted that the mechanism of the bipolar (i.e. polarity dependent) RS in those systems is due to the induced changes in the spatial distribution of $[V_O(\mathbf{x})] \equiv$

$u(\mathbf{x})$ by means of externally applied strong electric stress [9, 55]. In particular, the accumulation of vacancies within highly resistive regions between the oxide and the metallic electrode, such as Schottky barrier (SB) interfaces, greatly increases the (two-terminal) resistance across the device [58]. This accumulation can be achieved by applying strong voltage pulses across the device, leading to the high resistance state R_{HI}. Abrupt resistance switching from such high-resistance state to a significantly lower resistance state can be accomplished by reversing the voltage applied, which removes a significant fraction of vacancies from the SB region. The precise characterization of this resistance switching process is the main subject of this chapter.

We should mention that an important assumption is that the nonlinear drift term plays the dominant role as compared to the normal diffusion, i.e. we shall not be concerned with the resistive changes involving thermal effects [9, 55]. This restriction enables us to apply our analytical tools in a simple manner, allowing us to obtain a simplified mathematical description of the migration process, as we show in the following.

2.2 Model system

For concreteness, we adopt the *voltage-enhanced oxygen-vacancy migration model* [58] (VEOVM), which corresponds to granular materials with activated transport process and has been previously used for manganite devices [58]. Within the framework of this model, we shall perform numerical simulations to validate our shock-wave scenario. The VEOVM simply assumes that the local resistance of the cell at (discretized) position x along the conductive path of the device is simply given as a linear function of the local vacancy concentration, namely,

$$r(x) = A_\alpha u(x) \tag{2.2}$$

with $\alpha = SB, B$, where SB denotes the highly resistive (Schottky barrier) region and B the more conductive bulk [10]. The values of these constants are taken $A_{SB} \gg A_B = 1$, which allows us to neglect the bulk resistance [58]. The discretized conducting path assumes the metal-electrode at x=0, and $x = x_{int}$ denotes the point within the dielectric where the SB meets the bulk region. Under the action of the external stress (electric current I), the local fields at each cell position x are computed at every discrete time step t. The field-driven migration of vacancies is simulated computing the local ionic migration rates from cell x to $x+\Delta x$ as [58]

$$P(x, x+\Delta x) = u(x)[1-u(x+\Delta x)] \exp\left(\frac{-V_0 + qIr(x)}{k_B T}\right), \tag{2.3}$$

where, for simplicity, we take the ionic charge q=1 and k_BT=1. The parameter V_0 denotes the activation energy for ionic diffusion. The new profile $u(x,t)$ is updated from the migration rates, and from (2.2) we get the new total (two point) $R(t)$ as the discrete x-integral of the local cell's resistance $r(x,t)$. Here, for simplicity, we focus on a single active SB-bulk interface, while the more general situation with two barriers may be analyzed following a similar line of argument [58]. The applied external electric stress that we adopt is a constant current, in both, simulations and experiments (see below).

As described in Ref.[58], the initial vacancy concentration profile is assumed to be constant $[u(x)] = [u^0]$. The "forming" or initialization of the memory is done by first applying a few current loops of alternative polarity, $\pm I^0$, until the migration of vacancies evolves towards a *limit cycle*, with a well defined profile $u_0(x)$. After this, the system begins to repetitively switch between two values: R_{HI} and R_{LO}. In the first, most of the vacancies reside within the high-resistance region SB, and in the second vacancies accumulate in the more conductive bulk. The R_{HI} state with the vacancies piled up in the first cell, at x=1, defines the initial state for the shock wave propagation (see Fig.2.3).

2.3 Shock wave formation: the "propagation phase"

We apply an external field with polarity pointing from the SB to the bulk and observe the evolution of the vacancy profile as a function of the (simulation) time. As can be observed in Fig.2.3 there is a rapid evolution of the profile into a shock wave form with a sharply defined front. We also notice that the total resistance remains approximately constant during an initial phase, and suddenly starts to decrease after the front hits the internal SB-bulk interface at x_{int} (inset of top panel of Fig.2.3). We shall analyze these key features in the following.

First, we focus on the propagation of the shock wave front position $x_s(t)$, as shown in Fig.2.3 (bottom-left panel) for different values of the electronic current I. We observe that the characteristic time τ_1 for the shock wave to travel through the Schottky barrier and reach the SB-bulk point x_{int} decreases exponentially with the magnitude of I. To obtain analytical insight for this behavior, we recall that the velocity of the shock wave front dx_s/dt is very generally given by the Rankine–Hugoniot conditions [54, 60], which express it as the ratio of the spatial discontinuity of the (vacancy) drift current, and the spatial discontinuity of the density profile across the shock viz. $dx_s/dt = \Delta j/\Delta u\,|_{x_s}$. Within the VEOV model [58], we obtain the following *nonlinear rate equation* (see section 2.6 for details), which describes the dynamics of the shock wave front:

$$\frac{dx_s}{dt} = \frac{2Du_- \sinh\left(IA_{SB}u_-\right) - 2Du_+ \sinh\left(IA_{SB}u_+\right)}{\Delta u}, \tag{2.4}$$

where D is a prefactor related to the activation energy for vacancy migration (Arrhenius factor) (see Eq.3.1 and Ref.[58]), and $u_{-/+}$ are the density of vacancies at the two sides of the shock wave front (see Fig.2.3). The density u_- depends on the shock wave front position via: $u_- = Q/x_s + u_+$, where Q is the total number of vacancies carried by the shock wave, which remains a constant parameter through the propagation phase ($t < \tau_1$) and u_+ is a constant background density which can be written as $u_+ = Q_B/x_{int}$, Q_B standing for the total number of background vacancies.

Our description of the propagation phase is fully consistent with our numerical simulations. As shown in the inset of Fig.2.3 (top panel), the resistance remains essentially constant until the wave front reaches the SB-bulk interface after a (current dependent) time τ_1, and then begins to drop. Moreover, we also achieved a good fit to the shock front velocity by using Eq.2.4, as is shown in Fig.2.3 (see section 2.9 for details).

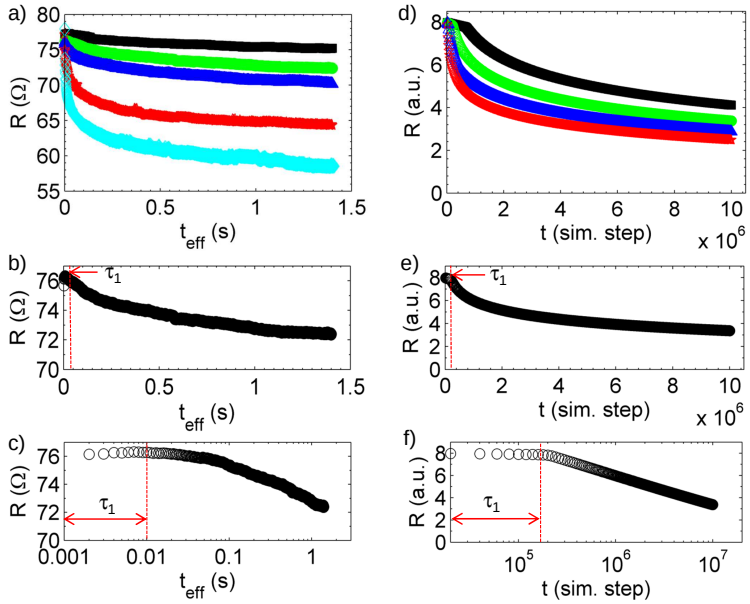

Figure 2.4: Time dependence of the resistive change $R(t)$ for various external current intensities. Top left: experimental data measured on an Ag/LPCMO/Ag memristor with $I = 37.5$ mA (black), 40 mA (green), 50 mA (blue), 80 mA (red) and 100 mA (cyan). t_{eff} is the effective time duration of the applied currents (see section 2.10 for details). The initial state was reset by applying an intense negative polarity current of 350 mA. Note that the initial value of the resistance, 78 Ω is recovered within ±1Ω. Top right: model simulations with applied current: $I[a.u.] = 58.5$ (black), 71.5 (green), 84.5 (blue) and 97.5 (red). Middle panels: experimental data for $I = 40$ mA (left) and simulations for $I[a.u.] = 71.5$ (right). τ_1 is defined as the time interval from the beginning of the applied pulse until the resistance starts to drop. Bottom panels: idem in a semi-log plot.

2.4 Resistance switching: the "leakage phase"

After the shock front reaches the boundary point x_{int} the resistance begins to drop. To understand this behaviour, we note that the total resistance of the Schottky barrier is given by the *total number of vacancies* within the barrier region viz. from (2.2) $R_{SB} = \int_{SB} dx A_{SB} u(x)$. As a result, the resistance drop per unit time is approximately given by the ionic vacancy-current passing through the SB-bulk interface at x_{int},

$$dR(t)/dt = -A_{SB} j(x = x_{int}) \tag{2.5}$$

since $R_{SB} \gg R_B$ as $A_{SB} \gg A_B$. Notice that during the propagation phase the ionic current through the interface x_{int} is negligibly small. This is because the initial vacancy concentration there, and hence the local field, are also negligibly small. However, when the shock wave front eventually reaches the end of the SB region, after travelling for a time τ_1, we do expect a sudden resistance drop as a large number of ionic vacancies begin to leak out into the bulk region.

We shall now focus on the detailed description of the resistive drop. In Fig.2.4 we show the systematic dependence of $R(t)$ as a function of the applied external (electronic) current. Along with the simulations of the VEOVM, we also present our experimental results measured on a manganite-based ($La_{0.325}Pr_{0.300}Ca_{0.375}MnO_3$) memristive device [61–65] . The experimental setup and device are described in detail in section 2.10 and in [66]. The set of curves were obtained for applied current intensities just above the threshold for the onset of the resistance switch. The goal here was not to demonstrate the fast switching speed of the device, but rather on the contrary, achieve relatively slow switching speeds in order to access the different time scales. In addition, this also minimizes thermal heating effects [66]. We observe that in both, simulation and experiments, the resistance-change rapidly becomes larger and faster with the increase of the applied electric stress intensity. We also observe an overall good qualitative agreement between experiments and model simulations. This is also highlighted by the semi-log plots, which clearly display the two-stage process involved in the resistive switch, before and after the impact time τ_1.

Remarkably, within shock wave scenario, we may also obtain explicit expressions that quantify the resistance change during the leakage phase. Our analysis may be simplified by first noting, from general considerations of shock waves, that their shape at long times becomes "flat", i.e. the gradient of the local density rapidly decreases ($\partial_x u \to 0$) at all points that were overtaken by the shock wave front[54, 57]. Indeed, our data is fully consistent with this observation, as the vacancy density profile within the SB remains approximately "flat" (i.e. spatially constant $u(x,t) = u_{SB}(t)$) at all times after the shock front reaches the interface (see Fig.2.3). Then, within the VEOVM the SB resistance is simply

proportional to the total vacancy concentration within the barrier and we have, $R(t) \approx R_{SB}(t) = A_{SB} x_{int} u_{SB}(t)$. Since the electronic current I is held fixed, the vacancy (i.e. ionic) current through the interface depends only on the vacancy concentration u_{SB} (cf Eq.3.3). Thus, within the VEOVM we obtain a *nonlinear rate equation*, describing the resistance drop during the "leakage phase":

$$\frac{dR}{dt} = -\frac{2DR}{x_{int}} \sinh\left(\frac{IR}{x_{int}}\right). \tag{2.6}$$

Similarly as we showed before for the propagation phase, this equation may be validated by a quantitative fit to the simulation results (see section 2.9). Note that due to the strong nonlinear form of this rate equation, the $R(t)$ response is significantly different from the simple exponential decay expected in the familiar linear case (e.g. in standard RC circuits). Therefore, within the short time scale associated with the initial fast drop of resistance and where the RS is significant ($IR/x_{int} \gg 1$), the present type of nonlinear system is dominated by the activated process and the approximation $\sinh(IR/x_{int}) \approx \frac{1}{2}\exp(IR/x_{int})$ is valid. This enables the approximate solution of the Eq.2.6.

$$R = R_{HI} - \frac{x_{int}}{I} \ln\left(1 + \frac{t}{\tau_2(I)}\right), \tag{2.7}$$

where the time is measured from the "impact" time τ_1 and $\tau_2(I) = \frac{x_{int}^2}{DIR_{HI}} \exp(-IR_{HI}/x_{int})$ (see section 2.11) is the current-dependent characteristic time for the resistance drop.

2.5 Resistivity scaling

An interesting consequence of Eq.2.7 is that it suggests the scaling behaviour of the curves $R(t)$. In fact, one may define the normalized resistance drop $\delta R(t^*) = R - R(\tau_2) / (R_{HI} - R(\tau_2))$ and see from Eq.2.7 that obeys it the scaling form:

$$\delta R(t^*) = 1 - \ln(1 + t^*/\tau_2) / \ln(2), \tag{2.8}$$

In Fig.2.5 we demonstrate that this striking feature is indeed present in both, our experiments and simulations data. In the upper panels of the figure we show the excellent scaling that is achieved, where all the experimental and the simulation curves $R(t)$ from Fig.2.4 were respectively collapsed onto a single one. Moreover, the collapsed data can also be fitted with a slightly more general form of Eq.2.8, that we discuss in section 2.11. Remarkably, in the lower panels of Fig.2.5 we show that a collapse of the data $R(t)$ can also be obtained using the impact time τ_1 as the scaling variable. This is significant, because it shows that a single scaling behavior may include the two phases of the resistive switching

process, namely before and after τ_1. We should mention that the scaling scenario was derived with the assumption of an ohmic behaviour in the I-V characteristics. While this may not be the case in general [66], within the present set of experiments, which are performed near the current threshold of RS, our results indicate that this is a reasonable assumption or at least a valid approximation.

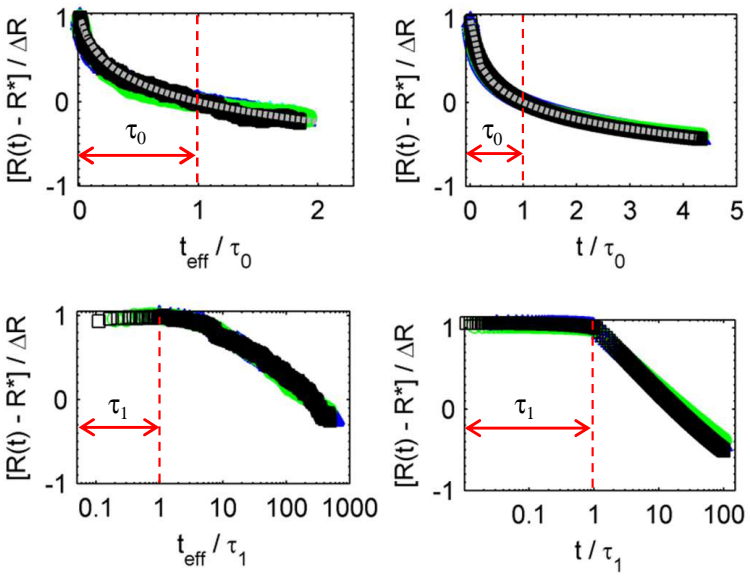

Figure 2.5: Scaled curves of the $R(t)$ data sets of Fig.2.4. The left panels show the collapsed experimental data and the right ones the numerical simulations. The time τ_0 is an auxiliary scaling variable, which is proportional to the characteristic time τ_2 (see section 2.11 for details on the scaling procedure). The scaled data were fitted (white dotted line) with a generalized version of Eq.2.8 (see section 2.11). The lower panels show the same data sets scaled with the shock wave impact time τ_1 (the experimental curves show only three data sets for the lower current values. At higher currents our electronics could not resolve τ_1). To achieve the scaling of the lower panels, we assumed for each plot the normalization value of ΔR determined from the previous scaling (top panels).

2.6 Dynamics of shock waves

In this section, we provide a simple derivation of the Rankine–Hugoniot condition [54, 60] which determines the equation of motion of the shock wave front. An important feature of the shock wave are the spatial discontinuities of u and j. Considering a shock wave front propagating on the interval $[0, d]$ in 1D, we define $u_+ \equiv u(t, x_s(t)+\epsilon)$, $u_- \equiv u(t, x_s(t)-\epsilon)$, $j_+ \equiv j(t, x_s(t)+\epsilon)$ and $j_- \equiv j(t, x_s(t)-\epsilon)$, where $x_s(t)$ is the coordinate of the shock wave front and $\epsilon \to 0^+$ is a infinitesimal positive quantity. According to the continuity equation $\partial_t u + \partial_x j = 0$, we can write:

$$\frac{d}{dt}\left(\int_0^{x_s(t)} u dx + \int_{x_s(t)}^{d} u dx\right) = j(0) - j(d), \tag{2.9}$$

$$\frac{dx_s}{dt}u_- - \frac{dx_s}{dt}u_+ + \int_0^{x_s(t)} \partial_t u dx + \int_{x_s(t)}^{d} \partial_t u dx \;=\; j(0) - j(d). \tag{2.10}$$

Using again the continuity equation, we can immediately determine the shock wave front velocity via the following equation:

$$v_s = \frac{dx_s}{dt} = \frac{j_+ - j_-}{u_+ - u_-} = \frac{\Delta j}{\Delta u}\,|_{x_s}\ , \tag{2.11}$$

which is often called Rankine–Hugoniot condition.

2.7 VEOV model

To simulate the vacancies dynamics we adopted *the voltage enhanced oxygen vacancy migration model* (VEOV), which is a well validated model for the RS effect [58, 67]. We provide here a general description of the model. Taking a capacitor-like device, this model considers a 1 dimensional conductive channel connecting the two contacts, along which oxygen vacancies can migrate through (see Fig. 2.6). This channel is divided in small cells corresponding to physical nano-domains, and at the same time the whole device is divided in two regions: the active interfacial region close to the metal contact (i.e. high resistive Schottky Barrier) and the high conductive bulk region. A diagram of the model with a single active contact, as used in the simulations, is presented at the top panel on Fig.2.6. The resistance of each cell in the channel $r(x)$ is proportional to the local density of vacancies: $r(x) = u(x)A_\alpha$, where $u(x)$ is the density of vacancies on the cell located at x and A_α is a proportionality constant whose magnitude depends on the region of the device: $\alpha = SB, B$, where SB stands for Schottky barrier and B for bulk, and where $A_s \gg A_B$. Migration is assumed to occur

only between neighbours cells, and in each step of the simulation the probability for vacancy migration from a cell at x to its neighbour at $x + \Delta x$ is computed according to:

$$P(x, x + \Delta x) = u(x)(1 - u(x + \Delta x)) \exp(\Delta V(x) - V_0), \tag{2.12}$$

where $\Delta V(x)$ is the drop of voltage (per unit length) at x and V_0 is an activation constant for vacancy migration. In each step of the simulation the migration from cell to cell is computed and the new resistance of each cell is calculated. The total resistance of the device is calculated simply as the addition of all the cells in the channel. For the values used in the simulations, the middle term $(1 - u(x + \Delta x))$ can and will be neglected in the theoretical analysis explained in the following sections. As mentioned in previous sections, this model corresponds to the case of granular materials with activated transport process. To put it in the context of the $generalized - Burgers' equation$ description made in section 2.2, it is easy to see that the drift current originated from this model satisfies the general form $j_{drift} \sim \sinh(E)$. The net current of vacancies generated by the action of an external electric field $E(x) = \partial V(x)/\partial x$, between a cell at x and its neighbour cell at $x + \Delta x$ can be written simply as Fick's-law for the migration probability: $j_{drift} = \partial P/\partial x \approx [P(x, x + \Delta x) - P(x + \Delta x, x))]/\Delta x$, where in the last term the discrete character of the model has been introduced. In particular for our model we take $\Delta x = 1$. Using the definition of P from the model (neglecting its middle term), we get from here that $j_{drift} = P(x, x + \Delta x) - P(x + \Delta x, x) = 2Du \sinh(\Delta V(x))$, where D stands for the Arrhenius factor $\exp(-V_0)$. If the external electric stress is a controlled current I, then $\Delta V(x) = Ir(x) = IA_\alpha u(x)$.

2.8 Simulations details

In order to analyze the existence of a shock wave scenario, the Hi (high-resistance-state) to Lo (low-resistance-state) process was simulated for different external currents. Previously, an initial forming process was performed at which current of different polarities was applied and well defined Hi and Lo states were obtained. In the top-right panel of Fig.2.6 the vacancy profile is shown before and after the forming process. The device starts with a uniform distribution along the channel, and by the end of the forming process the profile shows a characteristic distribution in which vacancies that were originally in the interfacial region migrate to the low-field bulk region where they are accumulated. The figure shows the formed Hi resistance state where it can be seen a second accumulation of vacancies next to the left metal contact in the interfacial region. This second accumulation of vacancies conforms the initial distribution for the Hi to Lo process and it will evolve to form the shock wave during switching as shown in section 2.3. To im-

prove the stability of the simulations the currents were applied using a rise time (from 0 to their actual values) always negligible compared with the characteristic times of the process τ_1 and τ_2 (with rise times in the order of a few thousands of steps). The simulated device contained a total of 1000 cells with a 100 cells long interfacial region (left interface). For the initial distribution a uniform density of $u_0 = 1 \times 10^{-4}$ per cell was used. The value of the activation constant V_0 was set to 16, which corresponds to the activation energy of $0.4eV$ reported in similar manganite systems [8] (i.e. , $0.4eV/k_BT = 0.4/0.026$ at room temperature). For the resistivity constants we used $A_{SB} = 1000$ and $A_B = 1$ (for a table with the parameters see Fig.2.6). For the analysis developed in this work we solely consider the shock wave after it is formed. In the bottom panel of Fig.2.6 we show a standard formation process of the shock wave: the initial narrow accumulation against the metal contact slowly evolves into the shock wave profile.

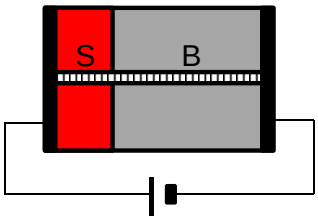

Sim. Parameters	
u_0 (vacancies/cell)	$1x10^{-4}$
A_{SB} (a.u.)	1000
A_B (a.u.)	1
V_0 (units of kT)	16
L (total # of cells)	1000
X_{int} (int. # of cells)	100

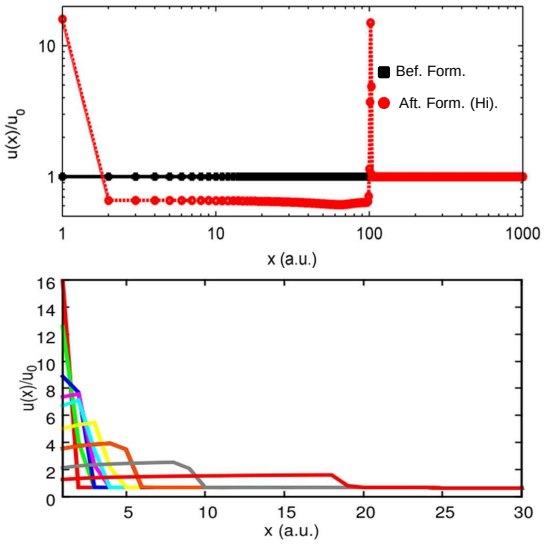

Figure 2.6: Top panels: top-left: Schematic diagram of the VEOV model with a single active contact. The two regions SB and B correspond to the high resistance interface (Schottky Barrier) and the more conductive central bulk, respectively. The small cells within the channel indicate the domains. Top-right: vacancy distribution along the conductive channel before (black squares) and after (red circles) the forming process. The distribution shown after the forming process correspond to a Hi resistance state. Starting from a uniform distribution, during the forming process a characteristic distribution is obtained where vacancies initially at the interface migrates to the low-field bulk region generating a pile-up of vacancies close to the limit between the two regions. In the Hi state, part of these vacancies migrates back to the interfacial region and are accumulated in the vicinity of to the metal contact.Bottom-left (table): parameters used in the simulations. Bottom-right: Snapshots of the shock wave formation in the early stage of simulations (between the first and second snapshot of Fig. 2.3).

2.9 Fitting for the VEOV model

In this section, we explain the details of the comparison between simulation and theory and the procedures used for fitting. Consider the drift current within left interfacial region in VEOV model:

$$j(u,t,x) = P(x, x+\Delta x) - P(x+\Delta x, x) = 2Du \sinh\left(IA_{SB}u\right) \tag{2.13}$$

where the term $1-u(x+\Delta x)$ in the probability has been neglected as explained before [2]. From Rankine–Hugoniot conditions an expression for the shock-wave front velocity $\frac{dx_s}{dt}$ can be obtained, as provided in Eq. (2.4). Performing a redefinition of parameters (for practical reasons only) we can rewrite such equation as:

$$\frac{dx}{dt} = \frac{2D}{x_{int}}\left[\left(1+\frac{\alpha}{\beta}x\right)\sinh\left(\frac{I}{\beta}+\frac{I}{\alpha x}\right) - \frac{\alpha}{\beta}x\sinh\left(\frac{I}{\beta}\right)\right], \tag{2.14}$$

where we used that $u_- = u_+ + \Delta u$, $Q = \Delta u x_s$ is the total number of vacancies carried by shock wave, $Q_B \equiv u_+ x_{int}$ is total number of background vacancies in the left region (being x_{int} the length of the interfacial region), $x \equiv x_s/x_{int}$ is the normalized coordinate, and where we defined the new parameters $\alpha \equiv x_{int}/A_{SB}Q$ and $\beta \equiv x_{int}/A_{SB}Q_B$. From the previous definitions we can write the high resistance value as $R_{HI} = A_{SB}\left(Q_B + Q\right)$ where R_{HI} is a constant determined by the vacancy concentration and independent of I [3].

We can solve then this equation numerically with the material dependent parameters x_{int}, α,β and D. Considering the initial rise time for the current and the non-flatness of the shock wave, an accurate test of the $x_s(t)$ prediction can be performed for $x > x_0 \approx 0.4$ using the integral-form equation:

$$t - t_0 \;=\; \int_{x_0}^{x} \frac{\left(x_{int}/D\right)dy}{2\left(1+\frac{\alpha}{\beta}y\right)\sinh\left(\frac{I}{\beta}+\frac{I}{\alpha y}\right) - \frac{2\alpha}{\beta}y\sinh\left(\frac{I}{\beta}\right)} \tag{2.15}$$

which is used for the fit of the simulation data for $t < \tau_1$ in the lower left panel of Fig.2.3.

On the other hand, we have also the rate equation for the switching (i.e. "leakage") phase (cf. Eq.2.6):

The numerical solution of this equation is used to fit the simulation data in the resistance switching phase for $\tau_1 < t$, shown in Fig.2.7.

[2] The typical value of $u(x)$ in simulation varies between 10^{-4} and 10^{-3}.

[3] There is in fact a small migration of background vacancies into the bulk during the period of shock wave propagation which causes a small variation of the resistance during this phase.

The values of the parameters that enter the equations Eq.2.15 and Eq.2.6 were extracted directly from the simulation results. We find $Q_B = 63.4u_0$, $Q = 15.3u_0$, $A_{SB} = 1000$, $R_{HI} = 7.9a.u.$ and $D = 1.12 \times 10^{-7}$. The very good fits of the simulation data shown in Fig. 2.3 and Fig.2.4 were achieved by slightly relaxing the value of the single parameter x_{int}=100 to the values 94.3 (Fig. 2.3) in the propagation phase and 82.2 (Fig.2.4) in the leakage phase.

The small discrepancy between the relaxed parameters and its actual value mainly comes from the non-flatness of the density profile both during the propagation of the shock wave and during the leaking phase, as well as from the fact that a small part of background vacancies leaks into the bulk during the propagating phase.

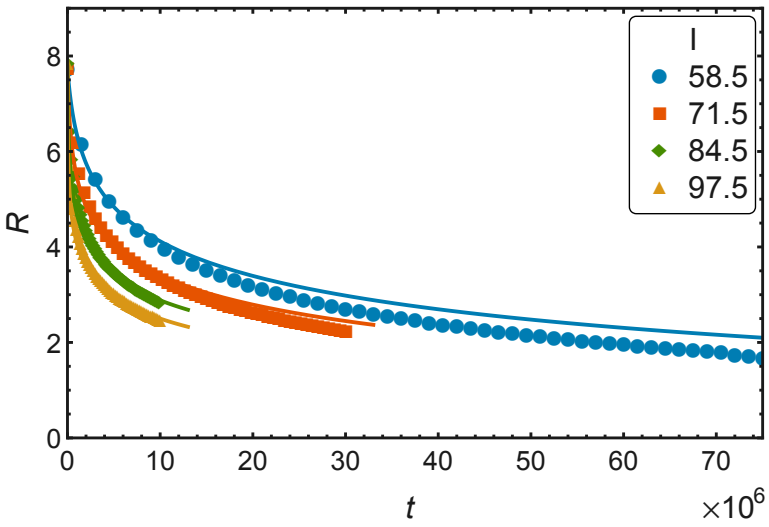

Figure 2.7: Evolution of the resistance during the switching phase for different applied currents according to simulations (dots) and theory (lines) from Eq. (2.6). The currents shown are $I = 58.5a.u., 71.5a.u., 84.5a.u.$ and $97.5a.u.$

2.10 Experimental details

For the experimental validation of our theory, the RS phenomenon was studied in a bulk $La_{0.325}Pr_{0.300}Ca_{0.375}MnO_3$ (LPCMO) polycrystalline sample with hand-painted Ag contacts of approximately 1mm diameter. The device is a parallelepiped of $1 \times 1 \times 10mm^3$, with the contacts painted over the 10mm surface. The distance between contacts is also in the order of 1mm. Measurements were performed using a three wire configuration in order to develop a single contact analysis.

To induce the RS effect an external constant current was used as the electric stimulus. To generate this current and to acquire the data a Keithley 2612 Sourcemeter was employed. The measurements were done using a three wire

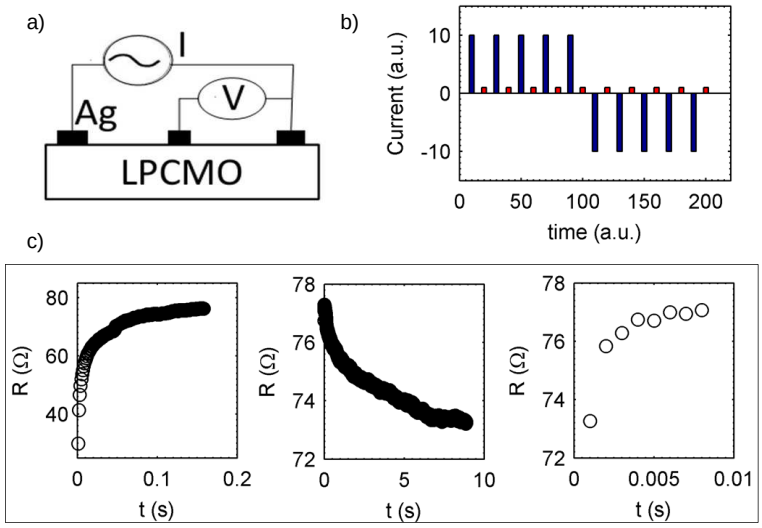

Figure 2.8: (a) Diagram of the experimental set up. (b) Sketch of the pulsed current protocol used in the experiments. A high current Write pulse (blue) is followed by a low current Read pulse (red). The first pulse generates the RS while the second pulse measures the non-volatile resistance. (c) R vs t curves from a complete RS process. The system is first taken to a Hi resistance state under a current of -350mA (left panel). Then the Hi to Lo RS is measured under an applied current of 37.5mA (middle panel). Finally the system is taken back, ie "re-initialized", to a Hi resistance state with the application of a -350mA current.

configuration in order to measure a single interface resistance (Fig.2.8.a). The Hi to Lo RS was studied for currents of different magnitude, as described in section 2.3. More information about the measurement technique and simultaneous contact analysis can be seen in Ref. [61].

The application of current is done following a pulsed protocol: a high current pulse (Write) is followed by a low current pulse (Read). A schematic diagram of the pulsed protocol is shown in (Fig.2.8.b). Each pulse lasts 1ms. Between two pulses there is an interval of about 0.5s, meant to reduce possible heating effects. The time axis exhibited in the R vs t curves (both in Fig.2.4 and in Fig.2.8.c, below) is the effective time elapsed during the actual application of the Write pulses, i.e. disregarding both the 0.5 s timeout and the Reading elapsed time. The Write pulses possess enough strength to change the resistive state of the system, while the Read pulse (low current) measures the remnant (stable, non-volatile) resistance of the device without affecting it. In the experiments shown in previous sections, the Write pulses are in the order of the mA while the Read pulses are in the order of the μA.

The complete measurement process is shown in Fig.2.8.c. To obtain the initial Hi state, pulses of -350mA were applied (Fig.2.8.c, left panel). Next, the desired accumulation experiment is performed, by applying positive pulses of constant

amplitude which decrease the resistance (Fig.2.8.c, middle panel). The initial Hi -resistance state is recovered by applying -350 mA pulses (Fig.2.8.c, right panel). In every case the initial Hi-resistance state obtained was of the same magnitude within a range of about 1%.

2.11 Scaling

In this section, we show that the scaling behaviour is a direct consequence of the strong non-linearity of the drift current $j(u,t,x)$, which depends on local electric field exponentially. In the time range where significant resistive switching occurs, we have ($IR/x_{int} \gg 1$) and we may approximate $\sinh(IR/x_{int}) \approx \frac{1}{2}\exp(IR/x_{int})$. From Eq.(2.6), using a normalized resistance $\widetilde{R} = R/R_{HI}$, we have:

$$\frac{d\widetilde{R}}{dt} = -\frac{D}{x_{int}}\exp\left[\left(\frac{IR_{HI}\widetilde{R}}{x_{int}}\right)(1+\lambda)\right], \tag{2.16}$$

where $\lambda = \frac{x_{int}}{R_{HI}}\ln\widetilde{R}/\left(I\widetilde{R}\right)$ is a small parameter as long as $\widetilde{R}$ close is to 1 (i.e. at the beginning of the resistive change). For simplicity we consider the leading order as we set $\lambda = 0$:

$$\widetilde{R} = 1 - \frac{x_{int}}{IR_{HI}}\ln\left(1+\frac{t^*}{\tau_2}\right), \tag{2.17}$$

where $t^* = t - \tau_1$ is the time measured from the impact time as explained in section 2.4, and τ_2 is a characteristic time for the resistance switch and is dominated by an exponential dependence of the applied current as follows:

$$\tau_2 = \frac{x_{int}^2}{DIR_{HI}}\exp\left(-\frac{IR_{HI}}{x_{int}}\right). \tag{2.18}$$

In Fig.2.9 we use this approximate expression to fit the $R(t)$ simulation data. Comparison with the previous fit done with Eq.2.6 and shown in Fig.2.7 allows us to check that this approximate solution is relatively accurate within the time domain we are interested in for fast switching devices.

Now, using Eq. (2.17), we can show that the I-dependent family curves $R(t)$ should obey scaling. We first consider the normalized resistive change $\delta R(t)$ defined as

$$\delta R(t) = \frac{R(t) - R(\tau_0)}{R_{HI} - R(\tau_0)} \tag{2.19}$$

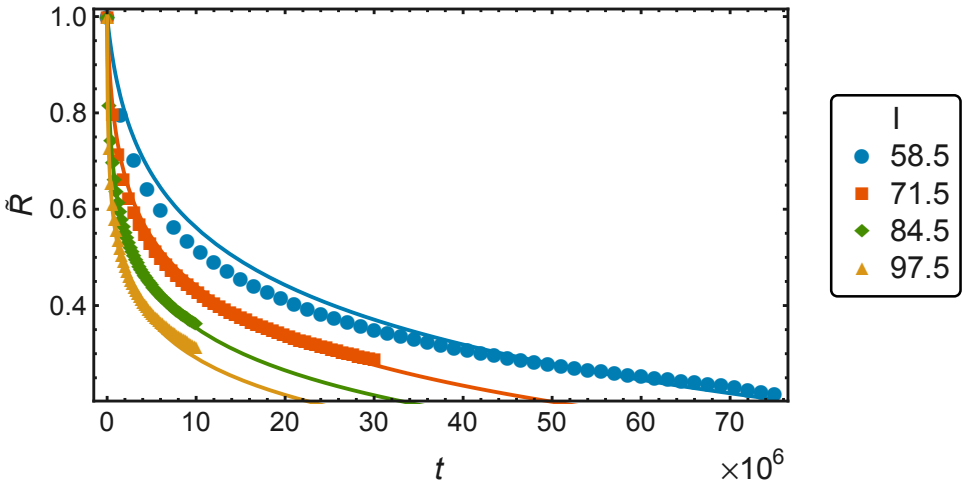

Figure 2.9: Fitting results for the evolution of the normalized resistance according to the Eq. (2.17).

where τ_0 is some yet unspecified time (and we drop the $*$ from t^*). Then, replacing with Eq.2.17 we have,

$$\delta R\,(t) \;=\; \frac{R_{HI} - \frac{x_{int}}{I}\ln(1+\frac{t}{\tau_2}) - R_{HI} + \frac{x_{int}}{I}\ln(1+\frac{\tau_0}{\tau_2})}{R_{HI} - R_{HI} + \frac{x_{int}}{I}\ln(1+\frac{\tau_0}{\tau_2})} \tag{2.20}$$

And rescaling the time by τ_0,

$$\delta R\,(t/\tau_0) \;=\; 1 - \frac{\ln(1+\frac{\tau_0}{\tau_2}\frac{t}{\tau_0})}{\ln(1+\frac{\tau_0}{\tau_2})} \tag{2.21}$$

Notice that with the natural choice of simply setting τ_0 as τ_2, we obtain the scaling form that we presented in section 2.5.

However, in the experiment we do not know, a priori, how to determine the characteristic time scale τ_2, which is a strong function of the current I and other material parameters. So we adopt the following strategy. We use τ_0 as a free scaling parameter, one for each I-dependent curve $R(t)$, that we rescale according to Eq.2.21. We vary the set of values $\tau_0[I]$ until we obtain a collapse of all the experimental and the simulation curves. The results of the successful collapse are shown in Fig.2.5. In our experience, the collapse is unique. A crucial point now is that the collapsed set of curves could be fitted with the expression

$$F(t) = 1 - \frac{\ln(1+ct)}{\ln(1+c)}. \tag{2.22}$$

with c a *current independent* constant. We find the values $c = 15.2$ for the experimental data and $c = 29.4$ for the simulation ones. Hence, in regard of Eqs.2.21 and 2.22 we observe that the constant c is nothing but the ratio between the analytically established characteristic time τ_2 and the empirically determined τ_0, which are simply proportional to one another.

In Fig.2.10 we plot the dependence of the scaling time as a function of the applied current $\tau_0(I)$. In the case of the simulation results, the data follow the same exponentially decreasing behaviour as deduced for $\tau_2(I)$ (see Eq.2.18). Moreover, we find the ratio $\tau_0(I)/\tau_2(I)$ in good agreement with the constant $c = 29.4$, which validates our practical scaling procedure for the determination of the characteristic switching time in the experimental case.

Under the same set of approximations that we have assumed in this section, plus the additional one of neglecting the effect of the background distribution of vacancies, one may also derive an explicit expression for the characteristic time τ_1. We start from Eq. (2.14), and similarly as before, adopt the approximation $\sinh(IR/x_{int}) \approx \frac{1}{2}\exp(IR/x_{int})$. Then, making the substitution $y' = 1/y$ in Eq. (2.15), and assuming that the integral is dominated by the exponential factor (i.e. neglecting the change in lower order factors), the integral has an analytical solution, and we get for the case with no background vacancies (i.e. $1/\beta = 0$)

$$\tau_1 \approx C(t_0, x_0) + \frac{x_{int}^2}{DIR_{HI}} \exp\left(-\frac{IR_{HI}}{x_{int}}\right). \tag{2.23}$$

where the first term is the integration constant determined by the initial conditions t_0 and x_0. If this constant can be neglected (for example for fast forming shock waves) then we have the surprising result that $\tau_1 = \tau_2$.

In the case of the model simulations, the results displayed in Fig.2.10 shows that, in fact, both characteristic times have the same I-dependent exponentially decaying behavior. Moreover, the ratio of the two characteristic times is approximately 25, which is close to the constant $c = 29.4$ quoted before, therefore our simulations also validate the equality between the two characteristic times τ_1 and τ_2 predicted by the shock wave scenario.

As may be expected, the experimental situation is only qualitatively consistent with the previous discussion. As seen in Fig.2.10, for the experimentally determined characteristic times, we observe that they have approximately a similar dependence with the applied current, however, it is less clear if the equality between them also holds.

We show and compare the evolution of both characteristic times under different applied current in Fig.2.10 for both simulations and experiments, observing a good agreement with the analysis presented here.

2.12 Quantitative comparison: experiments & simulations

The magnitudes of the main parameters used in the simulations can be related to actual experimental magnitudes. In our model all voltages are normalized by

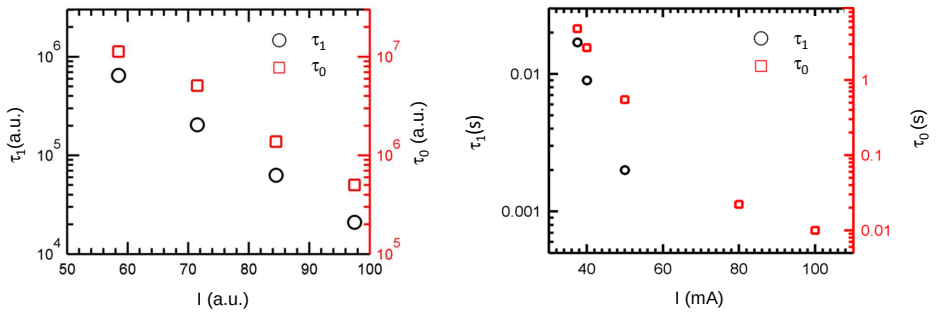

Figure 2.10: Evolution of the characteristic times for different applied currents for both simulations (left panel) and experiments (right panel). It can be seen that both times follow an approximate exponential dependence with I, and that there exists a relative proportionality between them as predicted by our analysis.

k_BT/e and energies by k_BT. As experiments were performed at room temperature, we have $k_BT/e \approx 26$ mV and $k_BT \approx 0.026$ eV. In the simulations the activation energy constant was given a value of $V_0 = 16\ k_BT \approx 0.4eV$, which is consistent with experimental values reported for similar PCMO devices [8]. A correspondence can also be established for the voltages adopted in experiments and simulations. In the former the applied voltages used for the resistive-commutation were in the order of 1V. In units of k_BT/e this leads to the dimensionless voltage values in the order of a few tens (1V/26mV = 38.5). However, in order to perform the extensive computational work required by our study within reasonable computational times, the values adopted in the simulations were higher by about one order of magnitude. For evident practical reasons (equipment and device limitations) such an increase of applied voltage cannot be performed in the experiments. Nevertheless, it should be clear from our theoretical discussion of the mathematical nature of the equations, that the same qualitative results, namely formation of shock waves, also remain valid at lower applied voltages. Despite the significantly higher computational cost (days versus hours), we present here a set of runs for voltages that are close to the experimental values. In figure 2.11, we show the results for a simulation with an applied dimensionless current $I = 6.75$, which corresponds to a physical units $V = 1.4$V, since the initial (dimensionless) $R = 8$ and then $V = IRk_BT/e = 6.75 \times 8 \times 26\text{mV} \approx 1.4\text{V}$. For convenience, in the figure we also reproduce the corresponding results from section 2.3 for a simulated voltage of $V = 14.87V$ ($I = 71.5a.u.$).

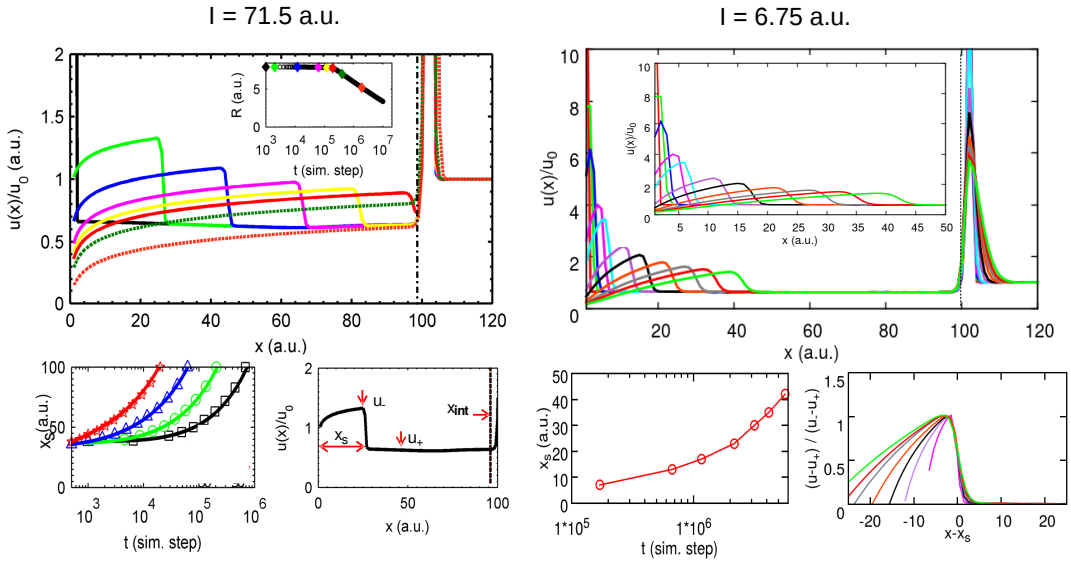

Figure 2.11: Shock wave dynamics for two different applied currents, which differ by nearly an order of magnitude. The lower current case (right panel) corresponds to applied voltages comparable to the experimental ones, and the higher current cases (left panel, same as FIG. 2) show similar shock wave dynamics. The two lower right panels demonstrate: (i) that the propagation of the shock wave front remains qualitatively the same as for higher applied currents, and (ii) the collapse of the snap-shots of successive profiles, due to the formation of the shock-wave.

Ondas de Choque en Óxidos de Metales de Transición

En este capítulo se estudió el fenómeno de Conmutación Resistiva en óxidos de Metales de Transición. Se analizó el caso de CR bipolar causada por migración de vacancias de oxígeno entre dos regiones del material: una interfaz de alta resistividad y el bulk semoconductor. Se mostró que la migración iónica puede ser descripta por una generalización de la ecuación de Brurgers, que bajo condiciones muy generales tiene como soluciones ondas de choque. Este escenario fue validado por medio de desarrollo analítico y comparación con experimentos realizados en un dispositivo memristor basado en la manganita LCMO.

Chapter 3

Shock waves in binary oxides memristors

In the previous section it has been proposed a connection between the RS phenomenon and the formation of shock waves, a classical topic of nonlinear dynamics. It has been argued that the profile of oxygen vacancies that migrate during the resistive change forms a shock wave (SW) that propagates through a high resistive interfacial region and leaks onto the bulk of the device. There the analysis was focused in complex oxides, and experiments in manganite-based devices were presented. In that kind of systems the oxygen vacancies act as scattering centers for the conduction electrons, increasing the local resistance of the material. When ions migrate under an external voltage, the local electric field may strongly depend on the local ion concentration; this effect is the key source of nonlinearity causing the formation of shock waves and very sudden resistance switching. However in a different kind of relevant systems, such as binary oxides (HfO_2, TiO_2) the oxygen vacancies play the opposite role in their conducting properties. In these particular systems the oxygen vacancies dope electron carriers to an otherwise good insulator, decreasing the local resistance of the material. In the present work we will extend the study of SW formation to binary oxides. First we will provide a general introduction to the shock wave formalism for these systems. Then we will adopt a specific model for ionic migration in RS and we will present novel simulations validating our results.

3.1 Generalized Burgers' equation and SW dynamics in binary oxides

When ions migrate through a *conducting* medium under the influence of strong applied voltages, they are likely to undergo a nonlinear diffusion process, as we explained in the previous section. In the case of binary oxides such as TiO_2,

the oxygen vacancies dope electron carriers. Hence, oxygen deficiency should decrease the resistance and, equivalently, the resistivity $\rho(u_O)$ must be a monotonically increasing function of the local oxygen density $u_O(x,t)$ Therefore, the redistribution of the local oxygen-ion density results in the change of local resistivities and, consequently, of the local electric fields, which further promotes the non-linear effect in the drift. Thus, in these systems and under the experimentally relevant case where the transverse currents may be neglected, the problem simplifies to the generalized *Burgers'* equation for local oxygen density,

$$\partial_t u_O + f\left(u_O\right)\partial_x u_O = D\partial_{xx} u_O, \tag{3.1}$$

where $f\left(u_O\right) \equiv \partial_{u_O} j_{drift}\left(u_O, I\right)$, and $I(t)$ is the magnitude of the electronic current.

As explained in previous sections, it is now widely accepted that the mechanism of the bipolar (i.e., polarity-dependent) RS in transition metal oxide memristors is due to the induced changes in the spatial distribution of oxygen. In the particular case of binary oxides (such as TiO_2 or HfO_2), the bipolar RS is often observed after an electroforming process that renders the highly insulating system poorly conductive by creating a path with a massive production of oxygen vacancies. In an extreme case, this path may become a purely metallic filament, which leads to the so-called nonpolar resistive switching mode. However, if this is not so drastic, one gets to the bipolar switching mode with an intermediate density of oxygen vacancies [68]. Within such a conductive path, oxygen ions move through the oxygen-vacancy sites by means of the applied electric field. As local oxygen density increases, the system locally approaches the stoichiometric formula, hence becoming locally more insulating with a local increase of resistivity. The local increase of resistivity leads to higher local voltage drops, and hence higher local electric fields, which further promote a higher motion of oxygen ions, leading to the formation of the shock wave.

3.2 Model system and results

Following the work presented in the previous section (and Ref.[69]), to analyze the RS in binary oxides we will adopt the *voltage-enhanced oxygen-vacancy migration model* [58] (VEOVM), which corresponds to granular materials with activated transport process. This model has been previously used for manganite devices [58] and will be adapted here for the case of binary oxides. Within the framework of this model, we shall perform numerical simulations to validate our shock-wave scenario. This model assumes a discretized 1-D conducting path with two metal metal-electrodes at x=0 and x=L, being L the length of the device (see Fig.3.1). This model assumes that the resistance of each discretized region of

the path ("cell") is a function of the local ionic concentration. For the case of binary oxides and motivated by the expected approximate linearity of the *conductivity* with the concentration of dopants, namely, oxygen vacancies (u_{OV}), $\sigma = 1/\rho \sim u_{OV} = (n - u_O)$, we will assume

$$\rho\,(u_O) \;=\; \frac{\rho_0}{1 + A_0\,(n - u_O)} \tag{3.2}$$

where n is the number of oxygen atoms in the unit formula, ρ_0 is the intrinsic resistivity of the stoichiometric system (i.e., for u_O=n) and A_0 is a suitable constant. Thus, $\rho\,(u_O)$ is a monotonically increasing nonlinear function of u_O. Under the action of the external stress (electric current I), the local fields at each cell position x are computed at every discrete time step t. The field-driven migration of oxygen is simulated computing the local ionic migration rates from cell x to $x+\Delta x$ as [58]

$$P(x, x + \Delta x) = u_O(x)[1 - u_O(x + \Delta x)] \exp\left(\frac{-V_0 + qI\rho(x)}{k_B T}\right), \tag{3.3}$$

For simplicity we will take the ionic charge q=1, k_BT=1 and $n = 1$. The parameter V_0 denotes the activation energy for ionic diffusion. The new profile $u_O(x, t)$ is updated from the migration rates, and from Eq.(3.2) we get the new total (two point) $R(t)$ as the discrete x-integral of the local cell's resistance $\rho(x, t)$. The unit of time in our simulations is the discretized time-step while the resistance and the current are in arbitrary units.

Following the work done for manganite devices, we will focus on the high-to-low resistance transition.

We build an initial high resistance state (R_{HI}) by applying a constant current to a pristine sample with uniform distribution u^0, which generates an accumulation of oxygen atoms against the left electrode at $x = 0$. Then we apply a pulse of current $I(t)$ with opposite polarity and observe the evolution of the oxygen profile as a function of the (simulation) time. To improve the stability of the simulations the pulse includes an initial rise time where the current increases from 0 to I in a short time, after which it is held constant. In Fig.3.1 (left panel) we show snapshots of the oxygen distribution during the application of the pulse. The black curve corresponds to the initial distribution (i.e. R_{HI} state). We see that, under the external current, the profile evolves with a shock wave form with a sharply defined front. It is important to notice that the formation of the SW is independent of the specific shape of the initial distribution. In Fig.3.1 (right panel) we show simulations for a triangular initial distribution, where we see that there is a rapid evolution of the oxygen profile into a shock wave form and the initial condition is rapidly forgotten. For simplicity we will focus in the initial squared profile for our following analysis.

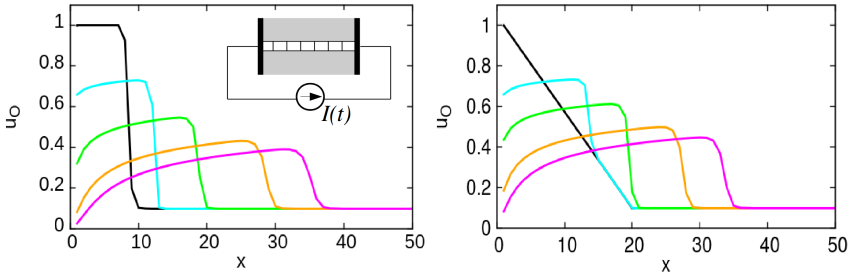

Figure 3.1: Simulations of the VEOVM model. In the model the resistance of a capacitor-like device is governed by a 1D conducting path with a high concentration of oxygen vacancies within an insulating binary oxide. The migration of oxygen ions along the discretized path is induced by an external current, which modifies the resistance of the system (see diagram in the inset). Main panels: Snap shots of the time evolution of the oxygen density profile in a simulation of the VEOVM model. We show the shock wave evolution and formation under two different initial conditions (initial squared profile (left) and triangular profile(right)). The black curves correspond to the initial oxygen profile ($t = 0$). We see that the SW is rapidly form "forgotten" the initial condition. The time steps of the successive profiles of the left panel can be read off from the corresponding color dots in the $R(t)$ plot of Fig.3.3. The model parameters used were $I = 0.3$, $L = 1000$, $u^0 = 0.1$, $V_o = 16$, $A_o = 100$ and $q = kT = 1$. To improve the stability of the simulations, the current is gradually (linearly) increased from 0 to $I = 0.3$ between $t = 0$ and $t = 3000$, after which it is held constant. The initial squared condition (left panel) is generated by applying a constant current $I = -1.0$ during a period of 4000 simulation steps over a pristine sample with uniform distribution u^0.

First we will analyze the evolution of the SW front x_S as a function of time. To gain analytical insight on x_S, we recall that the velocity of the shock wave front dx_s/dt is very generally given by the Rankine–Hugoniot conditions [54, 60], which express it as the ratio of the spatial discontinuity of the (oxygen) drift current, and the spatial discontinuity of the density profile across the shock viz. $dx_s/dt = \Delta j/\Delta u\,|_{x_s}$. Within the VEOVM model [58], the following *nonlinear rate equation* is obtained (see Ref. [69] for details), which describes the dynamics of the shock wave front:

$$\frac{dx_s}{dt} = \frac{2Du_{O,-}\sinh\left(I\rho(u_{O,-})\right) - 2Du_{O,+}\sinh\left(I\rho(u_{O,+})\right)}{\Delta u_O}, \tag{3.4}$$

where D is a prefactor related to the activation energy for oxygen migration (Arrhenius factor) (see Eq.3.1 and Ref.[58]), and $u_{O-/+}$ are the density of oxygen at the two sides of the shock wave front (see Fig.3.2, left panel). In Fig.3.3 (right panel) we show the results obtained from the numerical integration of Eq.3.4 (solid

blue line) together with the results from simulations (red dots). To perform this integration we write $u_{O,-}(t)$ in terms of $x_S(t)$ by assuming $u_{O,-}(t) \approx Q_{SW}/x_S(t)$, being Q_{SW} the total number of oxygen ions migrating within the shock wave (which will be assumed constant) and we take $u_{O,+} \approx u^0$. We use Q_{SW} as a free parameter to better reproduce the results of the simulations, obtaining $Q_{SW} = 8.95$. This is consistent with the value of Q_{SW} that can be estimated from the initial oxygen profile, i.e. $Q_{SW} = x_S(t=0)u_{O,-}(t=0) \approx 10$ (see Fig.3.2, right panel).

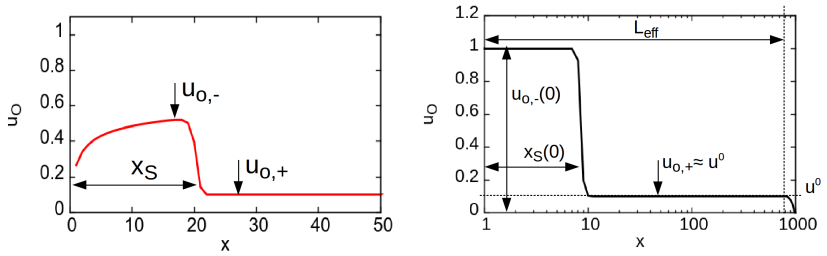

Figure 3.2: Left panel: Diagram of the SW profile. The main parameters are indicated. Right panel: Detail of the initial distribution (R_{HI} state). As explained in the text, the initial state is generated by applying a constant current over the pristine sample that induces the migration of oxygen ions from the right to the left contact. This creates an asymmetric distribution with a pile-up of ions at $x \approx 0$ and an "empty" region (low concentration) at $x \approx L$ (for $x > L_{eff}$ in the plot). The distribution in the intermediate region remains approximately uniform. We show in the plot the relevant parameters used for the integration of Eqs. 3.4 and 3.6.

Having established the formation of shock waves during the oxygen migration, we now proceed to the analysis of the resistance during this process.

The total (two point) resistance of the system is given by,

$$R(t) = \int_{x=0}^{x=L} \rho\left(u_O(x)\right) dx, \tag{3.5}$$

Using Q_{SW} and $u_{O,+}$ as defined before, the resistance can be reparametrized as a function of the shock wave front position x_s as

$$R\left[x_S(t)\right] = \frac{\rho_0 x_S}{1 + A_0\left(n - \frac{Q_{SW}}{x_S}\right)} + \frac{\rho_0\left(L_{eff} - x_S\right)}{1 + A_0\left(n - u_{O,+}\right)}, \tag{3.6}$$

where L_{eff} is the effective length of the device (see Fig.3.2, right panel). In Fig.3.3 (left panel) we show the evolution of the resistance $R(t)$ from simulations (red curve) together with the one obtained from Eq.3.6 (yellow line). For $x_S(t)$ we use the numerical integration performed for Eq.3.4 (Fig.3.3, right panel). We

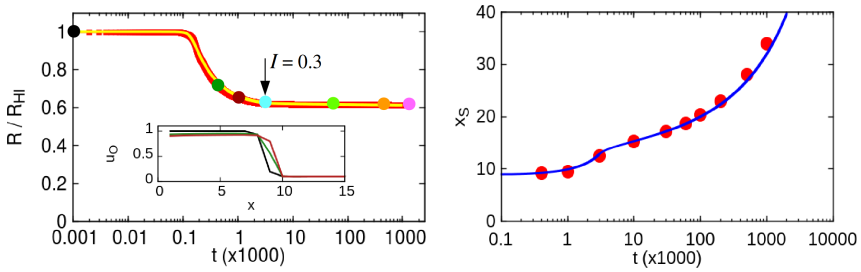

Figure 3.3: Left panel: Evolution of the resistance during oxygen migration. We show the results of the simulations (red curve) together with $R[x_S(t)]$ from Eq.3.6 (yellow line). The coloured dots indicate the time of each snapshot shown in Fig.3.1 (left panel) and in the inset of this figure. The arrow at $t = 3000$ indicates the end of the initial rise time for the current. Inset: Snapshots of oxygen profile at short times after the application of the pulse. Right panel: Evolution of the shock-wave front position $x_S(t)$. We show the simulations results (red dots) together with the integration of Eq.3.4 (blue solid line). We recall that the external stress (current) is linearly turned on between $t = 0$ and $t = 3000$ (see section 2.3 and caption of Fig.3.1), after which it is held constant. This explains the change of tendency observed at the end of that period.

used L_{eff} as a free parameter to better reproduce the simulations, obtaining $L_{eff} = 800$, in reasonable agreement with the simulation (see Fig.3.2, right panel). As a final remark we notice that the main part of the resistance change takes place during the early stages of the SW dynamics. In the inset of Fig.3.3 (left panel) we show snapshots of the density profile at $t = 400$ and $t = 1000$. Due to the non-linear dependence in $\rho(u_O)$, small changes in the oxygen profile lead to big changes in the resistance of the system.

Ondas de Choque en Óxidos Binarios

En este capítulo se estudió el fenómeno de Conmutación Resistiva bipolar en Óxidos Binarios. Se extendió el formalismo presentado en el capítulo anterior y se mostró que la formación de ondas de choque también se puede dar en estos sistemas. Este tipo de materiales (que incluye al TiO_2 y al HfO_2) son de gran relevancia para aplicaciones tecnológicas y son hoy en día intensamente investigados.

Chapter 4

Volatile RS in strongly correlated systems. Towards the implementation of artificial neurons

In this chapter we consider the phenomenon of electric Mott transition (EMT), which is an electric induced insulator to metal transition. Experimentally, it is observed that depending on the magnitude of the electric excitation the final state may show a short lived or a long lived resistance change. We extend a previous model for the EMT to include the effect of local structural distortions through an elastic energy term. We find that by strong electric pulsing the induced metastable phase may become further stabilized by the electro-elastic effect. We present a systematic study of the model by numerical simulations and compare the results to new experiments in Mott insulators of the AM_4Q_8 family. Our work significantly extends the scope of our recently introduced leaky-integrate-and-fire Mott-neuron [P. Stoliar Adv Mat 2017] to bring new insight on the physical mechanism of its relaxation. This is a key feature for future neuromorphic circuit implementations.

4.1 Introduction

Recently an "artificial neuron" which implements the functionality of a leaky-integrate-and-fire (LIF) biological spiking neuron has been presented [53]. strongly correlated systems that exhibit metal-insulator transitions [16].

In the LIF model, a neuron is excited by a train of incoming electric pulses (spikes), which are *integrated* in time by the neuron, until it reaches a threshold level where it *fires* a spike. The "fire" event in the Mott neuron corresponds to

an Electric Mott Transition (EMT), that is the resistance collapse of the Mott insulator. The *leaky* property models the fact that in the "down" time in-between pulses the excitation level of the neuron slowly decays with a given relaxation time constant. In this Chapter we shall gain insight in this key feature of the LIF model, namely the "leaky" property and shall also extend our model presented in [53] to study the recovery behavior of the Mott neuron right after the firing event which is corresponding to the "refractory period" of a biological neuron. Evidently, for a neuron to reach a threshold and fire, the time-delay between arriving pulses has to be shorter than the relaxation time constant of that neuron [42]. Therefore, the control of the "leaky time" is a key issue. On the other hand, the "refractory time" of a biological neuron refers to the period of time *right after* the fire event while the neuron cannot fire again. As we shall see below, in our artificial Mott neuron model both features are related to the same underlying mechanism, which leads to two characteristic relaxation times of the system.

One may naively expect that the relaxation time would be an intrinsic constant of the material, however the situation is more complex since the artificial neurons are based on strongly correlated Mott materials that undergo insulator-metal phase transitions. In systems in equilibrium, Mott transitions can be induced and controlled by a variety of parameters, such as pressure, chemical doping and temperature (see Introduction). However, in the present situation, the understanding of the relaxation is further complicated by the fact that the LIF functionality is a property of the system out-of-equilibrium. That is, when the Electric Mott Transition (EMT) is induced by pulses of electric field that provoke a partial dielectric breakdown. During this breakdown, the resistance collapses [41, 42], and eventually recovers back to the original value after the application of the electric pulse is terminated. The theoretical understanding of the recovery of a Mott insulator from the collapsed resistance state is a challenging many-body out of equilibrium problem of actual interest [40].

Experiments of EMT show that the relaxation from the low to the high-resistance state of a Mott insulator depends significantly on the strength of the applied electric field [14]. In fact, the systematic study of the field induced dielectric breakdown in the Mott system $GaTa_4Se_8$ and similar compounds revealed the existence of three different regimes: (i) at low applied electric fields there is, of course, no large resistance change, (ii) at intermediate field strength there is a *volatile* change of resistance, that is, there is an initial sudden collapse followed by a recovery. And (iii) at high fields there is a seemingly *non-volatile* change of resistance, that is, the resistance collapses and does not recover or may take very long time (i.e., the retention time is virtually infinity). In our artificial neuron model, we associate the duration of the resistance recovery to the "refractory period" mentioned above, and its characteristic time will be termed *retention*

time.

We should note that the resistive change in regime (ii) is a perfectly reproducible effect and the breakdown occurs after a delay-time t_D (of the order of μs to ms), strongly dependent on the applied voltage [14]. When the applied voltage pulse is terminated, the low resistance relaxes back to the original high value in a characteristic time that we shall denote τ_R [53]. In contrast, in regime (iii) the resistance change is permanent, i.e. $\tau_R \to \infty$, but the resistive changes are more difficult to control and reproduce.

In previous works, a model that accounts fairly well for the basic phenomenology of the EMT have been introduced [42]. However, that model has a single relaxation time for the recovery of the "broken-down" metallic regions back to the initial Mott insulator state. This feature clearly cannot account for the observation of the regime (iii) described above, and neither to the behavior of τ_R with applied pulse strength in regime (ii) as is observed in the experiments that we shall report here. Thus, the main goal of the present work is to extend the previous model to capture the behavior of the relaxation time in the experiments of the EMT. We shall show that by introducing an electro-elastic effect, the relaxation time τ_R will display a non-trivial behavior. For instance, we shall show that the duration of the relaxation will depend on the volume fraction that has changed from Mott-insulator to metal during the application of the voltage pulses. Related to this and relevant for experiments, we shall see that by application of a higher voltage strength and/or a longer pulse duration one may induce the growth of *thicker* metallic filaments and achieve a significant increase of the relaxation time.

Before introducing the model we should clarify a few important points, which connect the present study to a model of a neuron analogue aimed at the implementation of bio-inspired neural networks. The resistive collapse is considered to result from a two-step process. The initial one where the strong applied field enhances the rate of phase change and a larger number of isolated small regions of the insulating material turn metallic. If the production rate is sufficiently large, more than the rate of relaxation of those regions back to the insulator state, then the density of metallic regions will steadily increase. Eventually it will reach a critical density where a sudden avalanche-like process will create a filament [42]. The resistance change during the first part of the process is quite small, and the collapse of its value is due to the formation of the filament or, if the applied voltage is strong, of more filaments at random positions, further reducing the resistance. That initial model assumed a single intrinsic time for the relaxation of metallic regions back to insulator state, irrespective of whether it belonged to an isolated region or was part of a filamentary structure. This feature will be partially modified in the model introduced in the present work. We shall make

the additional assumption that the relaxation probability of a given cell depends on the current state of its neighboring cells. Hence, a metallic cell will effectively have a different relaxation rate depending whether it is an isolated one or it is within a filamentary structure. The model will aim to describe the whole process of resistance collapse and recovery, namely the filament formation and its reabsorption. The *leaky-time* of a neuron analogue model [53] is associated to the dynamics of the neuron in between arriving pulses *before* the fire. Correspondingly, in the context of the present model, the leaky behavior is associated to the behavior of the system during the initial filamentary formation process. More specifically, with the initial stage where the density of isolated metallic regions increase until the critical density is attained and with the ensuing rapid growth of the filamentary structure. Experimentally, this leaky stage may be explored and characterized by the application of short electric pulses [53]. In contrast, there is a process of reabsorption of a formed filament, which corresponds to the resistance recovery from low to high, that begins when the pulse is terminated after the fire event (see Fig.1) This process is what one would associate to the "refractory-time" of a biological neuron. However, there is a significant difference between the refractory time of a biological neuron and the Mott neuron. In the former, the neuron is "off" during the refractory time, that is, arriving spikes cannot induce a new action potential. In the Mott neuron, in contrast, the system is in the low resistance state, which means that arriving pulses will generate current pulses. Because of this difference, we term the recovery of the high-resistance state (i.e. filament reabsorption and rupture) as "recovery time" instead of refractory time (see Fig. 4.1).

As we shall see from the study of the simulation results of our model, the leaky process corresponds to the relaxation of *isolated* metallic regions in an essentially insulating system, while the recovery period corresponds to the rupture or depercolation process of already formed metallic filaments. We shall see that both the leaky and the recovery phases are captured by our model. As we shall also show in experiments that we report here, our modeling work provides useful insight for the control of these relevant neuronal model features.

4.2 The model

We start from the model introduced by Stoliar et al. [42] that consists of a 2D resistor-network where each element of the network represents a small (nanoscale) region of the physical Mott system [42, 70]. The cells of the network are assumed to be large enough so that its electronic state is well defined. Imaging technique experiments with nanoscale spatial resolution have shown that across the Mott transition there is a coexistence of metallic and insulating phases with inhomoge-

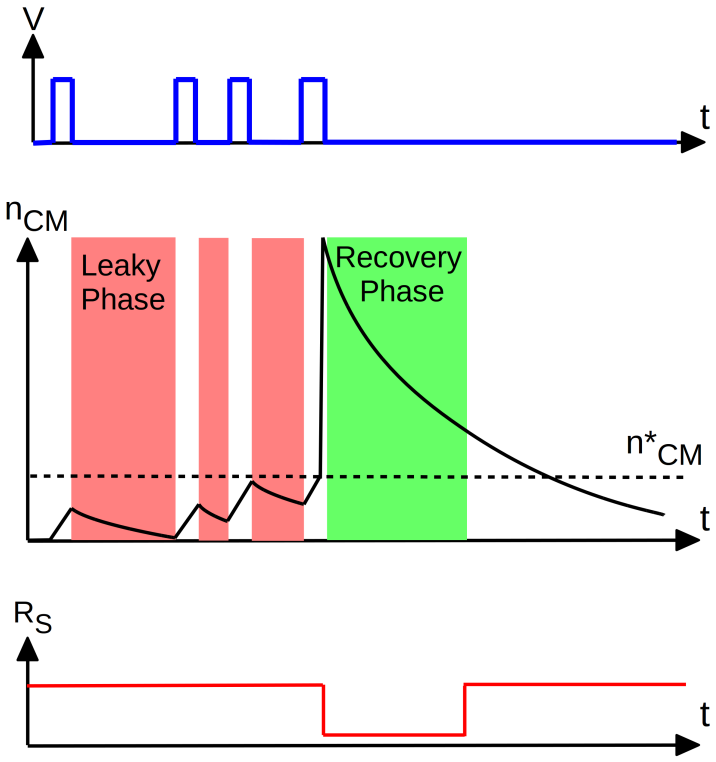

Figure 4.1: The leaky and recovery phases are respectively depicted in red and green. The first takes place in-between pulses and the second after the Electric Mott Transition (EMT), that is, after the neuron fires.

neous distributions down to the few nanometers [71, 72]. Each cell site is assumed to be in one of two electronic states: Mott-insulator (MI) or correlated-metal (CM). These states are respectively associated with a high and a low resistance values, R_{MI} and R_{CM}. The resistor network model is schematically shown in Fig.5.1.a-b. Since the experimental systems are normally in the insulator state, the model assumes that the MI-state is the lowest in energy, which is defined as the reference $E_{MI} = 0$. The CM-state is assumed to be a *metastable* state, with a higher energy E_{CM} , and separated from the MI-state by an energy barrier E_B^E of pure electronic origin (see Fig.4.3.a). From Dynamical Mean Field Theory calculations of the Hubbard model for Mott systems [12, 31], one may expect that the energy difference between these states may be of the order of a few tens of meV, substantially smaller than the electronic bandwidth .

In the present numerical study we follow the methodology of Ref. [42]. In analogy to the actual experimental setup, we adopt an electric circuit with a constant *load* resistance R_L, as shown in Fig.5.1.a. Thus, the resistance of the system R_S and R_L form a voltage divisor circuit. Denoting $V(t)$ the externally applied voltage protocol, then the voltage on the resistor network is given by $V_S(t) = \frac{R_S(t)}{R_S(t)+R_L} V(t)$. The external voltage can be set as any arbitrary profile

$V(t)$, which upon discretization of the time becomes $V(t_i)$ at each time-step t_i. Initially, all lattice cells are assumed in the MI state. Then, at every time step t_i the full resistor network circuit is solved, obtaining all the local voltage drops ΔV_{ij} at each cell site ij, and the total resistance $R_S(t_i)$ between the top and bottom electrodes. For simplicity the electrodes are assumed perfectly metallic (see Fig.5.1.b) [42].

At each time step, the state of the resistor network is updated following the procedure of Ref. [42]. The probability for a given insulator cell to undergo a local EMT, that is from MI to CM at time step t_i is given by $P_{MI\to CM} = \nu e^{-(E_B^E - e\Delta V(t_i)/kT)}$, where the constant ν is an attempt rate, e is the charge of the electron, $\Delta V(t_i)$ is the computed local voltage drop at the given cell, k is the Boltzmann constant and T the temperature. This is an Arrhenius like law, where the key feature is that the local electric field increases the probability for the cell undergoing a local EMT. This assumption should (hopefully) be fully supported by out of equilibrium many body calculations.

A crucial ingredient of the model is the metastability of the CM-state. In fact, if a given cell undergoes a MI→CM transition, then the metastable CM-state may relax back to the MI one. The transition rate for the relaxation is also given by an Arrhenius like expression $P_{CM\to MI} = \nu e^{-(E_B^E - E_{CM})/kT}$, hence the model has a fixed relaxation time τ_R. We note that the in this relaxation process the field $e\Delta V$ may be omitted since $R_{CM} << R_{MI}$, so the voltage drop effect is neglected in the CM sites.

Thus, in the numerical simulation the 2D resistor network is solved at each time-step t_i for a given protocol $V(t_i)$. The local voltage drops $\Delta V_{ij}(t_i)$ are computed for all cells ij. The state of the cells is updated according to the above probabilities. This gives a new value of the total (two point) resistance $R_S(t_i)$ of the system, and then the simulation proceeds. We adopt $\nu = e = kT = 1$. The unit of time in our simulations is the discretized time-step and the voltage is in arbitrary units.

The previous numerical studies [42, 70] showed that the resistive collapse in the EMT is due to the sudden formation of filamentary structures of CM phase, which connect the two electrodes. These structures grow, as expected, along the electric field lines. Less evident was the observation that while right after the percolation the filament connecting the two electrodes is quite inhomogeneous, it nevertheless continues to evolve till it rapidly reaches a rather homogeneous thickness [42]. This is illustrated in panel (a) of Fig.4.4. Since the numerical solution of the 2D resistor network is, by far, the most time consuming part of the numerical simulation, motivated by the previous observations, we explore a simplification of the simulation of the model that would dramatically boost the computational time.

This feature suggests that the transverse currents, i.e. perpendicular to the direction of the applied field, may not play a crucial role, at least after some irrelevant brief transient time. Therefore we numerically explored the possibility of neglecting the transverse currents altogether in our simulations. In Figs.4.4.b-d, we show a comparison of typical experimental data of the EMT for various applied external voltages and the respective result of the simulations for the 2D model (panel c) and for the case where the transverse currents were neglected (panel d). We see that the later simulations qualitatively capture the behavior, very similarly as in the 2D model [42]. In the present case, one should consider the thickness of the 1D filament (one cell) as a coarse grained version of the previous 2D one.

This simplification leads to a dramatic speedup of the simulations. In fact, instead of solving a 2D resistor matrix, we simply have a collection of 1D series resistor chains, which is trivially solved. This enabled us also to consider significantly larger systems and, more important, to simulate for longer times. This turns to be crucial for the systematic study of relaxation effects, which are relatively much longer than the typical time to dielectric breakdown. In addition, it makes possible a simpler analytical insight, which we will develop in the following sections.

This model has already provided valuable insights and very good qualitative agreement with experiments, such as the existence of a threshold field and the decrease of the delay time of the resistance collapse with the increase of the applied voltage [42]. However, as it stands, if fails to capture the existence of different relaxation regimes (ii) and (iii) as described in the Introduction. In fact, the model has a single intrinsic relaxation time, which is solely set by the energy difference between the electronic energy barrier and the metastable CM-state, $\Delta E = E_B^E - E_{CM}$.

Thus, in order to qualitatively capture the observed experimental behavior where strong voltage pulsing may realize low resistance states that are long-lived, we shall extend the model by making an additional assumption. Specifically, we shall introduce the energy cost associated to the formation of a MI-CM boundary interface. We may rationalize this as an elastic energy that originates from the structural strain created at the boundary between the two distinct electronic phases. In fact, experimentally, using STM techniques, it has been observed a giant electro-mechanical effect that was interpreted as a strong self-compression of the lattice structure in the metal state [72]. Therefore, we add to the model the assumption of an elastic deformation energy E_{EL}, which is a supplementary energy cost associated to the transition when two nearest neighbor cells would end in different states. In other words, it is an energy penalty for creating spatial inhomogeneities. As we shall see, this assumption creates *spatial correlations* in

the way that multiple filaments grow. In our previous model, filaments would grow at random, essentially uncorrelated positions, across the system. However, the addition of the elastic energy promotes the grow of new filaments neighboring a previous one. Thus promoting the thickening of filamentary structures.

The simplest way to include this in the model is by adding this effect into the definition of the energy barrier.

Thus, we may write the energy of the barrier E_B of the i^{th} site of the lattice as

$$E_B(i) = E_B^E + E_{EL}(i) \tag{4.1}$$

with the elastic energy cost being,

$$E_{EL}(i) = \kappa \sum_j (1 - q_i' q_j) \tag{4.2}$$

where the variable $q_i = \pm 1$ indicates the current state of the i^{th}cell (say, MI = 1 and CM = -1), q_i' is the proposed new state for the i^{th} cell (i.e. $q_i' = -q_i$), the index j of the sum runs over the number of nearest neighbors Q, and κ is an elastic constant.

Thus, if initially the i^{th} cell is in the same state as all of its neighbors, then the barrier to overcome is (maximally) increased from the electronic value E_B^E by the amount of $E_{EL} = 2\kappa Q$ corresponding to the maximal mismatch. If, on the contrary, the i^{th} cell is initially in a different state with respect to all of its neighbors, the barrier to overcome is solely the electronic one, as $E_{EL} = 0$ since all cells would end up in the same phase. For simplicity, we shall consider here that the range of the elastic term is only to the nearest neighbors, so in the present 2D lattice $Q = 4$. There is of course freedom to choose longer range interactions. We shall come back to this point later on.

As we shall see, the low-resistance states may become long-lived as the filamentary structures grow thick. Thus, for the sake of clarity in the presentation of our results, we shall first dedicate the next section to describe the formation of CM filamentary structures and how their thickness may grow under strong applied voltages. Then, in the following section we shall describe how the relaxation time may be significantly affected by the inclusion of the elastic deformation term and how it may qualitatively account for the various EMT regimes discussed before. We finally also compare our model behavior and experiments involving the application of trains of short voltage pulses, which bring us qualitatively closer to the realm of spiking neurons.

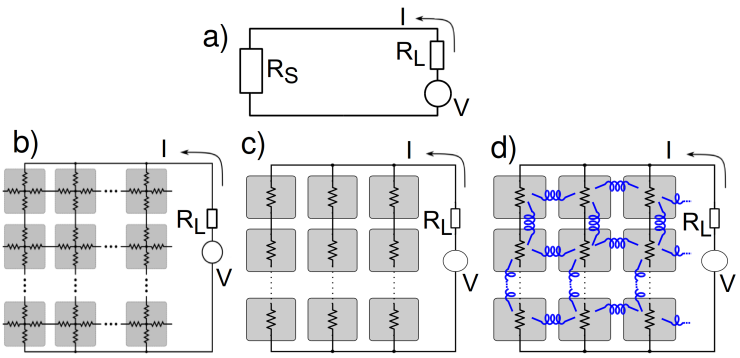

Figure 4.2: a) Circuit diagram of the system. b) Diagram of the 2D resistive network of the model from Ref.[42]. c) Diagram of the 1D filament approximation. All transverse currents have been neglected. d) Diagram of the 1D approximation with local elastic interactions (represented by the blue springs).

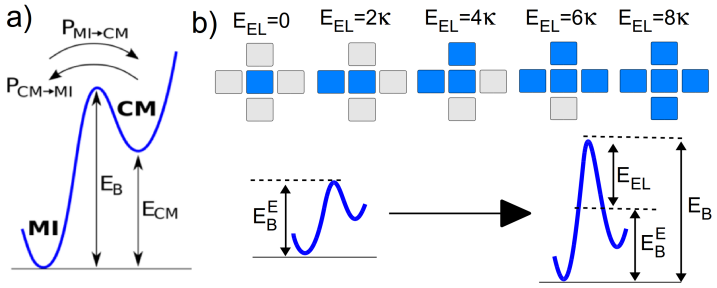

Figure 4.3: a) Energy landscape of the model. The Mott-insulator (MI) and the correlated-metal states (CM) are separated by the energy barrier E_B. b) The height of the barrier is affected by local structural distortions according to the elastic energy cost of Eq.4.2. We show the different possible configurations for a first neighbor interaction with their respective energy values.

4.3 Filament formation and growth

The EMT proceeds through two distinct stages: the first is the creation of low resistance filamentary structures that inter-connect the electrodes; the second is the successive reabsorption of the filaments as the system recovers the high resistance state. The first one occurs under the application of a strong external voltage, while the second takes place when the applied voltage is switched off. The present section is devoted to describing the first process.

The formation of the filaments under the application of an external voltage in the present model was already qualitative described in Ref.[42]. The main features were the existence of a threshold field for the formation of filaments and that the number of filaments (or the fraction of phase change in the system) grows with the magnitude of the applied field via a process of subsequent multiple filaments formation. The inclusion of the elastic term does not change the main

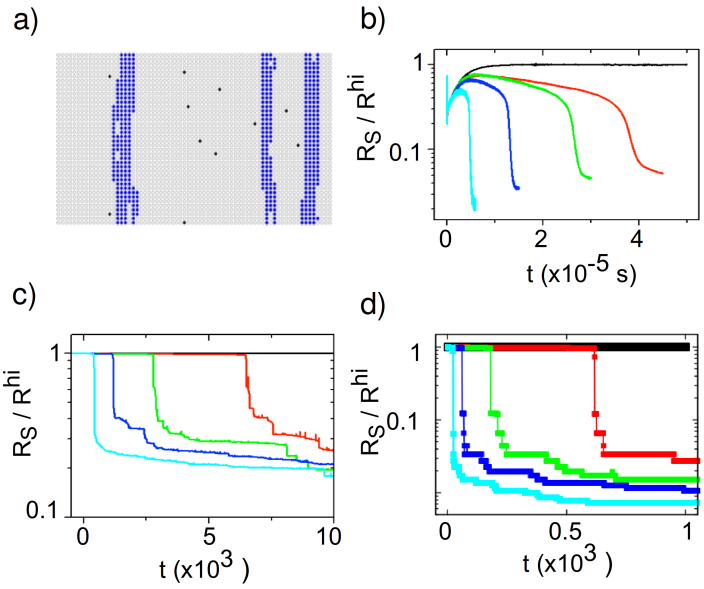

Figure 4.4: a) Snapshot of the simulated 2D resistive network after EMT, adapted from Ref.[42]. The black and blue dots indicate the sites that are in the CM state, while the gray dots correspond to the sites in the MI state. The dots forming filaments are coloured for easier visualization. The formed filaments exhibit a rather homogeneous thickness as explained in the text. Obs: A different colour-code will be used in the work for the 1D model simulations to avoid confusions. b) Experimental RS curves for different applied voltages in a $GaTa_4Se_8$ device. The curves correspond to voltage values of (from right to left): 6, 40, 44, 56 and 86 V. The length of pulses was limited to 50, 45, 30, 15 and 6 μs. The experiments were performed at a temperature of $T = 77K$. The curves show an initial transient increase due capacitive effects. c) Numerical simulations from the original 2D model adapted from Ref.[70]. The simulations were performed for a 128x40 network (NxW) with $E_B^E = 20$, $E_{CM} = 10$, $E_{MI} = 0$, $R_L = 0.1443$, $R_{CM} = 0.3R_L$ and $R_{MI} = 16.41R_L$. The curves correspond to V values of 400, 600, 650, 700 and 750. d) Numerical Simulations from the 1D filament approximation. The simulations were performed on a 50x140 network with $R_L = 500$, $R_{CM} = 200$ $(0.4R_L)$, $R_{MI} = 200$x10^3 $(400R_L)$, $E_B^E = 11$, $E_{CM} = 5$ and $\kappa = 1$. The curves correspond to V values of 300, 450, 500, 550 and 600. The same parameters will be used for all simulations in the work, except when specifically indicated. The units of time for simulations are expressed in simulation steps and the voltages are expressed in arbitrary units. The same units are used for all the simulations presented in the work.

basic mechanism, however, there are a few qualitative differences that we shall explore in this section.

In Fig. 4.6 we show the dependence of the delay time for filament formation

t_D with the applied voltage on the system (V_S), both for experimental data in a $GaMo_4S_8$ and for numerical simulations. We observe that the model behaves qualitatively similar as the experimental system, with a variation of t_D spanning many orders of magnitude. Both data sets show a linear behavior in a semi-log plot for short times and large V_S, and a clear slowing down of the dynamics as V_S approaches the V_{th}. At the threshold voltage the delay time should diverges, however it is difficult to access that regime both, experimentally and numerically.

We shall now consider in detail the formation of the filament from a dynamical point of view. This will allow us to derive approximate expressions for the delay time t_D.

The formation of filaments is a sudden event, thus the state of the system *previous* to the EMT breakdown still has the vast majority of cells in the initial MI state. Thus the system before the rupture is quite homogeneously MI. This implies that the role of the elastic term before the rupture is essentially to renormalize the value of the electronic barrier height E_B^E to $E_B \approx E_B^E + 2\kappa Q$ for the MI sites, which upon transition to the CM state find themselves surrounded by neighboring MI site. In contrast, any site that has already become CM, under relaxation to the MI does not see any elastic barrier, since all his neighbors are MI. Then this allow us to understand that the elastic term just produces slight changes in the value of the threshold voltage V_{th} and the time t_D [42].

One may gain analytic insight in the process of the initial filament formation and threshold behavior by considering the dynamical behavior given by the deterministic partial differential equation that follows from the probability rates of our model in a continuum limit. The production rate of CM-cells is given by the difference between a gain and a loss (leaky) term with their respective probabilities.

$$\begin{aligned} \frac{dn_{CM}}{dt} &= [n_{MI}P_{MI\to CM}] - [n_{CM}P_{CM\to MI}] \\ &\approx n_{MI}e^{-(E_B^E+E_{EL}^{MI}-V'(n_{CM}))} - n_{CM}e^{-(E_B^E+E_{EL}^{CM}-E_{CM})} \end{aligned} \tag{4.3}$$

where n_{CM} and n_{MI} are the time dependent number of cells in the CM and MI state, respectively. N is the number of cells between the top and bottom electrodes, i.e. the linear longitudinal dimension of the system. The elastic energy term in the model depend on the specific local configuration, so for the present analysis we have approximated them by the parameters E_{EL}^{CM} and E_{EL}^{MI}, which would correspond to average elastic energies of a CM and a MI cell, respectively. The voltage $V'(n_{CM})$ is the voltage drop on the MI cells, $V' \approx V/(N - n_{CM})$. Since $R_{MI} >> R_{CM}$, the total applied voltage V essentially falls on the high

resistivity cells MI, with $n_{MI} = N - n_{CM}$. Hence, the gain transition rate increases exponentially with increasing n_{CM}.

The reader that is not interested in the details of the dynamical analysis of the rate equation that provides approximation for the delay time t_D (shown in Fig. 4.6) may skip to the end of Eq. 4.8.

The rate equation has a stationary solution when $dn_{CM}/dt = 0$. It is given by the balance between the gain and the loss term. We shall consider the existence of such a solution as a function of the external voltage V. A geometric solution of the problem is shown in Fig.4.5 where we plot the gain and loss terms as a function of the variable n_{CM} at increasing values of V and all other parameter left fixed. The way to interpret this plot is as follows: at any given value of n_{CM} either the gain (red) or the loss (blue) rate is bigger. If the gain is bigger, then n_{CM} will evolve to the right, that is, to higher values. If the loss is bigger, it evolves to the left. The equilibrium of n_{CM} is where the gain and loss transition rates are equal. We observe in the two top panels of the figure that there are two points where the gain and loss terms cross. However, it is not difficult to see that only the lowest one (black dot) corresponds to a stationary *stable* equilibrium state, while the higher one (empty dot) is an *unstable* equilibrium point. Varying the parameter V, there is a critical value where the two crossing points "collide" at n^*_{CM}. The interpretation of this critical V is the finite threshold value V_{th}. For higher values of $V > V_{th}$, as shown in the last panel, there is no stationary state for n_{CM}, which means that the gain rate is never compensated by the loss rate and there is a runaway evolution of n_{CM} (indicated by the arrows). This Instability signals the formation of the first filament.

This process is not an uncommon situation found in dynamical analysis and is termed a saddle-node bifurcation [73]. For further details, an analysis of the numerical integration of the rate equation is shown in the Supplementary Material. We shall now derive two approximate expressions for the delay time t_D. One is simpler and valid at shorter times and higher applied V and the other is for longer times and V closer to V_{th}.

If the parameters of the model are such that $n^*_{CM} << N$, then one may approximate the rate equation 4.3 by

$$\frac{dn_{CM}}{dt} \approx Ne^{-(E_B^E + E_{EL}^{MI} - V/N)} - n_{CM}e^{-(E_B^E + E_{EL}^{CM} - E_{CM})} \tag{4.4}$$

If $V > V_{th}$ then an avalanche event will occur, as described above. Before the avalanche can take place there is a period where the evolution of the system (i.e. of $n_{CM}(t)$) is dominated by the slow dynamics at the proximities of the former stationary point where $n_{CM}(t) \approx n^*_{CM}$. It is the region where the gain and lose rate curves are approximate parallel (red and blue curves in Fig. 4.5).

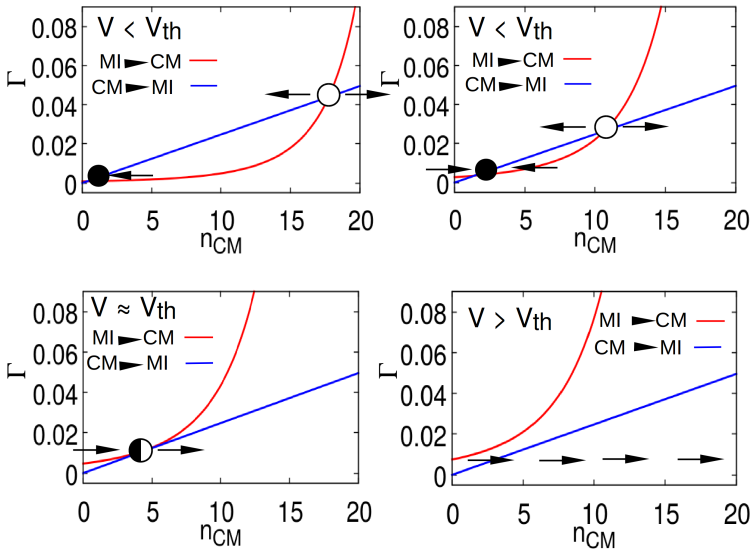

Figure 4.5: Dynamical analysis of the model. EMT rates (Γ) according to Eq.4.3 as a function of n_{CM}. The red curves correspond to the gain rate (first term of Eq.4.3) and the blue curves correspond to the lose or "leaky" rate (second term of Eq.4.3). We show the results for four different applied voltages (increasing from letft-to right and from top-to-bottom panels). For $V < V_{th}$ (top panels) the system exhibits two equilibrium points (where the two curves cross each other). At $V = V_{th}$ (bottom-left) the two equilibrium points "collide" at n^*_{CM}, while for $V > V_{th}$ (bottom-right) no crossing points are present and no equilibrium can be achieved. The black dots indicate the stable ("attractor") solution, the empty dots the unstable ("repeller") solution and the half-filled indicate the collapse of both solutions. In the last panel the arrows indicate the divergent dynamic. This evolution is known as a "saddle-node bifurcation" [73].

Once the evolution of n_{CM} overcomes this regime, it rapidly increases to N, i.e. the filament forms with an avalanche. Thus, we may neglect the duration of the sudden event for the estimation of the delay time for the filamentary formation and obtain an approximate expression by integration of Eq. 4.4 from 0 to n^*_{CM},

$$t_D(V) = \frac{1}{B} ln(\frac{A(V)}{A(V) - n^*_{CM} B}) \tag{4.5}$$

where $A(V)$ is the first term in the right hand side of Eq.4.4, B is the exponential factor in the second term of the same equation and n^*_{CM} was assumed a constant.

We used the expression above to produce fits of the experimental and numerical data at short times. This is shown in blue curves in Fig. 4.6, where we observe that the approximate expression can reproduce the variation in t_D of more than two orders of magnitude. The fitting parameters are summarized in the Table 4.1.

At lower V, and as we get closer to the threshold, the approximation made

before is expected to fail, as mentioned before. To describe the region close to the threshold we need to more accurately describe Eq.4.3 expanding around the bifurcation point (n^*_{CM},V_{th}). Thus, defining $dn_{CM}/dt \equiv f(n_{CM}, V)$, and using that at the bifurcation point $f(n^*_{CM}, V_{th}) = 0$ and $\frac{\partial f}{\partial n_{CM}}(n^*_{CM}, V_{th}) = 0$, we get to the lowest order

$$\begin{aligned}\frac{dn_{CM}}{dt} \approx & \bar{A}(n_{CM} - n^*_{CM})^2 + \\ & + \bar{B}(V - V_{th})(n_{CM} - n^*_{CM}) + \\ & + \bar{C}(V - V_{th})\end{aligned} \tag{4.6}$$

where

$$\begin{aligned}\bar{A} &= \frac{\partial^2 f}{2\partial n^2_{CM}} = \frac{V^2_{th} e^{-(E^E_B + E^{MI}_{EL} - \frac{V_{th}}{N - n^*_{CM}})}}{2(N - n^*_{CM})^3} \\ \bar{B} &= \frac{\partial^2 f}{\partial V \partial n_{CM}} = \frac{V_{th} e^{-(E^E_B + E^{MI}_{EL} - \frac{V_{th}}{N - n^*_{CM}})}}{(N - n^*_{CM})^2} \\ \bar{C} &= \frac{\partial f}{\partial V} = e^{-(E^E_B + E^{MI}_{EL} - \frac{V_{th}}{N - n^*_{CM}})}\end{aligned} \tag{4.7}$$

where the derivatives are evaluated at (n^*_{CM},V_{th}). Integrating, we obtain for t_D

$$t_D = \frac{2atan(\frac{2\bar{A}(n_{CM} - n^*_{CM}) + \bar{B}(V - V_{th})}{\sqrt{4\bar{A}\bar{C}(V - V_{th}) - \bar{B}^2(V - V_{th})^2}})}{\sqrt{4\bar{A}\bar{C}(V - V_{th}) - \bar{B}^2(V - V_{th})^2}} \Big|^{n^*_{CM}}_{n_{CM}=0} \tag{4.8}$$

The fit according to Eq.4.8 is shown in solid green lines in Fig.4.6 for both, experimental and numerical data. We observe that the approximation captures the behavior of t_D near the thresholds. The fitting parameters are summarized in the Table 4.1.

We now turn to describe one of the new features introduced by the elastic term in our model, namely the thickening of the filament with time. The width of initial filament is is just one cell. Thus, after it forms the resistance of the system R_S drops from a high value $R^{hi}_S \approx R_{MI}N/W$ to a lower value $R^{lo}_S \approx [R^{hi}_S // R_{CM}N]$, where W is the width of the resistor network and N is the length (i.e. distance between electrodes) as before. The decrease of R_S provokes a reduction of the voltage applied on the network according to $V_S = \frac{R_S}{R_S + R_L} V$, where R_L is the load resistance. Hence, the new value of V_S may be larger or smaller than V_{th}. In the former case the system will undergo a second filamentary formation, again according to Eq.4.5 but for a new (lower) value of V_S. After the formation of the second filament, V_S will drop further, and the process of filament formation will continue until $V_S \approx V_{th}$. This feature was already present in the previous model

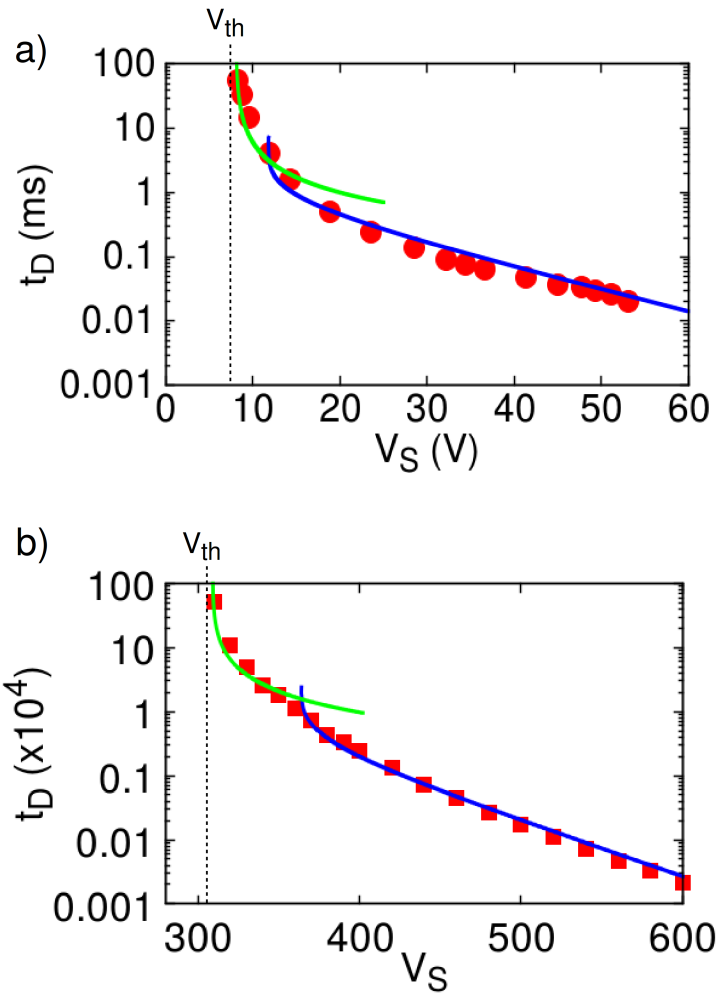

Figure 4.6: Commutation time t_D as a function of the applied voltage. In panel (a) we show experimental results on a $GaMo_4S_8$ sample and in panel (b) we show our model simulations. For each case we present two different fits: one for voltages close to V_{th} according to Eq.4.8 (solid green line) and another fit for the rest of the curve according to Eq.4.5 (solid blue line). The fitting parameters are shown in Table 4.1.

without elastic term. Thus, in that case, the position where the filaments form was essentially random and did not have any spatial correlation.

In contrast, in the present model the elastic energy term favors the growth of adjacent filaments, or, in other words, it favors the thickening of the filaments. This is easy to see, since an isolated filament requires the phase change of cells into the CM-state, while being surrounded by the other MI phase. That implies a maximal local elastic cost (see above). However, if a filament is already in place, the phase change of a cell adjacent to it is less penalized, hence has a higher probability to occur. This feature is seen in the panels of Fig.4.7.a, where we show snapshots of the system before the formation of the first filament ($t < t_D$), just after its formation ($t \approx t_D$) and at a later stage ($t \approx 5t_D$). We see that

	Experiments		Simulations	
	Region $V \approx V_{th}$	High Voltage Region	Region $V \approx V_{th}$	High Voltage Region
E_B^E	$110meV$	$100meV$	$70meV$	$70meV$
E_{CM}	$15meV$	$15meV$	$31.85meV$	$31.85meV$
E_{MI}	0	0	0	0
E_{EL}^{MI}	$10meV$	$10meV$	$49.7meV$	$47.8meV$
E_{EL}^{CM}	0	0	$12.7meV$	$12.7meV$
$\frac{n_{CM}^*}{N}$	0.08	0.05	0.07	0.04
N	2000	2000	50	50
T	74K	$74K$	$74K$	$74K$
V_{th}	8.0 V	-	$1.97V$	-
ν^{-1}	$1\mu s$	$1\mu s$	1	1

Table 4.1: Parameters used for the fits of Fig.4.6. For the fit of the simulation data we used as free parameters: V_{th}, E_{EL}^{MI}, E_{EL}^{CM} and n_{CM}^*. The others parameters are the same as in the numerical simulations. The energy and voltage values were converted from arbitrary units by assuming $T = 74K$. For the fit of the experimental data, all parameters are free, but we tried to obtain values physically reasonable. For instance, for the parameter N that corresponds to the number of cells, we implicitly assume a physical cell size Δx=d/N=$35\mu m/2000$=$17.5nm$ which is of the order of magnitude of the domains observed in STM (see Fig. 4.7).

both process have occurred, more filaments are present but also the filaments grew thicker. Evidently, the higher the value of the elastic constant κ and/or the longer the range of the elastic interaction, i.e. Q, the more favorable would be for the thickening process with respect to new individual filament formation. Results for two different $\kappa's$ are shown. In addition, the increase of κ may enhance the formation of CM-clusters before the generation of filaments, which, in turns, may affect the value of t_D. As seen in Fig.4.6, this last effect plays little role for $\kappa = 1$.

This feature may allow us to interpret the experimental results reported by scanning tunneling microscopy (STM) on a cleaved surface of a $GaTa_4Se_8$ compound [14] after the EMT. The image data in Fig.4.7.b show the variations in the conductance map due, presumably to the cross sections of the conductive filamentary structures that were created by the EMT (in red). The distribution of areas of these conductive cross sections, which we associate to the filament thickness in our model, are quantified in the histogram in Fig.4.7.c. We can compare these data to our model simulation results. In the three panels of Fig.4.7.d we show

the evolution of the histogram of filamentary thickness distribution during the application of a continued pulse voltage. We observe that, consistent with our previous discussion, the histogram distribution slowly drifts to higher thickness and is in qualitative agreement with the experimental data. We notice here that when typical thicknesses are greater than about $0.1W$ (W being the width of the sample) the nucleation of separated filaments has shown to be a relevant effect (i.e. the creation of big filaments via the percolation of smaller ones). In the STM image we observe cross sections with areas up to about $0.01A$ (being $A \approx$ 500x500 nm^2 the total area), suggesting that is effect is not relevant for the experiments analyzed in this work [1]. Thus, we will restrain our study to filaments thicknesses below $0.1W$.

The systematic thickness grow of filaments in our model is further characterized in Fig.4.8. We show a color map (panel a) of the largest thickness of the formed filament as a function of the duration of the applied pulse voltage (t_{ON}) and its magnitude (V). The two panels b and c respectively show cuts of the color map at fixed V and fixed t_{ON} The results are obtained as the mean over 100 realizations. The parameters used for the simulations are the same as in Fig.4.4.

4.4 Filament reabsorption: retentivity in the recovery phase

We now turn to a central part of this study, which is the relaxation of the low resistance state back into the Mott insulator state after the applied voltage pulse is terminated. The proper description of this process is crucial for the understanding of the recovery phase in neuromorphic applications of the EMT for neuron analogue electronic devices [53].

The previous modeling of the EMT, which did not include the elastic term, predicted that the conductive low resistance state always returns back to the high resistance state with an essential constant relaxation-time rate. The cells in the CM metastable state relax back to the MI with a single characteristic time and they do that randomly. So the filaments disintegrate randomly as well. We shall now study how the addition of the electro-elastic effect in the model modifies this feature.

In a low resistance state there are filamentary structures which are composed of a relatively high number of cells that switched into the metastable CM-state. These structures are induced by an external applied voltage. After the voltage application is terminated, the CM cells start to relax back to the high resistivity

[1] For a better comparison with simulations, in the histogram of Fig.4.7.c we consider cross sections up to a few tens of nm^2. The full distribution is shown in Supp. Mat.

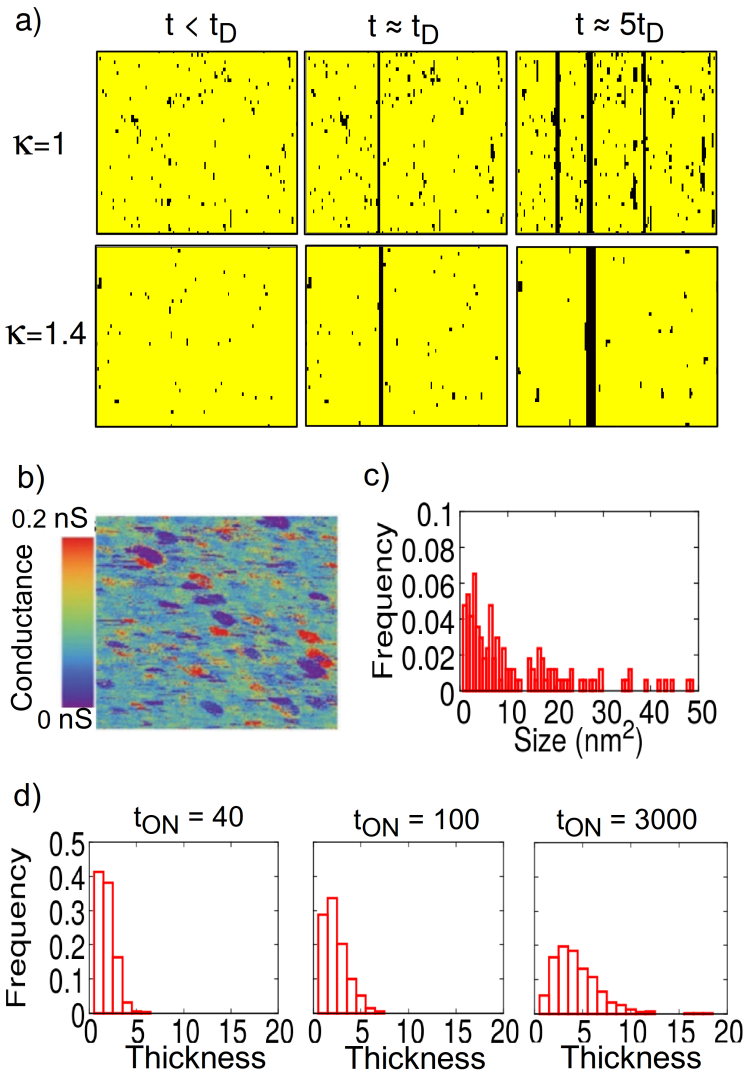

Figure 4.7: a) Snapshots of the resistive map during the application of an external voltage ($V = 600$). The black dots indicate the CM sites and the yellow ones the MI sites. We show the results for two different values of κ. The left panels show the system before the formation of the first filament ($t < t_D$). The central panels correspond to times shortly after the first filament formation. And the right panels show the system at times much longer than t_D. Higher κ favors the thickening process. b) Conductive STM image of a cleaved $GaTa_4Se_8$ surface after the EMT (from Ref.[14]). c) Distribution of cross sectional areas of conductive structures obtained from (b). d) Distribution of filamentary thickness from simulations. We show the distribution for three different pulse lengths (t_{ON}). An applied voltage of $V = 600$ was used for the three cases. The data corresponds to an average over 100 realizations.

MI-state. The relaxation time for the *total* number of cells to return to the MI-state is long. However, this is not the physically relevant time for the experiments. In fact, the experimental observation of the relaxation of the system is through

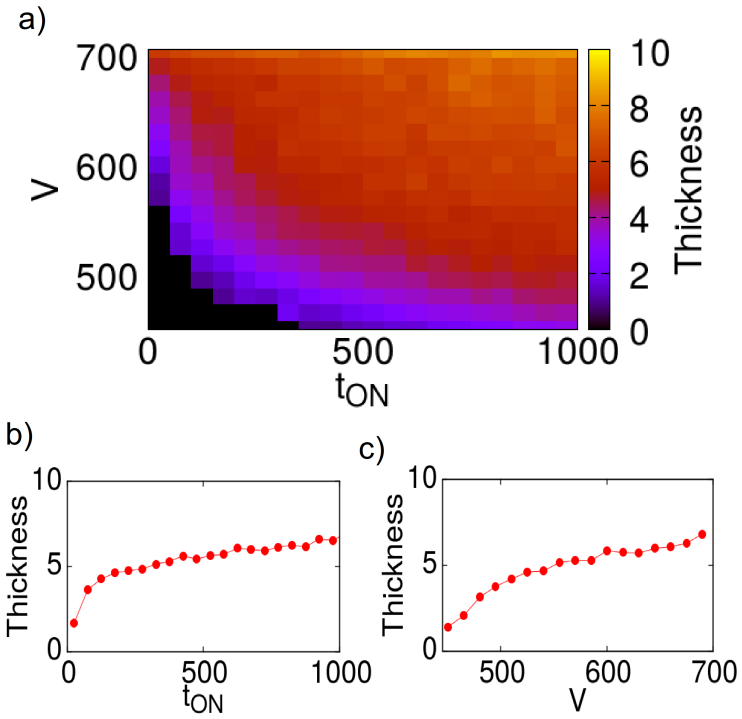

Figure 4.8: Filament Growth. a) Colormap of the filamentary thickness as a function of applied voltage and pulse length (t_{ON}). The results are obtained as the average over 100 realizations. The thickness is measured considering the thickest filament on each realization. The parameters used for the simulations are the same as in Fig.4.4. b-c) Vertical and horizontal cross sections of panel (a): maximum filamentary thickness as a function of pulse length (panel (b)) and applied voltage (panel (c)). The later was taken after a fixed $t_{ON} = 500$ and the former for fixed $V = 600$.

the behavior of the recovery of the resistance $R(t)$. So the important quantity to monitor in our model is when the filamentary structure of CM-cells breaks up or loses the percolation.

In our previous model, the cells forming the filament relaxed in a random fashion. In contrast, in the present case where we added the electro-elastic term in our model, we shall see that the filaments relax differently. Rather inversely to the case of filamentary growth by thickening, the dissolution of filaments occurs by thinning. In fact, as we shall see, the cells on the border of the filament have higher probability to relax to the MI-state compared to those in the interior of the filament.

In order to perform a systematic study of this process, we shall start from "artificially" well defined initial states consisting of homogeneous filaments of cells in the CM-state that we let relax back to the insulator. We shall consider initial filaments of different thickness and then record the time it takes for them

to break up. Since in our model this process is subject to statistical fluctuations we average our results over a large number of realizations (typically 100). We shall denote this time τ_R as it indicates the time that a filament keeps its high conductive state till it relax to the insulator one. This quantity may also be denoted *retentivity*.

In Fig.4.9 (left panel) we show results of our simulation studies for the dependence of τ_R with the initial filament thickness d, between $d = 1$ and $d = 10$. We observe that there are three different regimes. An initial exponential increase, which then becomes linear and finally saturates for higher values of d. Overall, τ_R increased by two orders of magnitude for filament thickness of just a few units. The fast initial increase, of a full order of magnitude when comparing $d = 1$ to 2, follows from the presence of the elastic term. This renders much less probable the relaxation of cells in any one of the two adjacent filaments with respect to a single one. In the former case, any cell of a filament is surrounded by 3 other cells of the same type, while in the later only by 2 (out of 4). This effect enters into an exponential in the probability (see Model section above). As $d > 2$ one may distinguish between central filaments or border filament. Cells belonging to central filaments have all their 4 neighbors in the same state. Hence the eventual elastic mismatch maximally penalize the relaxation. In contrast, cells in the external boundary of the filament only have 3 neighbors in the same sate. Hence boundary cells will relax faster. An internal cell would only get a good probability to relax by becoming part of the boundary, i.e. after outermost neighboring cells relax. This feature leads to a continuous "thinning" effect of the filaments, and it progresses at an approximate constant rate, which results in the observed linear dependence with d. At higher values of d a saturation effect becomes evident, as the thinning time starts to compete with the probability for relaxation of internal filament cells (i.e. with those inside an homogeneous CM phase).

We may easily estimate the relaxation time of a unitary filament from the loss term of the dynamical evolution of the cells of expression (4.3),

$$\frac{\partial n_{CM}}{\partial t} = -n_{CM} exp[-(E_B^E + E_{EL}^F - E_{CM})] \tag{4.9}$$

being E_{EL}^F the elastic part of the energy barrier of the i^{th}-cell in the filament, which is assumed constant for all the cells in the same unitary filament. The rupture condition for a unitary filament is given by the relaxation of a single cell (since we neglect transverse currents), i.e. $\Delta n_{CM} = 1$. A conductive individual filament has initially $n_{CM} = N$. Therefore,

$$\Delta n_{CM} = \Delta t N exp[-(E_B^E + E_{EL}^F - E_{CM})] = 1 \tag{4.10}$$

and we simply get:

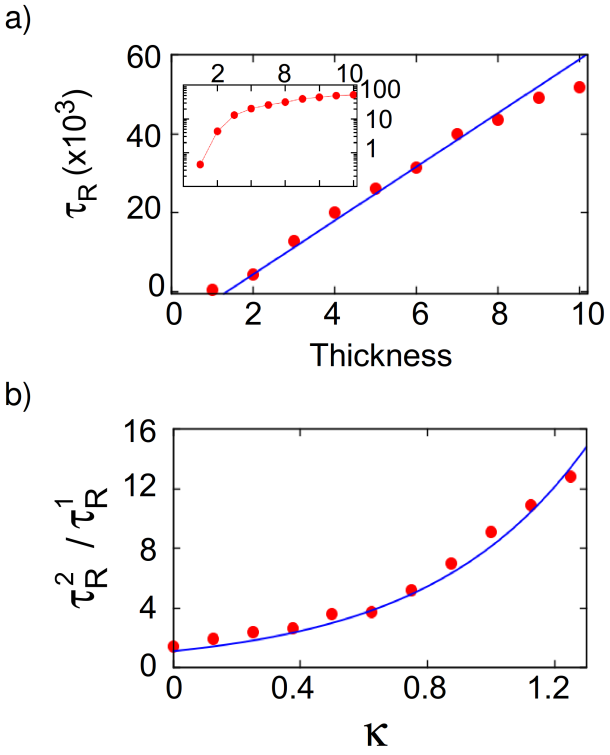

Figure 4.9: Top panel: Retentivity time as a function of filamentary thickness. The results are the average over 100 realizations. A fit according to Eq.4.15 (solid blue line) is shown. Inset: Semi-log scale version of main panel. A difference of about one order of magnitude can be seen between the first two points. Bottom panel: Retentivity ratio between filaments of thickness $d = 2$ and $d = 1$ (red squares) together with a fit according to Eq.4.13: $f(\kappa) = Aexp(2\kappa)$, with A the only fitting parameter. The fit corresponds to $A = 1.15$.

$$\tau_R^F = \frac{exp[(E_B^E + E_{EL}^F - E_{CM})]}{N} \tag{4.11}$$

where τ_R^F denotes the time for rupture of a unitary filament. From our previous qualitative discussion we get that $E_{EL}^F = 4\kappa$ for cells in an isolated filament of $d = 1$. Then $E_{EL}^F = 6\kappa$ for cells in the outer boundary of filaments of $d \geq 2$, and $E_{EL}^F = 8\kappa$ for cell in the interior of a thick filament ($d \geq 3$). The exponential dependence is explicit in Eq.4.11.

Then, recalling from our discussion that the filaments relax by progressive thinning, we may simply estimate the total time for the full rupture of a filament of thickness d as,

$$\tau_R \propto d\ \tau_R^F \tag{4.12}$$

where τ_R^F refers here to unitary border filaments. From the above equations we

may focus on the simple case with $d = 1$ and 2, which produce the largest relative retentivity gain. The ratio for the respective τ_R^d gives

$$\frac{\tau_R^2}{\tau_R^1} = exp(2\kappa(Q_2 - Q_1)) = exp(2\kappa(3-2)) \tag{4.13}$$

which corresponds to the blue solid line fit of Fig.4.9.b. Here Q_d correspond to the number of neighbours in the CM state for each thickness d. This expression highlights the exponential dependence on the elastic constant parameter κ. Evidently, in systems where the field induced dielectric breakdown is due to a structural change, one may consider that κ is very large and the change cannot be undone except by means of inducing a new structural change. We may then consider that τ_R becomes effectively divergent. Interestingly, this is the situation in non-volatile resistive switching oxides, such as TiO_2, HfO_2, NiO, CuO, etc, that form filamentary structures which involve ionic migration. One may also contemplate the possibility that in the Mott systems that presently concern us the regime (iii) where the resistive change may be non-volatile (or very long lived) may also involve a volume change of nano-domain size regions of the crystal. Then, the non-volatility may be due to pinning by strain defects induced by the strong electric field [14].

On the other hand, it is intuitive that the retentivity time may be significantly augmented by increasing the range of the elastic term. One may consider, for instance, next nearest neighbors or any longer finite range. Indeed, elastic strain involves several lattice units in real materials [74] . At the level of our model, we find this effect is so severe that, even upon increasing the range of the elastic term to the next nearest neighbors, our simulations become prohibitively slow. The mathematical analysis of the behavior and dependence of model parameters can be carried on along similar lines as we did above (see Sup. Mat.). Thus the origin of the long (and possibly infinite) retention times in regime (iii) may be due to long range strain induced by the filamentary growth.

4.5 Resistance relaxation with an applied voltage bias

We shall now discuss an interesting effect due to the introduction of the elastic energy barrier term in our model related to the electric stabilization of filaments. In other words, electrically prevent the filament break-up and reabsorption. In previous sections we have seen that a minimum threshold voltage V_{th} is necessary for filament formation. In this section we consider a different issue, namely, what is the minimal low-voltage that needs to be applied to sustain an already fully formed filament. The interest of this question is that it may be experimentally

tested as further validation of the present model.

In Fig.4.10 we show our simulation results for a resistive switching protocol where a small bias voltage ($V_{bias} < V_{th}$) remains applied during the relaxation process. Along with our numerical results we also show in the figure actual experimental data obtained in $GaMo_4S_8$ sample under a qualitatively similar voltage protocol. Specifically, the experiment was performed as follows: i) at $t = 0$ a bias voltage V_{bias} is turned on, ii) at $t = t_P$ a high voltage pulse V_P is applied for a time t_{ON}, iii) at $t_{OFF} = t_P + t_{ON}$ the applied voltage returns to V_{bias} and the evolution of the resistance of the system is observed. The bias voltage remains applied during the entire process. The times t_P and t_{ON} and the total applied voltage during the pulse $V_{bias} + V_P = constant > V_{th}$ are kept constant so that the switching voltage is the same in all realizations. In the figure we show the results of this protocol for three different V_{bias}. We observe that both, in experiments and simulations, the asymptotic relaxation value of the resistance depends on the applied V_{bias}. In fact, at the highest applied bias (red curve), we see that the resistance does not recover to the initial state but remains at a lower value. To get a better understanding of this behavior we show in Fig.4.10.c snapshots of the simulated resistive network for each V_{bias} at two different times: a short one, right after the pulse is terminated at $t = t_{OFF}$ and a longer when the asymptotic resistance state is reached [2]. We observe from the short-time snapshots (upper panels) that the $R_S^{hi} \to R_S^{lo}$ resistive change is rather independent of the applied (sub-threshold) bias-level, as a very similar multi-filament structures are realized in all three cases On the other hand, for the asymptotic state the system shows qualitatively different states. In the lowest bias case, the whole filamentary structure is reabsorbed. In the intermediate bias case only a single filament persists, which was the thickest. While in the higher bias case, all filaments formed during the pulse remain at asymptotic times. We also note that all isolated metallic regions (clusters) do relax to the insulator state in all three cases.The fluctuations observed for the intermediate voltage in panel (b) (blue curve) are due to rapid rupture and reconnection of small sections of a filament (i.e. a transitory decay to the insulating state). This effect may actually happen in real materials, however in our simulations it is likely overemphasized due to the finite size.

4.6 Complete pulse-voltage protocol

In this final section we shall consider the full-time behavior of the system, that is the whole process of formation and subsequent reabsorption of filaments. We shall

[2] As a technical side note we notice that we kept the same "seed" for the pseudo-random number generator in all three simulations for the sake of a more meaningful comparison.

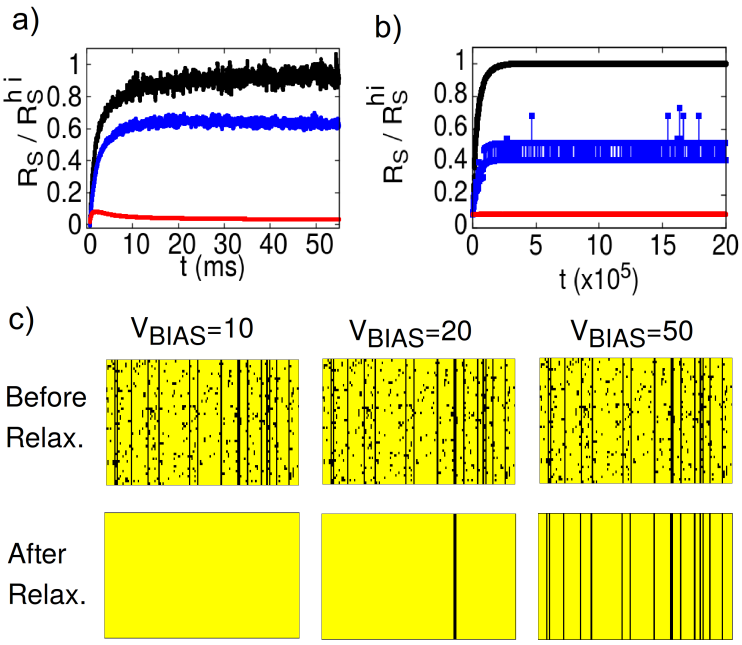

Figure 4.10: Relaxation of the sample resistance after EMT under different bias voltages. a)Experimental results on a $GaMo_4S_8$ sample for V_{bias}=2.4, 4.8 and 7.1V (top to bottom). b) Simulations results for V_{bias}=40, 50, and 70 (top to bottom). The time is measured from the beginning of the relaxation. For the detail description of the protocol see maintext. c) Snapshots of the resistive network before and after the relaxation process shown in panel (b).The snapshots correspond to the initial and final states of each curve in panel (b). We see that the state before the relaxation is essentially the same for the three curves. The final state, however, depends strongly on the applied V_{bias}. For the lowest bias all filaments are re-absorbed. For the intermediate bias only thicker filaments survive. And for the highest bias all filaments survive. The presence of V_{bias} stabilize (prevent relaxation) of the metallic filaments. Thicker (more stable) filaments require a lower external bias.The simulations correspond to a 50x140 network with $E_B^E = 15$, $E_{CM} = 5$, $R_L = 500$, $\kappa = 0.5$, $R_{MI} = 20000$, $R_{CM} = 200$, $t_P = 500$ and $t_{ON} = 120$. For a better visualization the ratio R_{MI}/R_{CM} was reduced with respect to previous sections. The EMT was generated with an external voltage pulse of $V_P = 750$ in simulations and $V_P = 37.5V$ in experiments.

adopt two different applied voltage protocols: a single pulse and a train of pulses. The former case is simplest to analyze as is closely related to the discussions of previous sections. In contrast, the interest of applying train of pulses [53] is that it bring us closer to the situation of actual neurons, which are excited by electric spikes.

In Fig.4.11 we show the full time evolution of the resistance during the application of a single pulse for both simulations and experiments on a $GaMo_4S_8$

sample (same sample as in Fig.4.6) . A single voltage is applied for a fixed duration t_{ON}, then V is set to zero. We show data for two different applied voltages. We observe the significant dependence of the retention time with the applied voltage. We see that a relatively small change in the strength of the applied pulse produces a great change of the retention time. For example, in experiments a change in the voltage from $34V$ to $56V$ produces a change in the retention time of a full order of magnitude (from approximately $2\text{x}10^{-3}$ to approximately $2\text{x}10^{-2}$). Similarly in the simulations, a change in the voltage from 450 to 600, produces a change of the retention time by a factor of 500% (from approximately $2\text{x}10^{4}$ to approximately 10^5).

These results permit to rationalize the existence of the regimes (ii) and (iii) that we described in the introductory section before. In Fig.4.12 we show our simulation results for the retention time τ_R as a function of parameters of a single voltage pulse: intensity V and duration time t_{ON}. In the color plot of panel (a) we observe that the retention of the filaments may be increased by either incrementing V or t_{ON}. The key point being that any one of these two parameters contribute to thicken the filaments. The dependence of the threshold with the duration of the applied pulse can also be clearly observed. This is basically the effect of the delay time that was discussed in previous sections: At a given applied voltage there is a delay time for the transition, which implies that the pulse duration must be above the delay time to actually produce the filament formation. The two panels (b) and (c) show two cuts of the color map for fixed t_{ON} and V respectively. All these results correspond to the mean over 100 realizations. Finally in panel (d) we show the evolution of τ_R on a $GaMo_4S_8$ sample as a function of the applied voltage for fixed $t_{ON} = 100\mu s$.

We may finally illustrate the behavior of the model upon the application of a train of voltage pulses. We show in Fig.4.13 the comparison of our model simulations with actual experimental data of the resistive change in a crystal of GaV_4S_8 upon application of voltage pulses. Two types of pulse protocol are applied: either a single pulse or a train of identical pulses with a relatively long separation, which mimics a train of spikes that may be arriving to the dendrites of a neuron [53]. In actual situations the arrival of pulses is mostly random, though here we focus on regular trains for the sake of simplicity. In the top panels of the figure we show the experimental data and in the bottom the simulations. Each pulse of the train is identical to the single one. The data in red color corresponds to the applied voltage and the data in blue to the respective resistance value $R(t)$. The small subpanels at the right of the main $R(t)$ panels indicate the asymptotic value of the resistance after the voltage pulse protocol is terminated. In the experimental data we observe that the single pulse is sufficient to produce a resistive change, which takes place after about $20\mu sec$. However, this low-

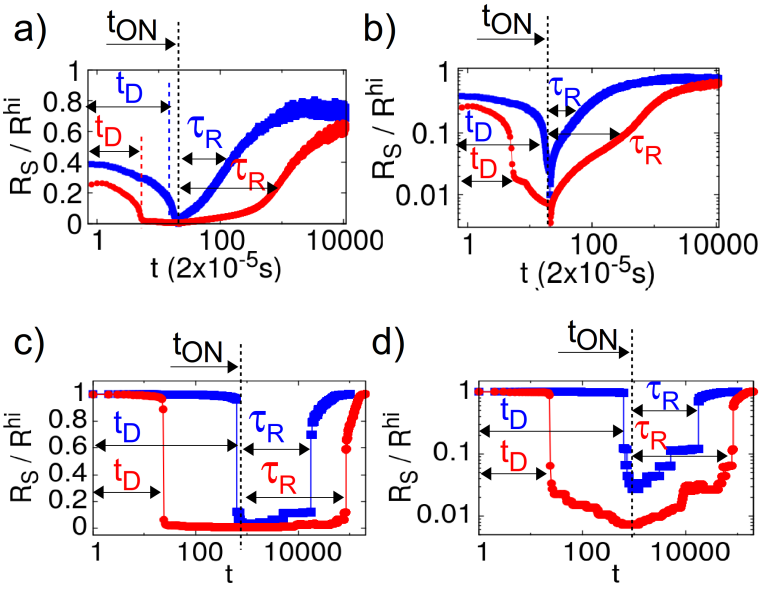

Figure 4.11: Evolution of the resistance during a complete Switching process. Panels (a-b) show experimental results on a $GaMo_4S_8$ sample while panels (c-d) show the results of our simulations in semi-log and log-log scale respectively. In each case an external voltage is appplied for a time t_{ON} after which the system is left to relax freely. The red and blue curves represent the results for two different applied voltages. The experimental curves correspond to $t_{ON} = 100\mu s$, $V = 34V$ (blue curve) and $V = 56V$ (red curve). The simulations correspond to $t_{ON} = 1000$, $V = 450$ (blue) and $V = 600$ (red). The characteristic times t_D and τ_R are indicated for each case. We notice that in the experimental data the initial value of R_S/R^{hi} is smaller than unity due to a capacitive transient introduced by the measurement circuit.

resistance state is volatile, as the corresponding asymptotic value has returned to the original high resistance value. In contrast, as the data of the right panel show, the application of 7 identical pulses was enough to dramatically increase the retention time. Thus, seven pulses are found to be sufficient to drive the resistance change non-volatile (in the time scale of the experiment).

In the bottom panels we see that the simulations capture qualitatively well these effects. From the discussions of previous sections we can understand the behavior. As shown in the left panels of the figure, a single pulse is enough to induce an EMT with filamentary formation. However, that single pulse only produced a thin filament with a short retention time, which got rapidly reabsorbed. Thus the system returned back to the initial high resistance state. In contrast, the train of multiple pulses produced the gradual thickening of the filament, with a consequent much longer retention time and persists beyond $t = 4000$.

This behavior may be considered an initial step towards the modeling of a

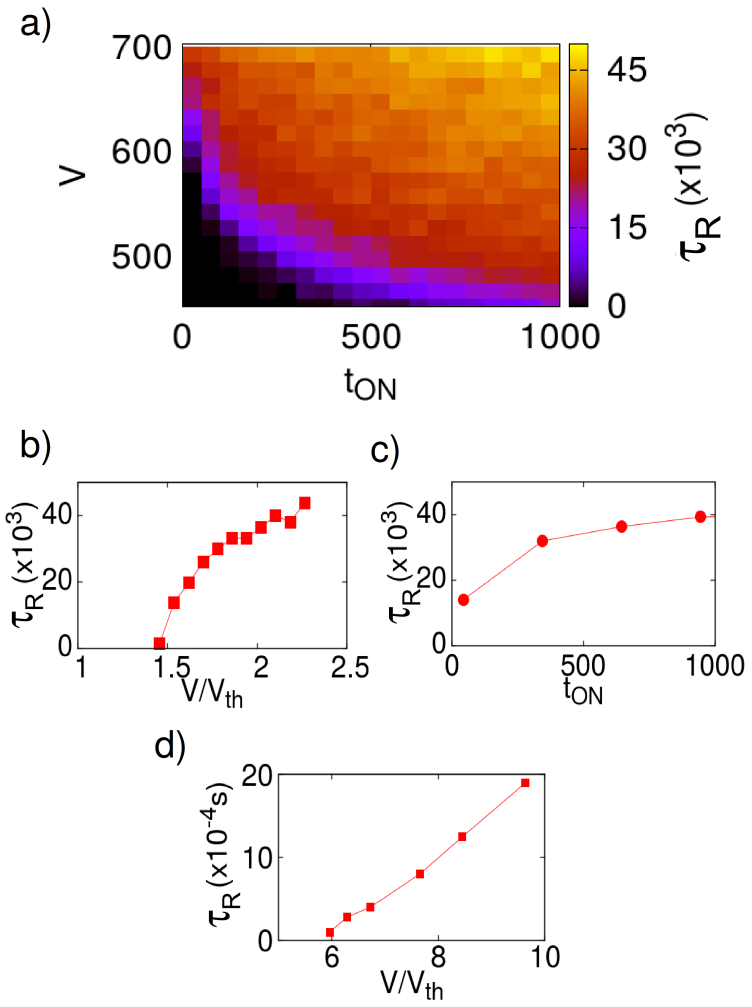

Figure 4.12: a) Colormap of the retentivity as a function of pulse length (t_{ON}) and applied voltage. b) Vertical cross section of panel (a): evolution of τ_R as a function of the applied voltage for fixed $t_{ON} = 500$. The voltage is measured in units of the threshold voltage with $V_{th} = 309$. c) Horizontal cross section of panel (a): evolution of τ_R as function of pulse length for fixed $V = 600$. The results are obtained as the average over 100 realizations. d) Experimental results: evolution of τ_R on a $GaMo_4S_8$ sample as a function of the applied voltage for fixed $t_{ON} = 100\mu s$.

recovery period of an artificial neuron under spiking stimulus. It may be interesting to mention that this variations in the recovery time may find potential useful applications in neural networks for tasks such as neural coding [75, 76].

We may note that the inter-pulse time duration (200μs in the experiment) provides a rough indication of the reabsorption time of the filaments. The systematic investigation of the retention time with the parameters of the applied voltage pulsing protocol is an important issue but it certainly involves some technical challenges and is outside the scope of the present study.

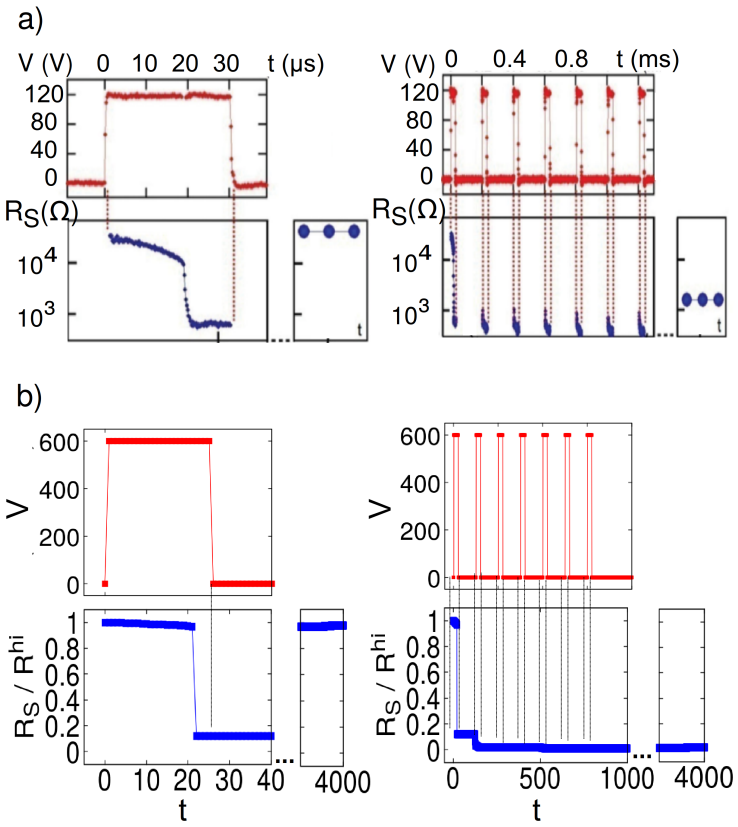

Figure 4.13: Retentivity manipulation in RS via a pulsed protocol. a) Experimental results in a GaV_4S_8 crystal for a single pulse of $t_{ON} = 30\mu s$ with $V = 120V$ (left), and for a train of 7 pulses of $t_{ON} = 30\mu s$ with $V = 120V$ separated by $200\mu s$ (right). b) Results from the simulations for a similar pulsed protocol. A single pulse of $t_{ON} = 25$ with $V = 600$ (left) and a train of 7 pulses of $t_{ON} = 25$ with $V = 600$ separated by 100 simulation steps (right) are shown.

4.7 Dynamical analysis and filament formation

In this section we complement the dynamical analysis of the model described before. We present a numerical integration of the model equations and analyze the origin of V_{th}. By definition, the threshold voltage is the minimum one at which at least one filament is formed. In our description each filament is independent from each other, so the analysis is done studying a single-filament dynamics. To begin we notice that in our model the change in the number of conductive cells at time t is given by the net rate equation of cell metalization:

$$\frac{\partial n_{CM}}{\partial t} = P_{MI\to CM} - P_{CM\to MI} = n_{MI}e^{-(E_B^E+E_{EL}^{MI}-q\Delta V)/kT} - n_{CM}e^{-(E_B^E+E_{EL}^{CM}-E_{CM})/kT} \tag{4.14}$$

where n_{CM} is the number of metallic sites in the filaments at time t and n_{MI} the number of MI sites (with $n_{CM} = N - n_{MI}$, being N the total number of sites

in a filament) and where we assumed that E_{EL} is at this point approximately the same for all sites in a given state (valid for $t < t_D$, as explain in previous sections). For simplicity we take $q = kT = 1$ and we will start assuming $E_{EL} = 0$. When the right-hand side of Eq.4.14 becomes zero then the rate of metalization is zero and the system is said to have a "fixed point", which represents an equilibrium state of the system. In precious sections, geometric solutions of this equation were shown for different applied voltages and the existence of a saddle-node bifurcation is shown [73]. Here we analyze the dynamics of the system via direct numerical integration. In Fig.4.14 the integration of Eq.4.14 with a 4th order Runge-Kutta method is presented. Here we assume that the voltage applied on the sample is independent of time (valid for $t < t_D$), and that the drop of voltage on each cell is given by $\Delta V \approx V/n_{MI}$. Each panel in Fig.4.14 correspond to a different applied voltage. And each curve inside a panel correspond to a different initial condition (different initial n_{CM}). Here we used that each filament has total length of $N = 50 sites$ and $n_{CM} = N - n_{MI}$. In this plot we can see the evolution of the two fixed points: the "attractor" (stable) point (represented with a filled circle) and the "repulsive" (unstable) point (represented by an empty circle). We can see again how the two points gets closer to each other as the voltage is increased, then collapse (at $V = V_{th}$) , and then no fixed points are present. The different initial conditions curves are meant to show the location and character of each fixed point: the system diverges from the "repulsive" point and converges toward the "attractor" point. The actual "physical" case would correspond to an initial n_{CM} close to zero, as the experimental devices begin in an insulating phase. For $Vs = 360$ ($V > V_{th}$) it can be seen that, before diverging, the system spends a significant amount of time at $n_{CM} \approx 5$ (close to location of the fixed point right before the bifurcation). This time-delay effect, known as the "ghost" of the fixed point, is a regular feature of saddle-node bifurcations and correspond to what we call t_D in previous sections.

4.8 Retentivity for clusters with $d > w_B$

In a filament of thickness greater than range of interaction (w_B) we can have two types of cells: the ones in the center and the ones in the "border". Each type will have a different energy E_{EL}. For simplicity we will consider here the case of a n.n. interaction (where $w_B = 2$). In this case the cells in the border have three CM neighbors and one MI from where $E_{EL} = 6K$. And the ones in the center have 4 CM neighbors from where $E_{EL} = 8K$. Using the EMT rate equation we can find the mean lifetime of each layer (central or superficial) $t^F_{ret-Center}$ and $t^F_{ret-Border}$. If $t^F_{ret-Center} >> t^F_{ret-Border}$ then the filament will tend to relax from outside-in (starting from the surface towards the bulk). After one

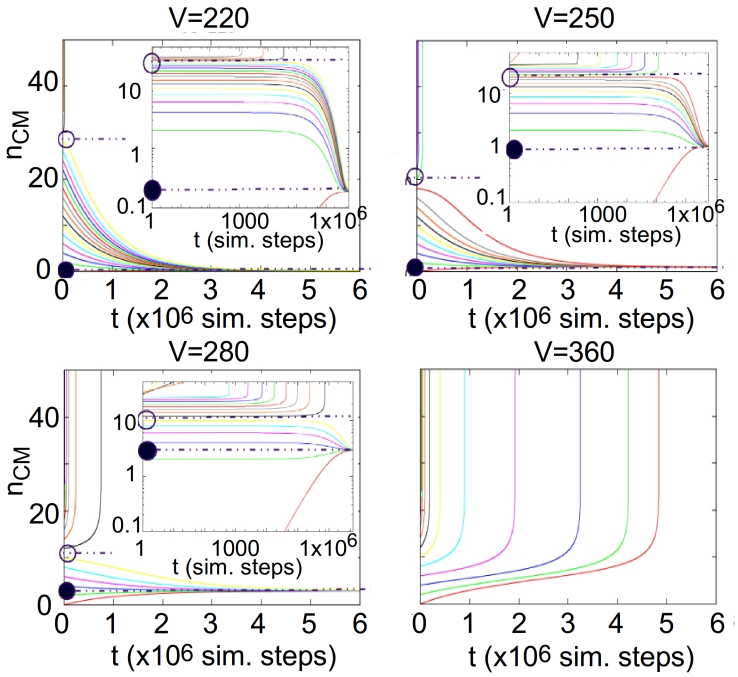

Figure 4.14: Dynamical analysis of the model. Numerical integration of Eq.4.14 via a $4th$ order Runge-Kutta method. It can be seen how the two fixed points (one attractor and one repulsor) gets closer as the voltage is increased until they collapse and disappear.This transition is known as a "Saddle-node bifurcation" [73]. The insets show the plots in a log scale.

cell in the surface turns MI then its nearest inner-neighbor becomes superficial, and after it relax the next neighbor becomes superficial and so on. Then the rupture of a filament of thickness d can be thought as the consecutive rupture of $d/2$ superficial cells (considering that the process begins at both boundaries of the filament with equal probability):

$$\tau_R = C \cdot \frac{(d-2)}{2} \cdot \tau^F_{R-Border} + \tau^F_{R-Border} \tag{4.15}$$

being τ_R the retentivity time of the filament and C a factor related with the geometry of the de-percolation path (i.e. shape and size of the outer-in perforation) In section 4.4 the evolution of τ_R as function of the thickness obtained from the simulations is shown, together with a fit according to Eq.4.15. For the fit we fixed $t^F_{ret-Border} = 4400$ (according to the retentivity obtained for $d = 2$) and used C as a free parameter, obtaining $C = 3.1$.

For a general w_B the description is completely analogous. In the next section we present the results for longer interactions, ranging from 2nd neighbors to 4th neighbors.

4.9 Longer range interactions

In this section we present simulations for longer interactions (beyond the n.n. used so far). In Fig.4.15 we show the results with interactions ranging from the 2nd to 4th layer of neighbors. In this case we can see that the evolution of τ_R as a function of the thickness exhibits first an exponential regime whose extension depends on the corresponding w_B. After this, the expected linear behavior can be seen as explained before. To keep the variation of the energy (and so τ_R) in the same range of magnitude for every interaction (due to computation times), we used a different surface constant (K) for each case. We used $K = 0.5$, $K = 0.33$ and $K = 0.2$ for the 2nd, 3rd and 4th neighbors interaction respectively.

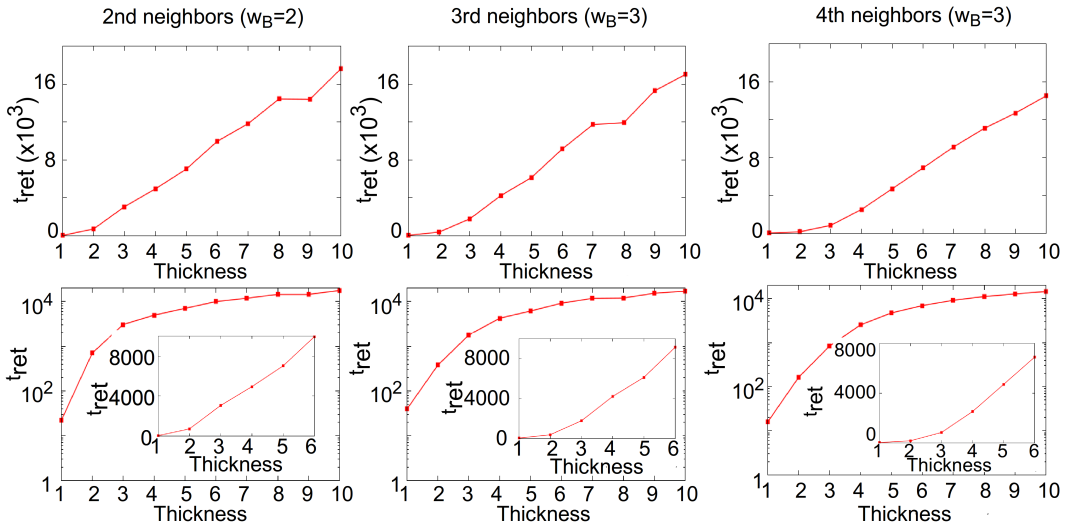

Figure 4.15: Simulations for different interaction lengths. We show the results for 2nd, 3rd and 4th neighbors interactions. The plots show the variation of the retentivity as a function of cluster diameter. The two regimes explained in the text can be observed for $d < w_B$ and $d > w_B$. The results are shown in linear (top) and semi-log (bottom) scale. The inset in the bottom panels show the linear plots in a limited range for a better view of the change of regime.

CR en Sistemas Fuertemente Correlacionados

En este capítulo se estudió el fenómeno de Conmutación Resistiva en sistemas con fuerte correlación electrónica. Se extendió un modelo previamente presentado, agregando interacciones locales. Se estudió la formación y crecimiento de filamentos metálicos en este modelo y se mostró que la inclusión de interacciones locales lleva a una dependencia exponencial entre el tamaño del filamento y su tiempo de relajación. El período de relajación de estos sistemas está asociado con el periodo refractario de una neurona artificial previamente presentada.

Chapter 5

VO_2 thermal spiking neuron

5.1 Introduction

In this chapter we will explore a new kind of neuronal-inspired device based in a prototypical strongly-correlated system such as VO_2. This material is known for experiencing a thermally driven insulator-to-metal first order transition close to room-temperature, when the kinetic energy starts dominating over the coulombic repulsion.

More important for our work, this system also exhibits a metal-insulator transition under the application of an external electric field. The origin of this transition is under debate. The central point of the discussion is if its origin is due to thermal effects or due to the destabilization of the electronic state generated by the external field or a combination of both [33, 34]. In this chapter we will first propose a phenomenological model to describe this transition. For simplicity our model will assume a purely thermal origin and we will see that it is able to reproduce some key features observed in experiments. One of the key features we will analyze are the oscillations observed in the resistance of the system under the application of a constant voltage [34]. We will see that these oscillatory dynamics can be associated with a very popular model of oscillating neurons known as the FitzHugh-Nagumo model (FNM). The FNM is one of the first models describing oscillatory neuron dynamics and has been extensively studied during the past decades. Oscillations in neurons (i.e. periodic spiking under a constant external stimulus) is a crucial element in biological systems and is believed to be behind the codification of information in the nervous system (i.e. neural coding) [77].

5.2 The model

To model the VO2 device we will use a 2D resistor-network with a parallel intrinsic capacitance. Each element of the network (with NxW sites) represents a small

(nanoscale) region of the physical system [42, 70]. The cells of the network are assumed to be large enough so that its electronic state is well defined. In the present model each cell site is assumed to be in one of two electronic states: correlated-insulator (MI) or correlated-metal (CM) with associated energies E_{MI} and E_{CM} respectively. These states are respectively associated with a high and a low resistance values,R_{MI} and R_{CM}. The resistor network model is schematically shown in Fig.5.1.a. To model the thermally driven 1st order transition we will make use of the local free energy f with a conventional Landau-type of expansion. From DMFT analysis, it is possible to see that for these systems, the free energy can be expanded as [78]:

$$f(\eta) = -h\eta + p\eta^2 + C_3\eta^4 \tag{5.1}$$

where $h = h_1(T - T_c)/T_c + h_2$, $p = p_1(T - T_c)/T_c + p_2$, T is the temperature, Tc is the critical point, η is the order parameter and all the rest are constants. In Fig.5.1.c) we show the energy landscape for different temperatures. The physical interpretation of the order parameter is not obvious and is related with the hybridization function in DMFT [78]. Nevertheless, the interpretation of the free energy is straightforward. For very low temperatures ($T << T_c$) the energy exhibits a single minimum, which we associate with the MI state. As T increases a second local minimum appears, which we associate with a metastable CM state. At $T = T_{MT}$ both states (MI and CM) becomes equally stable and for $T > T_{MT}$ the MI state loses stability. This is associated with the 1st order insulator-to-metal transition (referred to as IMT during this work or as MT after "Mott Transition").

To simulate the dynamic of the system we will follow the methodology of Ref. [42], explained in the following. Initially, all lattice cells are assumed in the MI state. In analogy to the actual experimental setup, we adopt an electric circuit with a *load* resistance R_L as shown in Fig.5.1.c. The external voltage can adopt any arbitrary profile $V(t)$, which upon discretization of the time becomes $V(t_i)$ at each time-step t_i. At every t_i the full resistor network circuit is solved, obtaining all the local voltage drops, resistance and temperature. The top and bottom electrodes are assumed perfectly metallic. The local temperature is updated using the heat equation through the discrete Laplacian approximation

$$\frac{\partial T(x,y)}{\partial t} c_h = p(x,y) - \kappa(5T(x,y) - \sum_{i}^{1stneighbors} T_i) \tag{5.2}$$

where c_h is the heat capacity of each cell, $p(x, y)$ the local dissipated power and κ the thermal conductance between neighboring sites (same for all the network). Each cell exchange heat with its 4 neighbors in the network and with the substrate at constant temperature T_B (where we assume a planar structure for the device).

The cells at the top, at the bottom and on the lateral borders exchange heat with the 3 neighbors and a virtual cell at constant temperature T_B. At each time-step the probability for a site to undergo a local Mott transition (MT), that is from MI to CM or the opposite, is given by $P_{MT} = \nu e^{-(\Delta E_S(T)/kT}$, where the constant ν is an attempt rate, k is the Boltzmann constant, T is the local temperature and where $\Delta E_S(T)$ is the energy barrier associated with the corresponding transition, with $S = MI, CM$. The energy barrier is defined by the local energy landscape which depends on the local temperature (see Fig.5.1). This probability is an Arrhenius like law, where the key feature is that the local temperature changes the probability for the MT of the cell.

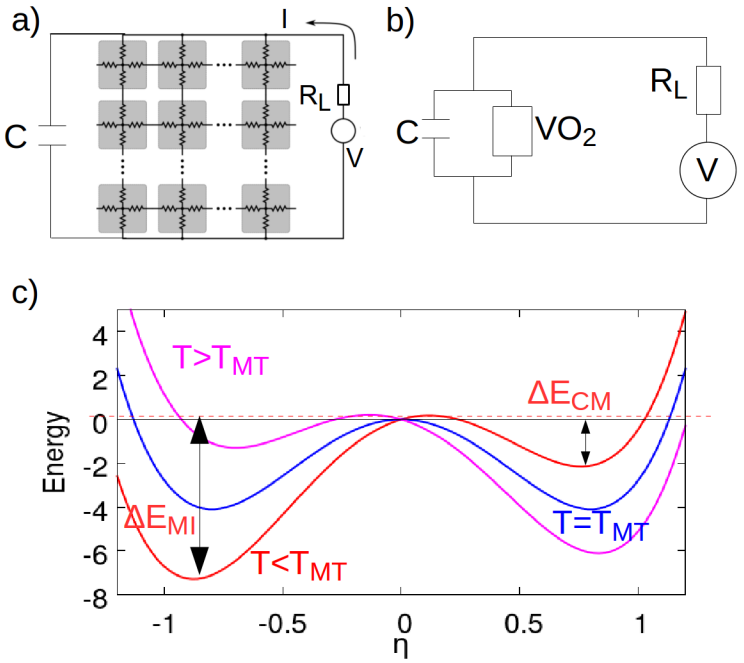

Figure 5.1: a-b) Circuit and network diagrams of the system. c) Energy landscape of the model for different temperatures according to Eq.5.1. For the present work we use: C_3=10.0; p_1=40.0; h_2=50.0; p_2=0; h_1=h_2/0.32; T_c=1.66; C=0.05; R_{MI} = 5000, R_{CM} = 500, N=50, W=100, c_h=300, κ=50, T_B=1. The insulator-to-metal transition temperature is indicated as T_{MT} in the figure.

At each time-step, the states of all cells are updated according to the above probabilities. This gives a new value of the system resistance, and the simulation proceeds. For simplicity, here we adopt $\nu = kT = 1$.

This simple model is able to reproduce the global resistance transition and some key features observed in VO_2 such as hysteresis behaviour (shown in Fig.5.2) and the S-shaped I-V curve with negative differential resistance.

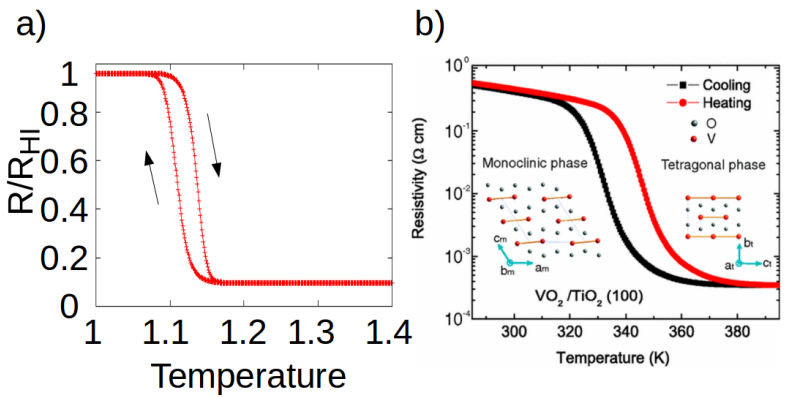

Figure 5.2: Hystersis in the R-T curve for simulations (left) and experiments (right) (adapted from Ref.[34]). In these simulations the temperature of the system (T) is gradually increased and is equal for all the sites in the network.

5.3 Oscillations and filament formation

Another key feature of VO_2 is its oscillatory dynamics. It is well known that regular periodic oscillations in the resistance are observed under a constant electric stimulus [34]. This feature is also captured by our simple model and shown in Fig.5.3. This is an important part of our work and will be analyzed with detail through this chapter. In Fig.5.3 we show the voltage drop across the device (V_D), its resistance (R_D), the fraction of metallic sites (n_{CM}) and the average temperature. And in Fig.5.4 we show snapshots of the resistive network at different instants of the oscillation. These snapshots provide some insight regarding the generation of the metallic structures that causes the abrupt collapse of the resistance. In Fig.5.4 we see that the switch of resistance begins with small accumulations of metallic sites that trigger the formation of metallic filaments. This can be understood as follows: the appearance of metallic clusters increases the flow of current through that path which in turns increase the local temperature. So the formation of the first metallic filament is driven by current-temperature feedback loop. After the first filaments is formed we see that they grow transversally via thermal diffusion and eventually all the sample becomes metallic. There is another important aspect about the IMT that we can see from Fig.5.3 and 5.4. It is easy to see that the transition involves two different time scales: one corresponding to the change in temperature and resistance (fast variables) and a second one (slow variable) corresponding to the charge and discharge of the capacitor (i.e. the change of V_D). A salient feature is that the characteristic time of the fast variables is much smaller than the one of the slow variable. The origin of these two time scales is easy to understand in our system. The fast variables are driven by the temperature-resistance feedback loop we have just described. On the other hand the slow variable correspond to the slow charge and discharge

of the capacitor. After the sample has become fully metallic, the voltage V_D goes down slowly which generates in turn a decrease in the temperature. When the IMT temperature is reached the system relaxes back to the insulating state and the entire process starts again. This kind of oscillatory systems with two time-scales are known as "relaxation oscillators" [73] and will be analyzed with more detail later in the work. We notice that the time-scale for the charge of the capacitor depends on the load resistance (R_L) and on the given capacitance of the device. Thus, the existence of the two time-scales is in principle restricted to the election of R_L. The dependence on R_L of the oscillatory regime has been previously analyzed in the literature [79, 80]

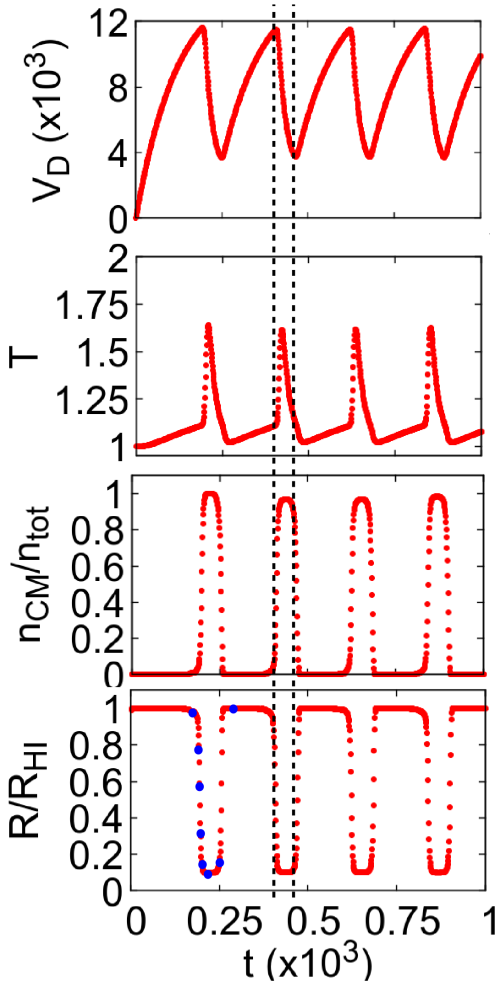

Figure 5.3: Oscillatory Dynamics. Evolution of the system under a constant external voltage $V = 30000$. We show the voltage drop across the device (V_D), the resistance (R_D), the fraction of metallic sites (n_{CM}/n_{tot}) and the average temperature T.

An interesting aspect of the simulated process described so far is that oscillations are predicted only for a restricted range of external voltages. In Fig.5.5 we show the evolution of V_D for different applied voltages. We see that for the lowest

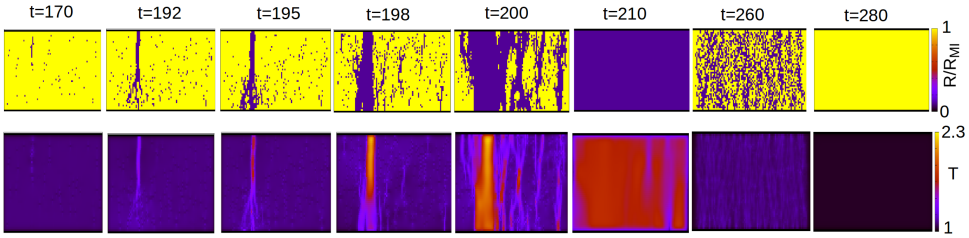

Figure 5.4: Snapshots of the resistor network and the temperature distribution during a complete oscillation (resistance collapse and recovery). The corresponding resistance values can be read from the bottom panel of Fig.5.3 indicated by blue circles.

voltage there is no resistance collapse, for intermediate voltages we have oscillations and for high voltages the oscillations are blocked and the system remains at a low resistance state. We also notice that between these three regimes there are two regions with transient oscillations. The dependence of the (stable) oscillations as a function of the applied voltage is shown in Fig.5.5 (bottom right). We see that the evolution of the frequency is not continuous and experiences a jump from zero to a finite value at a certain threshold voltage. In the next chapter we will extend the analysis of the oscillatory dynamics and we will establish a relation with the FitzHugh-Nagumo neuron model.

5.4 Dynamical analysis and the FitzHugh-Nagumo model

In this section we perform the dynamical analysis of the system. We start by writing down the model equations, for which we will perform first a dimensionality reduction. To describe our system we will focus on the three main variables studied in the previous chapter: the concentration of metallic sites n_{CM} (i.e. resistance), the temperature and the voltage drop over the device. From Fig.5.3 we see that the average temperature and the average concentration provides a good description of the dynamics of the system. Thus, for simplicity, we will adopt these average magnitudes to describe the system which we will see can reproduce the main features described in the previous section. The rate equations of these three main variables can be written as:

$$\begin{aligned}\frac{\partial n_{CM}}{\partial t} =&(N - n_{CM})exp(-\Delta E_{MI}(T)/kT) - \\ & n_{CM}exp(-\Delta E_{CM}(T)/kT)\end{aligned} \tag{5.3}$$

$$\frac{\partial T}{\partial t}c_h = \frac{V_D^2}{R_D} - \kappa(T - T_B)N \cdot W \tag{5.4}$$

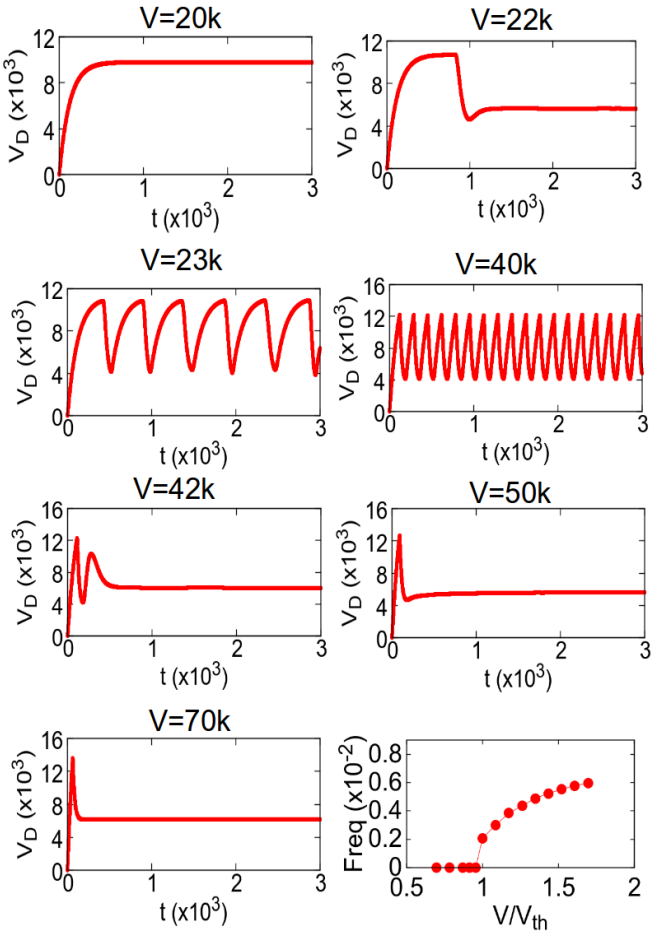

Figure 5.5: Evolution of the system for different applied voltages (in the magnitude of the voltages, "k" stands for "kilo", i.e. thousands). No oscillations are observed for low and high voltages. The evolution of the frequency is shown in the bottom-right panel.

$$\frac{\partial V_D}{\partial t} = \frac{1}{C}\left(\frac{R_D V}{R_L + V_D} - V_D\right)\left(R_D - \frac{R_D^2}{R_L + R_D}\right)^{-1} \tag{5.5}$$

with $R_D = (n_{CM}(t)R_{CM} + (N - n_{CM})R_{CM})/W$. Here we assumed that the system is made of W identical 1D filaments and that n_{CM} is the concentration of metallic cells in each filament. We will see that this rough approximation is enough for reproducing the main aspects of the transition, except of course the process of filament formation and growth described in the previous sections.

As described in the previous section, n_{CM} and T are fast variables with characteristic times much smaller than the slow variable V_D as described before. In Fig.5.6 we show the evolution of the system obtained from the numerical integration of the model equations with a 4th order Runge-Kutta method. We show the results for different applied voltages. The same global behaviour as before is obtained: oscillations are only observed for a restricted range of voltages with no oscillatory behaviour for low and high voltages. The threshold voltages for each

regime (oscillatory and non-oscillatory) are also very similar as the ones observed before. The frequency evolution is also shown.

To gain a better understanding of the process described so far we will proceed with a basic dynamical analysis of the model equations.

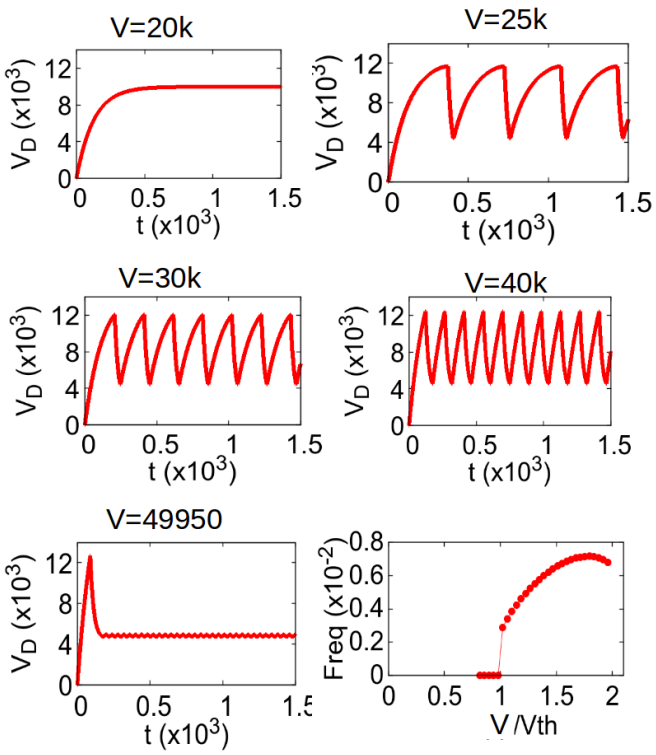

Figure 5.6: Evoltuion of the system under different applied voltages (k stands for thousands) obtained from the integration of the model equations (Eqs.5.3,5.4,5.5). Bottom right panel: frequency of oscillation as a function of the applied voltage.

To further simplify the analysis we will keep only one of the fast variables: we will assume that n_{CM} is an instant variable of the temperature which is given at any time by its equilibrium (Boltzmannian) concentration $n_{CM}(T) = Nexp(-\Delta E_{MI}(T)/kT)/(exp(-\Delta E_{MI}(T)/kT) + exp(-\Delta E_{CM}(T)/kT)$. So now the dynamic of the problem is reduced to a two dimensional coupled system on T and V_D. In Fig.5.7 we show the nullclines (i.e. equilibrium curves corresponding to $d\mathbf{x}/dt = 0$) for the two variables T and V_D. We show the results for three different applied voltages with their corresponding trajectories obtained from the integration of the model equations. The crossing points of these two nullclines correspond to the fixed points (equilibrium points) of the system. It can be seen that when the crossing point is located on the left and right arms of the N-shaped curve then the equilibrium points are stable (we show this later), while if is located on the middle arm it is unstable. We can see from Fig.5.7 that as the external voltage is increased then the crossing point moves from the left arm to the middle arm and finally to the right arm of the N-shaped curve. To obtain sta-

ble oscillatory solutions the fixed point needs to be unstable [49], i.e. the crossing point has to lie within the middle branch. For stable fixed points (i.e. on the left and right arms) the system converges towards the stationary stable point (where damped oscillations are feasible to occur). This explains that the oscillatory solutions are only observed for a limited range of voltages, corresponding to fixed points on the middle branch. As the fixed point transitions between branches it can be seen that the system goes through a Hopf-biffurcation, as we will see later.

When the crossing point is on the middle branch (oscillatory solution), we see from Fig.5.7 that the fast variable "jumps" between the left and right (stable) arms. This particular dynamic is typical of the so called "relaxation oscillators", which is relevant for the description of oscillating biological neurons. One of the first models describing this dynamic in real neurons is the well known FitzHugh-Nagumo model (FNM) [49]. The equations for the FNM are:

$$\begin{aligned} \frac{\partial u}{\partial t} &= f(u) - w + a \\ \frac{\partial w}{\partial t} &= bu - cw + d \end{aligned} \tag{5.6}$$

where f(u) is an N-shaped functions and a,b,c,d are constant. The variables u and w in the FNM correspond to the membrane voltage (fast variable) and to a "recovery" (slow) variable representing the (de)activation of ionic channels. The constant a (and/or d) correspond to the external current. In Fig.5.6 we show the nullclines for the FN model.

The FN model is known for reproducing some important aspects of biological neurons. Among these aspects are: discontinous frequency curves and excitation block (i.e. no oscillation for high external stimulus). Both aspects are also reproduced by our system as shown before. The disconitnuous frecuency is a key feature of certain type of neurons known as Type II neurons. Indeed, there is a standard classification of neurons between two groups (Type I and Type II) according to the response of their oscillation frequencies with the external stimulus. Type II exhibit a discontinous evolution with a non-zero frequency at the threshold stimulus, while type I exhibit a continous behaviour. Each type of neuron plays a crucial role in neural coding, i.e. in codifying information in the brain [77].

Another interesting aspect of the FNM is the presence of "subthreshold oscillations". When the system is excited with stimulus below the threshold for the resistance collapse, then small oscillations are observed which differ from the large trajectories described above. It is easy to see that this oscillations correspond to what is known as a Hopf-Bifurcation: in the limit between the middle and left branches of the N-shaped nullcline, the stationary point loses stability and a small limit cycle appears around this point. The presence of these oscil-

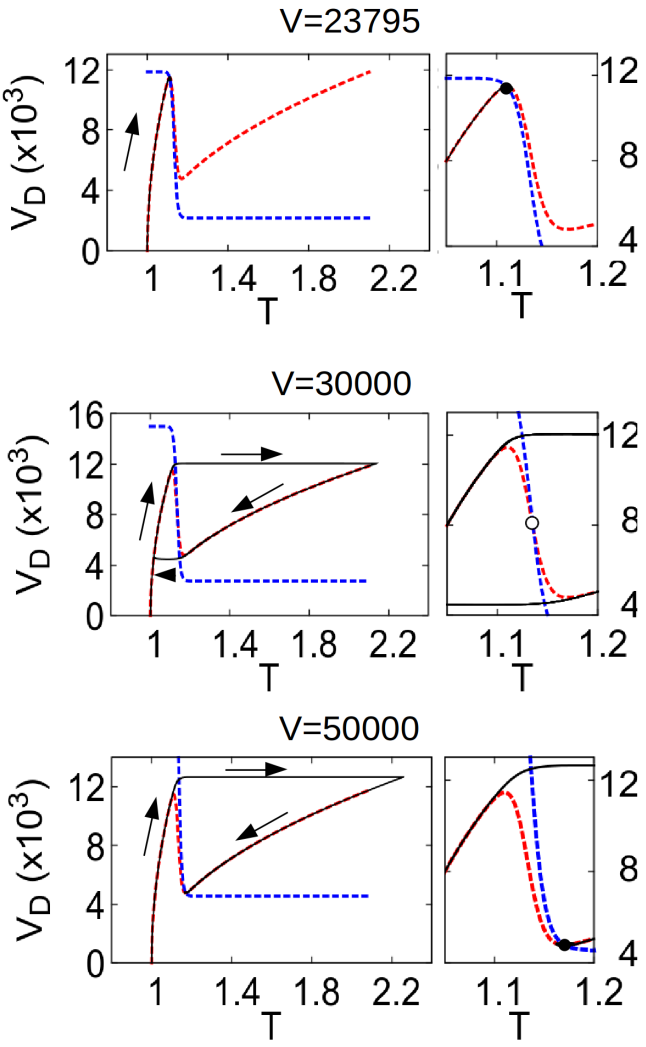

Figure 5.7: Left panels: nullclines of the reduced 2D system for three different voltages together with the corresponding trajectories obtained from the (3D) integration of the model equations. The red nullcline correspond to the fast variable T and the blue nullcline to the slow variable V_D. Right panels: detail of the nullclines around the fixed points (i.e. crossing of both nullclines). The fixed points are indicated with a black or white circle for the stable and unstable case respectively.

lations can be deduced from the linearized (2D) system around the stationary point (at V_D^o, T^o) in the critical region. If we call $\frac{\partial T}{\partial t} = F(T, V_D)$, $\frac{\partial V_D}{\partial t} = G(T, V_D)$ and $\boldsymbol{X} = (V_D - V_D^o, T - T^o)$, then the linearized system looks like

$$\frac{\partial \boldsymbol{X}}{\partial t} = \begin{bmatrix} F_T & F_{V_D} \\ G_T & G_{V_D} \end{bmatrix} \boldsymbol{X} = J \cdot \boldsymbol{X}$$

where $F_{(i)} = \frac{\partial F}{\partial i}$ (same for G) and J is the Jacobian matrix. A general solution for this system is $\boldsymbol{X}(t) = \boldsymbol{A} exp(\lambda t)$. Replacing in the previous equation leads to a standard eigenvalue problem. The real part of the resulting eigenvalues indicate

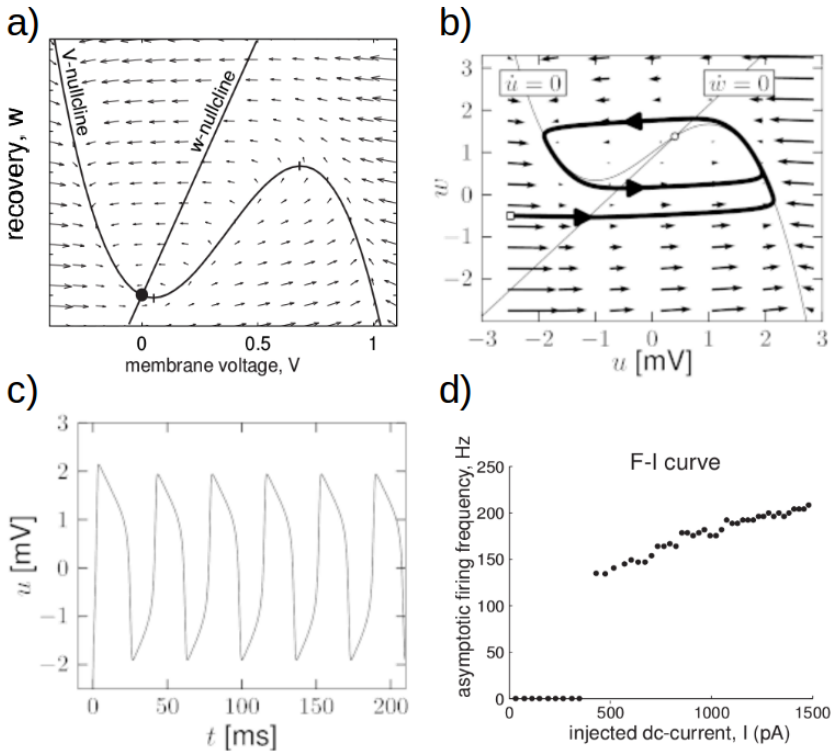

Figure 5.8: FitzHugh-Nagumo model and Type II neurons. a) Nullclines of the FH model (extracted from Ref.[49]. b) Relaxation oscillation in the FNM: trajectories in the w-u plane are shown. c) Spikes in the FNM (corresponding the trajectories of panel (b)) (extracted from Ref.[81]). d) Frequency response of a Type II neuron: recordings of a mesV (mesencephalic trigeminal) neuron from rat brainstem (extracted from Ref.[49]).

the stability of the fixed point: a negative real part indicates a stable point, while a positive indicates an unstable point. If the eigenvalues are complex then the solution is oscillatory (and both eigenvalues are complex conjugate). In Fig.5.9 we show the evolution of the real and imaginary part of the eigenvalues for our linearized system as we increase the stimulus around the left knee. The location of stationary points and the necessary derivatives are calculated numerically. We can see that as the voltage is increased then a oscillatory solution emerges and the fixed point goes from stable to unstable as the real part becomes positive. In Fig.5.10 we show this subthreshold oscillatory regime obtained from the integration of the model equations. The amplitude of these oscillations depends strongly on the particular selection of parameters. For the selected parameters the oscillations are extremely small (barely neglectable). By changing, for example, the values of $R_{MI,CM}$ an increase in its amplitude can be observed. An interesting aspect is that this regime can lead to stable periodic oscillations. In Fig.5.10 (left column) we show these oscillatory trajectories in the phase plane. We notice that these oscillations correspond to a complete different regime from

the large oscillations described before which might have a different frequency. We remark at this point that the same effect occurs when the system goes through the right knee region. In Fig.5.10 (right column) we show the small oscillatory regime around this second region.

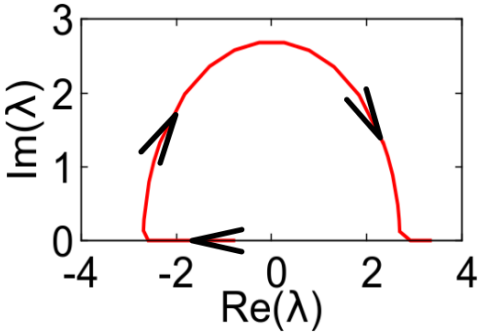

Figure 5.9: Real and imaginary parts of the eigenvalues of the linearized system around the stationary points. The plot shows the evolution as the voltage is increased around the critical region (left knee).

Finally we also notice that in the stochastic simulations of the resistor-network we observe large damped oscillations for voltages close to the threshold. These oscillations involve the transition of just a part of the device and cannot be reproduced with the integration of the model equations proposed in this section. The relevance and feasibility of these "subthreshold" oscillations (large or small) should be determined via experimental analysis.

5.5 A LIF (Leaky-Integrate-and-Fire) implementation

In this section we will consider a second type of neuronal implementation for VO_2 devices, i.e. the "Leaky-Integrate-and-Fire" neuron. The LIF model is one of the simplest and most widely used neuron models in computational neuroscience [49], and we will show briefly that it can also be realized with the VO_2 system. General circuital neuron models (such as the famous Hodgkin-Huxley model) describe the cell-membrane as made of a capacitive term in parallel with voltage activated channels (represented by non-linear conductances) and leak channels which account for the permeability of the membrane and are usually represented by Ohmic conductances (see *Bio-inspired Computing* in the Introduction). The LIF model is an idealization of a neuron having only a capacitive term with an Ohmic leakage current and a number of voltage-gated currents that are completely de-activated below threshold. Thus, the subthreshold behaviour of such a neuron can be written as:

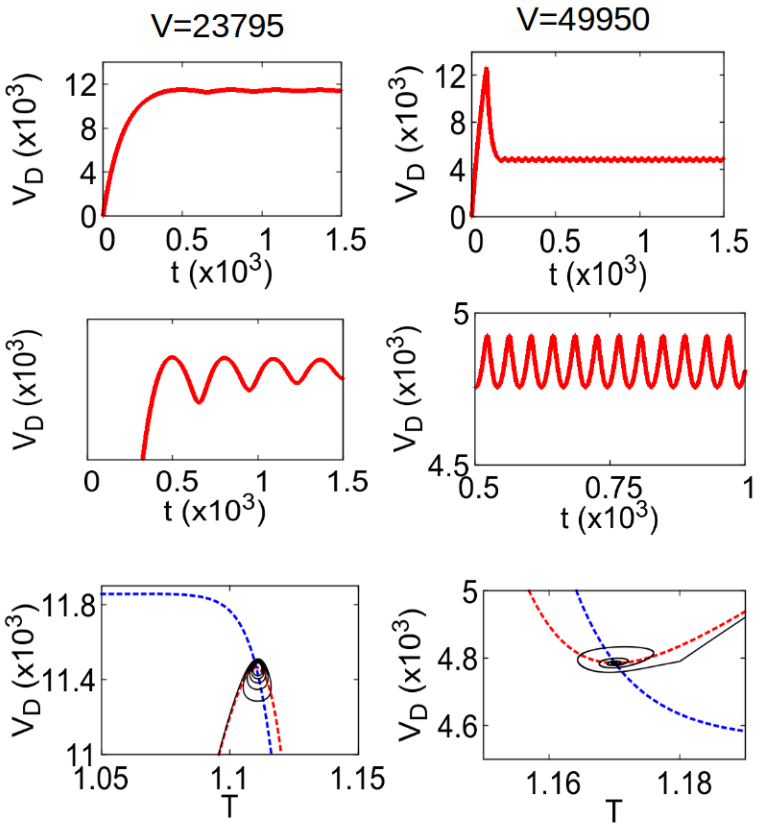

Figure 5.10: Left column: Subthreshold oscillations. Top panel: evolution of V_D as a function of time for a voltage close the threshold. Middle panel: detail of the small oscillatory regime observed for this voltage. Bottom panel: phase plane with the nullclines and trajectory of the system. Right column: small oscillatory regime around the right knee of the fast nullcline (see Fig.5.7).

$$C\frac{\partial V}{\partial t} = a - g_{leak}(V - V_{leak}) \tag{5.7}$$

where g_{leak} is the conductance of the leak channel and V_{leak} is known as the leak reversal potential. In the original version of the LIF model the first term a correspond to $a = I$ (being I the applied external current) and the system is equivalent to a capacitor in parallel with a leak current. When the membrane voltage reaches a certain threshold (at a time $t = t_{FIRE}$) an abrupt spike is generated. The spike generation is not described by the model equation. In computational applications the spike is simulated as a delta function, after which the membrane voltage is set to zero and the process starts again. Recent improvements, such as the Exponential-Leaky-Intergrate-and-Fire, have incorporated voltage dependent terms for describing the spiking process. The equivalence with our VO_2 system is straightforward, as we will discuss in the following. In our system the IMT transition ("spike") is thermally induced. Thus, we will consider the temperature dynamics in equivalence to the voltage dynamics from the biological neuron.

From Eq.5.4:

$$\frac{\partial T}{\partial t} c_h = \frac{V_D^2}{R_D} - \kappa (T - T_B) N \cdot W \tag{5.8}$$

The second term in the right hand side represents the heat "leaked" towards the substrate. This is equivalent to the leakage current in the biological case. On the other hand, we show in Fig.5.11 the evolution of the temperature during the application of a constant voltage.

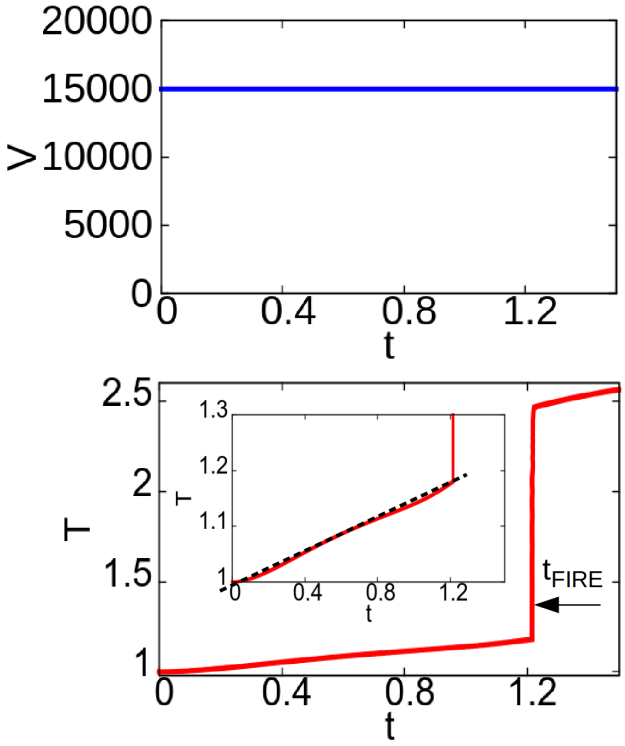

Figure 5.11: Evolution of the sample temperature (bottom) under the action of constant applied voltage (top). The region $t < t_{FIRE}$ follows approximately a linear evolution. Inset bottom panel: detail of the region $t < t_{FIRE}$.

We notice two important things from here: i) as seen in the previous section, the temperature suffers an abrupt increase when $T \approx T_{MT}$. This effect is generated by a positive feedback between the resistance and the temperature: the decrease in the resistance generates an increase in temperature (due to the higher current) which generates a further decrease in the resistance. We call t_{FIRE} to the time at which the abrupt change in T begins, in analogy to the neuronal case. ii) During the period $t < t_{FIRE}$, the temperature evolves approximately linearly with time. This is in agreement with the prediction of the LIF model (first term in the right hand side of Eq.5.7). For simplicity, in this simulations we set a small R_L ($R_L = 10$). This eliminates the effects due to long transient periods of the capacitor, treated in the previous section. To test the LIF implementation in our

model, we simulate a standard pulsed protocol on our device, which emulates the arrival of spikes from other neurons. In hardware implementations of artificial neural systems, instant spikes of biological neurons are often replaced by short squared voltage pulses, thus, this kind of protocol is relevant for technological applications. In Fig.5.12 we show the evolution of the temperature during a pulsed protocol. We can see that T increases linearly during the application of the pulse (of length t_{ON}) and it relaxes during interval between pulses (of length t_{OFF}). Finally, it reaches the threshold temperature ($T \approx T_{MT}$) and a spike is generated. The number of pulses necessary to trigger the spike (N_{FIRE}) can be easily measured experimentally. This makes it suitable for a future validation of our model and it has been used before for similar experiments [53] . From Eq.5.8 it is easy to see that:

$$N_{FIRE} = ceiling(1 - \frac{ln[e^{t_{OFF}/\tau} - \frac{t_{FIRE}}{t_{ON}}(e^{t_{OFF}/\tau} - 1)]}{t_{OFF}/\tau}) \tag{5.9}$$

where we assumed that $\frac{\partial T}{\partial t} \approx a$ while a pulse is on and $T(t) \approx T_i e^{-t/\tau}$ while the pulse is off. Since N_{FIRE} is an integer number of pulses, we use the ceiling function which maps a real number to the smallest following integer. In Fig.5.13 we show the evolution of N_{FIRE} as a function of $t_{ON/OFF}$ obtained from the simulations together with a fit according to Eq.5.9. We notice that for the case of null capacitive effects it would be $\tau = c_h/(\kappa N \cdot W)$. In our case, the capacitive effects are no null, and we used τ as the only free parameter for the fit.

This first analysis establishes the feasibility of a LIF implementation for the VO_2 system and it opens the possibility for further theoretical and experimental work in this direction.

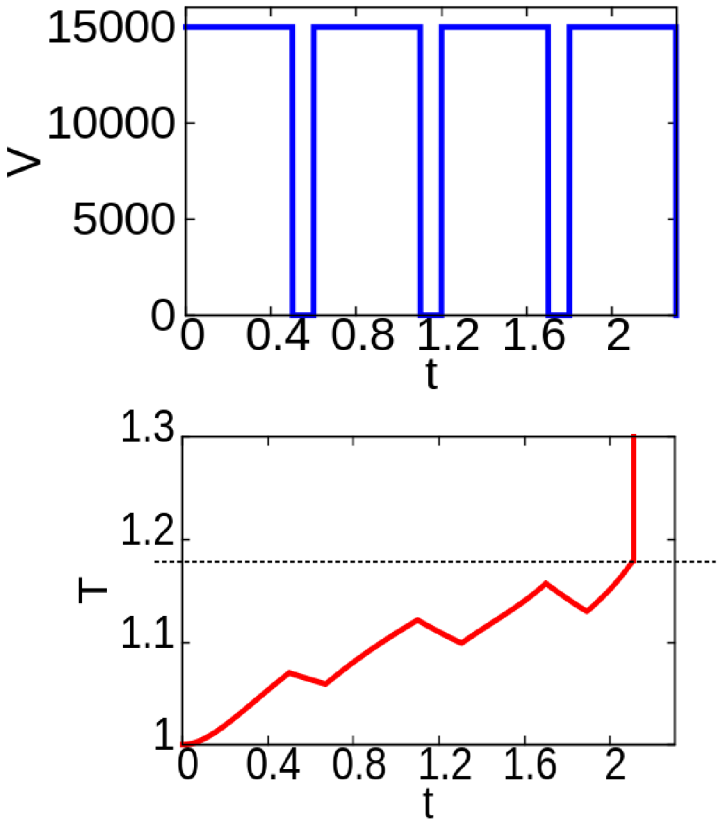

Figure 5.12: Simulations of a pulsed protocol. Top: applied voltage pulses. Bottom: evolution of the sample temperature (bottom) during a pulsed protocol. When the temperature reaches a threshold value ($T \approx T_{IMT}$), indicated with the horizontal dashed line, a spike is generated.

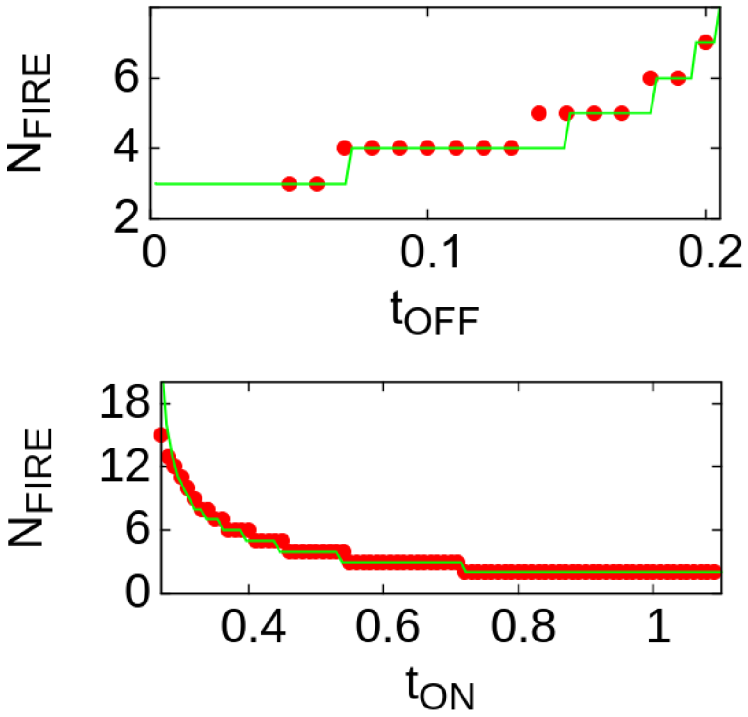

Figure 5.13: Evolution of N_{FIRE} as a function of the pulse length t_{ON}) (bottom) and pulse separation t_{OFF} (top). A fit according to Eq.5.9 is shown for each case. The fit corresponds to $t_{FIRE} = 1.28$, $\tau = 0.42$, $t_{ON} = 0.5$ (top) and $t_{OFF} = 0.1$ (bottom).

Una Neurona Artificial Basada en VO_2

En este capítulo se estudió el fenómeno de Conmutación Resistiva en el sistema VO_2. Se propuso un modelo fenomenológico que captura algunas de las características principales de este sistema, entre ellas las oscilaciones resistivas observadas en los experimentos. Luego se mostró que la dinámica del modelo es análoga a la del célebre modelo neuronal de FitzHugh-Nagumo para neuronas oscilatorias.

Chapter 6

Conclusions

In this thesis the phenomenon of Resistive Switching and its applications for Neuromorphic devices has been studied.

In Chapter 2, from quite general considerations of migration of ionic defects under strong electric fields in solids, we have argued that the dynamics of the spatial profile of defect concentration should be governed by a Burgers'-type nonlinear equation and develop shock waves. We demonstrated that this scenario is indeed realized within a concrete implementation, namely an ionic migration model that was previously applied to describe resistive switching phenomena in manganite based memristive devices. In those systems, a key role is played by the migration of oxygen vacancies, which are the ionic defects relevant to the electronic transport properties. We thus predicted a two-stage process for the resistive switch phenomenon. An initial one, where the oxygen-vacancy concentration profile develops a shock wave that propagates throughout a highly resistive (Schottky barrier) region near the electrode. During this phase the resistance essentially does not change. This is followed by a second phase, where the shock wave emerges from the high resistive region and the ionic defects leak into the conductive bulk. Our scenario was further validated by novel experimental data on a manganite based memristor device. A remarkable result of our study is that both, the numerical simulations and the experimental curves, obey a scaling behaviour, providing decisive support to our theory. The present work provides novel insights on the physical mechanism behind the commutation speed on novel non-volatile electronic memories, unveiling an unexpected connection between a phenomenon of technological relevance and a classic theme of nonlinear dynamical systems. Furthermore, and from a practical point of view, our study unveils some of the key physical parameters that control the resistive switching properties of devices. Of foremost importance are the characteristic time scales, τ_1 and τ_2. Interestingly, we find that both depend on on the same combination of parameters, namely $x_{int}^2/(DIR_{HI})$, and $x_{int}/(IR_{HI})$ that appears in the exponential factor (see Eq. 2.7 , Eq. 2.18 and 2.23 on section 2.9 and 2.11). While we may

intuitively understand that a shorter interface or a stronger current pulse would increase the commutation speed, this expression also provides concrete guidance for the engineering effort of devices, which is less evident. For instance, it shows that shortening the length of the interface by a factor of three should at least gain a full order magnitude in speed. It also points towards adopting materials where the diffusion constant of oxygen vacancies is large. While this is a priori fixed by the specific chemistry of the material, one may also envision that the diffusion might be boosted by preparing samples with smaller grain sizes and with extended columnar defects that could be induced by heavy ion irradiation.

In Chapter 3 we analyzed the general validity of the previous results for other type of very relevant resistive switching systems, such as binary oxides. In these systems, in contrast to the case of PCMO, the main effect of oxygen vacancies may be to dope electron carriers to an otherwise good insulator, decreasing the local resistance of the material. We have shown that it is also possible to describe the migration of oxygen ions in binary oxides memristors in terms of a Burgers' type nonlinear equation that leads to the formation of shock waves. This process is relevant for systems such as TiO_2 and HfO_2, which are of current technological importance. Our results show that the main contribution to the hi-lo commutation ratio occurs very fast, as it happens during the formation of the shock wave. Once the wave is well established and it evolves through the system there is just a small relative change of resistance. This feature may be tested experimentally and indicates that these binary memristors may switch in very short time scales without much degradation.

In Chapter 4 we have extended a model for the Electric Mott Transition (EMT) to incorporate electro-elastic effects. This feature leads to spatial correlations in the growth patterns of filamentary structures in the resistive transition. In particular, it leads to the thickening of the filaments during longer applied pulses or multiple pulses. The increased thickness of filaments was directly related to a dramatic increase in retention time of the low-resistance state.

We should mention that our model does not predict any sharp or discontinuous transition between the experimentally observed volatile regime (ii) and the non-volatile regime (iii) discussed in the introduction of Chapter 4. Nevertheless, it does indicate that the retention times may be exponentially increased by means of the applied pulsing protocol. Specifically the strength, duration and inter-pulse time, which may be tailored to optimize the growth and thickening of the filaments. The results of the previous section may be considered as an initial step in that direction. However, it should be realized that there are a large number of variables to take into account and the systematic investigation remains an important experimental challenge.

We also briefly refer to the qualitative similarities of our present model study

and the behavior of spiking leaky-integrate-and-fire neurons. We are aware of the relative simplicity of our system with respect to the biological ones but, nevertheless, this may be taken as a contribution towards future implementation of neuromorphic electronic systems. In this regard, it is very exciting to envision that strongly correlated Mott materials may realize unexpected bio-inspired functionality.

Finally, in Chapter 5 we have analyzed the RS phenomenon in VO_2 memristors. We have proposed a purely thermal phenomenological model that was able to capture some of the main features of RS in this systems, in particular the oscillations of the resistance observed in experiments. Then we were able to establish a connection between our system and the well known FitzHugh-Nagumo model for oscillatory neuron. We have shown that both systems obeys the same dynamics, which exhibits a discontinuity in the $f - V$ dependence. This last feature is believed to be fundamental for information processing in biological brains, and open the possibility of implementing this same mechanism at hardware level in Artificial Neural Networks. To conclude we have also shown that a Leaky-Integrate-and-Fire implementation is feasible in these systems. This implementation is widely used in theoretical neuroscience and is of current great importance for potential technological applications.

Appendices

Appendix A

Method of characteristics

In this section, we demonstrate that shock waves are typically formed in presence of sufficient nonlinearity, and analyze the problem via the *method of characteristics*. Considering the vacancy migration in highly resistive barriers, where we can neglect the normal diffusion term $D\partial_{xx}u$, we obtain a first order, partial differential equation of the general form

$$\partial_t u + c(u,t)\partial_x u = 0. \tag{A.1}$$

Here, the u dependence in $c(u,t)$ gives rise to the nonlinearity effect for the onset of shock wave formation. In order to determine the density profile evolution, we need to track the motion of points corresponding to specific values of u (see Fig.2.2, left panel). We can solve the trajectories (the so-called "characteristics") followed by such point in the $t-x$ plane by solving the following equation [54, 57] [1]:

$$\frac{dx}{dt} = c(u,t). \tag{A.2}$$

As different characteristics might intersect with each other in the $t-x$ plane (see the inset of Fig.2.2), the emergence of intersecting trajectories indicates that the solution $u(t,x)$ becomes multivalued, since the points can be traced back along each of the characteristics to different initial values of $u(t=0,x)$. The intersection which happens chronologically first determines the formation of the shock wave, as shown in Fig.2.2 . As an illustration, we provide an example with $c(u,t) = u^2$ and an initial Gaussian distribution $u(t=0,x) = 0.5\exp\left[-(x-5)^2/4\right]$. The time dependent wave profile is solved numerically with fixed boundary conditions, and characteristics are computed according to Eq.A.2.

We should stress, however, that this qualitative behavior is a robust feature of any such nonlinear diffusion equation, provided that the prefactor $c(u,t)$ is a monotonically *increasing* function of u (i.e. $\partial_u c(u,t) > 0$). To see this, note

[1] It's straightforward to see that u is constant along the characteristics, since $du/dt = dx/dt\partial_x u + \partial_t u = 0$.

that Eq. (A.1) takes the form of a simple wave equation, thus its solution is a traveling wave, with speed locally proportional to $c(u,t)$. Therefore, at any given time, each point on the wave front moves with a different speed proportional to $c(u,t)$ and the "crest" having the largest value of u moves *fastest*, which leads to a "kink" type shock. Alternatively, it is easy to check that if $\partial_u c(u,t) \leq 0$, the shock wave will not form. In the case where $c(u,t)$ is any function independent of u, the characteristics are curves of the same shape but parallel to each other, and hence they would not have any intersections; the shock wave would again not form. Finally, it can be shown that if the diffusion term $D\partial_{xx}u$, is non-zero but is parametrically small (as compared to the drift term), the diffusion will prevent the wave from topping over (to undergo "self-breaking"), and the shock wave front will remain sharp as it propagates [54, 57].

Appendix B

Filaments size distribution in Experiments

In Fig.B.1 we show the full distribution of metallic cross sections obtained from the scanning tunneling microscopy (STM) shown in Chapter 4. The image correspond to a cleaved surface of a $GaTa_4Se_8$ compound after the EMT. The total area of the sample is of about 500x500 nm^2.

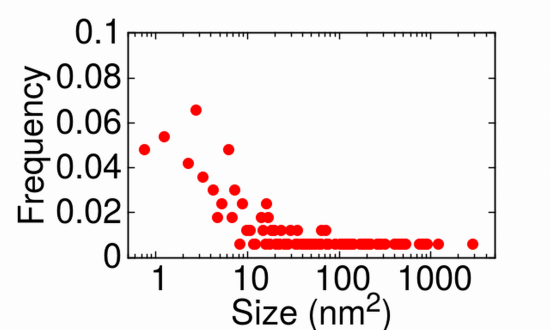

Figure B.1: Distribution of cross sectional areas of conductive structures obtained from the STM image of a cleaved $GaTa_4Se_8$ surface after the EMT.

Bibliography

[1] A. Sawa. "Resistive switching in transition metal oxides". In: *Materials Today* 11 (2008), pp. 28–36.

[2] J.J. Yang et al. "Memristive switching mechanism for metal/oxide/metal nanodevices". In: *Nature Nanotechnol.* 3 (2008), pp. 429–433.

[3] D Ielmini, F Nardi, and C Cagli. "Physical models of size-dependent nanofilament formation and rupture in NiO resistive switching memories". In: *Nanotechnology* 22.25 (2011), p. 254022. URL: http://stacks.iop.org/0957-4484/22/i=25/a=254022.

[4] Deok-Hwang Kwon et al. "Atomic structure of conducting nanofilaments in TiO 2 resistive switching memory". In: *Nature nanotechnology* 5.2 (2010), p. 148.

[5] Yong-Mu Kim and Jang-Sik Lee. "Reproducible resistance switching characteristics of hafnium oxide-based nonvolatile memory devices". In: *Journal of Applied Physics* 104.11 (2008), p. 114115.

[6] Daniele Ielmini et al. "Size-dependent retention time in NiO-based resistive-switching memories". In: *IEEE Electron Device Letters* 31.4 (2010), pp. 353–355.

[7] John Paul Strachan et al. "Direct identification of the conducting channels in a functioning memristive device". In: *Advanced materials* 22.32 (2010), pp. 3573–3577.

[8] YB Nian et al. "Evidence for an oxygen diffusion model for the electric pulse induced resistance change effect in transition-metal oxides". In: ().

[9] I.H. Inoue and A. Sawa. In: *Chap. 16 of Functional Metal Oxides, New Science and Novel Applications, Wiley-VCH, Germany (Eds. Ogale S, Venkatesan T, Blamire M)* (2013).

[10] X Chen et al. "Direct resistance profile for an electrical pulse induced resistance change device". In: *Appl. Phys. Lett.* 87 (2005), p. 233506.

[11] S.M. Sze and Kwok K. Ng. "Metal-Semiconductor Contacts". In: *Physics of Semiconductor Devices*. John Wiley and Sons, Inc., 2006, pp. 134–196. ISBN: 9780470068328. DOI: 10.1002/9780470068328.ch3. URL: http://dx.doi.org/10.1002/9780470068328.ch3.

[12] Antoine Georges et al. "Dynamical mean-field theory of strongly correlated fermion systems and the limit of infinite dimensions". In: *Rev. Mod. Phys.* 68 (1 1996), pp. 13–125.

[13] G. Kotliar et al. "Electronic structure calculations with dynamical mean-field theory". In: *Rev. Mod. Phys.* 78 (3 2006), pp. 865–951. DOI: 10.1103/RevModPhys.78.865.

[14] Etienne Janod et al. "Resistive Switching in Mott Insulators and Correlated Systems". In: *Advanced Functional Materials* 25.40 (2015), pp. 6287–6305.

[15] Gabriel Kotliar and Dieter Vollhardt. "Strongly correlated materials: Insights from dynamical mean-field theory". In: *Physics Today* 57.3 (2004), pp. 53–60.

[16] Masatoshi Imada, Atsushi Fujimori, and Yoshinori Tokura. "Metal-insulator transitions". In: *Rev. Mod. Phys.* 70 (4 1998), pp. 1039–1263.

[17] Hidehiko Kuwamoto, JM Honig, and J Appel. "Electrical properties of the (V 1- x Cr x) 2 O 3 system". In: *Physical Review B* 22.6 (1980), p. 2626.

[18] V Guiot et al. "Control of the Electronic Properties and Resistive Switching in the New Series of Mott Insulators GaTa4Se8–y Te y (0 y 6.5)". In: *Chemistry of Materials* 23.10 (2011), pp. 2611–2618.

[19] Regina Pocha, Dirk Johrendt, and Rainer Pöttgen. "Electronic and structural instabilities in GaV4S8 and GaMo4S8". In: *Chemistry of materials* 12.10 (2000), pp. 2882–2887.

[20] Regina Pocha et al. "Crystal structures, electronic properties, and pressure-induced superconductivity of the tetrahedral cluster compounds GaNb4S8, GaNb4Se8, and GaTa4Se8". In: *Journal of the American Chemical Society* 127.24 (2005), pp. 8732–8740.

[21] Helen Müller, Winfried Kockelmann, and Dirk Johrendt. "The magnetic structure and electronic ground states of Mott insulators GeV4S8 and GaV4S8". In: *Chemistry of materials* 18.8 (2006), pp. 2174–2180.

[22] MM Abd-Elmeguid et al. "Transition from Mott Insulator to Superconductor in G a N b 4 S e 8 and G a T a 4 S e 8 under High Pressure". In: *Phys. Rev. Lett.* 93.12 (2004), p. 126403.

[23] TF Qi et al. "Negative volume thermal expansion via orbital and magnetic orders in Ca 2 Ru 1- x Cr x O 4 (0¡ x¡ 0.13)". In: *Phys. Rev. Lett.* 105.17 (2010), p. 177203.

[24] V Eyert. "The metal-insulator transition of NbO2: An embedded Peierls instability". In: *EPL (Europhysics Letters)* 58.6 (2002), p. 851.

[25] Hyowon Park, Andrew J Millis, and Chris A Marianetti. "Site-selective Mott transition in rare-earth-element nickelates". In: *Phys. Rev. Lett.* 109.15 (2012), p. 156402.

[26] Cédric Weber et al. "Vanadium dioxide: A Peierls-Mott insulator stable against disorder". In: *Phys. Rev. Lett.* 108.25 (2012), p. 256402.

[27] Wen-Pin Hsieh et al. "Evidence for photo-induced monoclinic metallic VO2 under high pressure". In: *Applied Physics Letters* 104.2 (2014), p. 021917.

[28] Haidan Wen et al. "Structural and electronic recovery pathways of a photoexcited ultrathin VO 2 film". In: *Physical Review B* 88.16 (2013), p. 165424.

[29] Jiajun Li et al. "Electric-field-driven resistive switching in the dissipative Hubbard model". In: *Phys. Rev. Lett.* 114.22 (2015), p. 226403.

[30] FA Chudnovskii et al. "Switching phenomena in chromium-doped vanadium sesquioxide". In: *Journal of applied physics* 84.5 (1998), pp. 2643–2646.

[31] A. Camjayi et al. "First-Order Insulator-to-Metal Mott Transition in the Paramagnetic 3D System $GaTa_4Se_8$". In: *Phys. Rev. Lett.* 113 (8 2014), p. 086404.

[32] Jeehoon Kim et al. "Nanoscale imaging and control of resistance switching in VO 2 at room temperature". In: *Applied Physics Letters* 96.21 (2010), p. 213106.

[33] A Zimmers et al. "Role of thermal heating on the voltage induced insulator-metal transition in VO 2". In: *Phys. Rev. Lett* 110.5 (2013), p. 056601.

[34] Tom Driscoll et al. "Phase-transition driven memristive system". In: *Applied physics letters* 95.4 (2009), p. 043503.

[35] Y Taguchi, T Matsumoto, and Y Tokura. "Dielectric breakdown of one-dimensional Mott insulators Sr 2 CuO 3 and SrCuO 2". In: *Physical Review B* 62.11 (2000), p. 7015.

[36] S Yamanouchi, Y Taguchi, and Y Tokura. "Dielectric breakdown of the insulating charge-ordered state in La 2- x Sr x NiO 4". In: *Phys. Rev. Lett.* 83.26 (1999), p. 5555.

[37] Cristian Vaju et al. "Electric-Pulse-driven Electronic Phase Separation, Insulator–Metal Transition, and Possible Superconductivity in a Mott Insulator". In: *Advanced Materials* 20.14 (2008), pp. 2760–2765.

[38] Laurent Cario et al. "Electric-Field-Induced Resistive Switching in a Family of Mott Insulators: Towards a New Class of RRAM Memories". In: *Advanced Materials* 22.45 (2010), pp. 5193–5197.

[39] Takashi Oka, Ryotaro Arita, and Hideo Aoki. "Breakdown of a mott insulator: a nonadiabatic tunneling mechanism". In: *Phys. Rev. Lett.* 91.6 (2003), p. 066406.

[40] Hideo Aoki et al. "Nonequilibrium dynamical mean-field theory and its applications". In: *Rev. Mod. Phys.* 86 (2 2014), pp. 779–837.

[41] Vincent Guiot et al. "Avalanche breakdown in $GaTa_4Se_{8-x}Te_x$ narrow-gap Mott insulators". In: *Nature Communications* 4 (2013), p. 1722.

[42] Pablo Stoliar et al. "Universal Electric-Field-Driven Resistive Transition in Narrow-Gap Mott Insulators". In: *Advanced Materials* 25.23 (2013), pp. 3222–3226.

[43] John Backus. *Can programming be liberated from the von Neumann style?: a functional style and its algebra of programs*. ACM, 2007.

[44] Alan Gara et al. "Overview of the Blue Gene/L system architecture". In: *IBM Journal of research and development* 49.2.3 (2005), pp. 195–212.

[45] John Hertz, Anders Krogh, and Richard G Palmer. *Introduction to the theory of neural computation.* Addison-Wesley/Addison Wesley Longman, 1991.

[46] M Bishop Christopher. *PATTERN RECOGNITION AND MACHINE LEARNING.* Springer-Verlag New York, 2016.

[47] Stphane Mallat. "Group Invariant Scattering". In: *Communications on Pure and Applied Mathematics* 65.10 (2012), pp. 1331–1398.

[48] Jrgen Schmidhuber. "Deep learning in neural networks: An overview". In: *Neural Networks* 61 (2015), pp. 85 –117.

[49] Eugene M Izhikevich. *Dynamical systems in neuroscience*. MIT press, 2007.

[50] Sung Hyun Jo et al. "Nanoscale Memristor Device as Synapse in Neuromorphic Systems". In: *Nano Letters* 10.4 (2010), pp. 1297–1301.

[51] Yuriy V. Pershin and Massimiliano Di Ventra. "Experimental demonstration of associative memory with memristive neural networks". In: *Neural Networks* 23.7 (2010), pp. 881 –886.

[52] Matthew D Pickett, Gilberto Medeiros-Ribeiro, and R Stanley Williams. "A scalable neuristor built with Mott memristors". In: *Nature Mat* 12.2 (2013), pp. 114–117.

[53] Pablo Stoliar et al. "A Leaky-Integrate-and-Fire Neuron Analog Realized with a Mott Insulator". In: *Advanced Functional Materials* 27.11 (2017), p. 1604740.

[54] Lokenath Debnath. *Nonlinear partial differential equations for scientists and engineers*. Springer Science & Business Media, 2011.

[55] J.J. Yang et al. "Metal oxide memories based on thermochemical and valence change mechanisms". In: *MRS Bulletin* 37.02 (2012), pp. 131–137.

[56] M Taylor. "Partial Differential Equations I,II,III". In: *Applied Mathematical Sciences* (2011).

[57] R Courant and D Hilbert. "Methods of mathematical physics. Vol. II: Partial differential equations". In: *Interscience, New York* (1962).

[58] MJ Rozenberg et al. "Mechanism for bipolar resistive switching in transition-metal oxides". In: *Phys. Rev. B* 81 (2010), p. 115101.

[59] HS Lee et al. "A new route to the Mott-Hubbard metal-insulator transition: Strong correlations effects in $Pr_{0.7}Ca_{0.3}MnO_3$". In: *Scientific Reports* 3.17 (2013).

[60] L Landau. "Fluid Mechanics (Course Of Theoretical Physics)". In: *Butterworth-Heinemann* 6 (1987).

[61] M Quintero et al. "Mechanism of Electric-Pulse-Induced Resistance Switching in Manganites". In: *Phys. Rev. Lett.* 98 (2007), p. 116601.

[62] YL Jin et al. "Enhancement of resistive switching effect in double-layered Pt/Pr0.7Ca0.3MnO3/La0.6Pr0.4MnO3/SrNb0.01Ti0.99O3 heterostructure". In: *Physica B-Condensed Matter* 449 (2014), pp. 52–56.

[63] M Scherff et al. "Interplay of cross-plane polaronic transport and resistive switching in Pt-Pr0.67Ca0.33MnO3-Pt heterostructures". In: *New Journal of Physics* 15 (2013), pp. 103008/1.

[64] S Park et al. "Self-formed Schottky barrier induced selector-less RRAM for cross-point memory applications". In: *Physica Status Solidi-Rapid Research Letters* 6 (2012), pp. 454–456.

[65] A Herpers et al. "Spectroscopic Proof of the Correlation between Redox-State and Charge-Carrier Transport at the Interface of Resistively Switching Ti/PCMO Devices," in: *Advanced Materials* 26 (2014), pp. 2730–2735.

[66] F. Gomez-Marlasca et al. "Modeling electronic transport mechanisms in metal-manganite memristive interfaces". In: *J. Appl. Phys.* 113 (2013), p. 144510.

[67] N. Ghenzi et al. "Hysteresis switching loops in ag-manganite memristive interfaces". In: *Journal of Applied Physics* 107 (2010), p. 093719.

[68] N Ghenzi et al. "Tuning the resistive switching properties of TiO2-x films". In: *Appl. Phys. Lett.* 106 (2015), p. 123509.

[69] S. Tang et al. "Shock Waves and Commutation Speed of Memristors". In: *Phys. Rev. X* 6 (2016), p. 011028.

[70] P Stoliar et al. "Nonthermal and purely electronic resistive switching in a Mott memory". In: *Physical Review B* 90.4 (2014), p. 045146.

[71] M. M. Qazilbash et al. "Mott Transition in VO_2 Revealed by Infrared Spectroscopy and Nano-Imaging". In: *Science* 318.5857 (2007), pp. 1750–1753.

[72] Vincent Dubost et al. "Resistive Switching at the Nanoscale in the Mott Insulator Compound GaTa4Se8". In: *Nano Letters* 13.8 (2013), pp. 3648–3653.

[73] Steven H Strogatz. *Nonlinear Dynamics and Chaos*. Westview Press, 2000.

[74] Angus J. Wilkinson, Graham Meaden, and David J. Dingley. "High-resolution elastic strain measurement from electron backscatter diffraction patterns: New levels of sensitivity". In: *Ultramicroscopy* 106.45 (2006), pp. 307 –313.

[75] Fred Rieke et al. *Spikes : exploring the neural code*. Cambridge, MA, USA: MIT Press, 1999. ISBN: 0-262-18174-6.

[76] Wulfram Gerstner et al. "Neural codes: Firing rates andbeyond". In: *Proceedings of the National Academy of Sciences* 94.24 (1997), pp. 12740–12741.

[77] Peter Dayan and Laurence F Abbott. *Theoretical neuroscience*. Vol. 806. Cambridge, MA: MIT Press, 2001.

[78] G Kotliar, E Lange, and MJ Rozenberg. "Landau theory of the finite temperature Mott transition". In: *Phys. Rev. Lett.* 84.22 (2000), p. 5180.

[79] A. Pergament, G. Stefanovich, and A. Velichko. "Relaxation oscillations in circuits containing sandwich switches based on vanadium dioxide". In: *Phase Transitions* 90.4 (2017), pp. 351–361.

[80] Alexander Pergament et al. "Electrical switching and oscillations in vanadium dioxide". In: *Physica B: Condensed Matter* (2017).

[81] Wulfram Gerstner et al. *Neuronal dynamics: From single neurons to networks and models of cognition*. Cambridge University Press, 2014.